Static and fatigue assessment of the mixed-mode behaviour of adhesively bonded joints

Maria Benedita Pereira da Silva e Vasconcellos Ferreira

A dissertation submitted for Master's Degree in Mechanical Engineering

Supervisor: Prof. Lucas F. M. da Silva

Co-Supervisor: Mr. Marcelo B. S. F. P. da Costa

July 2016

To my sister

Abstract

The use of adhesives as a structural bonding component has been increasing in a wide range of industries, mostly because of advantages related to performance and cost.

Fracture mechanics tests provide important tools to evaluate adhesive joints strength. The determination of the toughness gives a huge contribute guiding the design process. Also, as many failures occur due to an extensive exposure to cyclic conditions, the study of the fatigue behavior in adhesive joints is of extreme importance. In fact, those cyclic loadings can cause failure for lower load values than those required to cause quasi-static failure.

The present work aims to obtain the full fracture envelopes of three different adhesives by determining the fracture energy in in mode I, mode II and some mixed-mode I+II combinations. Double Cantilever Beam (DCB) and End-Notched Flexure (ENF) tests were performed to assess mode I and mode II fracture behaviour. Regarding mixed-mode analysis, a versatile apparatus was used to perform a wide range of mixed-mode combinations from mode I to mode II. The energy release rate was estimated considering an equivalent crack length method, the Compliance Based Beam Method (CBBM). DCB and mixed-mode numerical models, implemented in ABAQUS®, were used to model the experimental data.

Moreover, the study includes the assessment of adhesively bonded joints under cyclic-fatigue loading using a fracture mechanics approach. The fatigue behaviour was evaluated through the measurement of the fatigue crack growth (FCG) and Paris-law parameters in joints subjected to the same types of loading studied in quasi-static conditions.

The results reveal the adequacy of the mixed-mode apparatus, presenting consistent values for the fracture energies in every mixed-mode combination studied. The fracture envelopes point to a linear criterion for the most ductile adhesive and quadratic criterion for other two adhesives studied. From the fatigue tests, it was concluded that the presence of mode II loadings affects the crack propagation leading to slower growth. The closer to mode I, the more abrupt is the slope of the FCG curves.

Resumo

As juntas adesivas estruturais são cada vez mais utlizadas em diversas industrias como substituto dos métodos convencionais de ligação. Esta tendência deve-se essencialmente às vantagens dos adesivos em termos de desempenho e custos.

Os ensaios de mecânica da fratura permitem avaliar a resistência das juntas, conduzindo à determinação da sua tenacidade o que proporciona um contributo importante no projeto de juntas. Por outro lado, uma vez que muitas falhas ocorrem devido à exposição prolongada a cargas cíclicas é extremamente importante o estudo do comportamento à fadiga de juntas adesivas. Verifica-se que a rutura em fadiga ocorre para cargas significativamente mais baixas do que as cargas necessárias para causar rotura em condições estáticas.

A presente dissertação tem como objetivo obter envelopes de fratura através do estudo da tenacidade de três adesivos em modo I, modo II e algumas combinações em modo-misto I+II. Para analisar o comportamento à fratura em modo I e II, efetuaram-se os ensaios *Double Cantilever Beam* (DCB) e *End Notched Flexure* (ENF), respetivamente. Relativamente ao estudo em modo misto, foi utilizado um dispositivo que permite o estudo de várias combinações de carga entre modo I e modo II. As taxas de libertação de energia foram determinadas recorrendo a um método baseado no conceito de fenda equivalente*, Compliance Based Beam Method* (CBBM). Foi ainda levada a cabo uma análise numérica utilizando modelos de DCB de modo misto, implementados em ABAQUS®, para modelação dos resultados experimentais.

Adicionalmente, foi efetuado também um estudo de fadiga em juntas adesivas usando os conhecimentos da Mecânica da Fratura. O comportamento à fadiga de juntas foi avaliado através da medição das curvas de crescimento da fenda para os mesmos tipos de carga estudados em condições quase-estáticas.

Os resultados revelam a adequabilidade do dispositivo utilizado para a avaliação da tenacidade em modo-misto. O envelope de fratura do adesivo mais dúctil segue um critério linear enquanto que os envelopes determinados para os outros dois adesivos estudados se adequam melhor ao critério quadrático. A partir dos ensaios de fadiga foi possível concluir que a presença de esforços de corte contribui para uma propagação mais lenta de fendas.

Acknowledgments

I would like to express my gratitude to Prof. Lucas da Silva for the opportunity to work as "part of this team", for the advices and for sharing his vast knowledge.

I would like to thank Mr. Marcelo Costa for his continuous guidance, and for his promptitude and availability when clarifying my doubts.

I also would like to thank every member on the FEUP Adhesives Group, particularly Dr. Ricardo Carbas for his supporting during the lab days.

I must also acknowledge the *Laboratório de Ensaios Tecnológicos (LET)* for giving me the opportunity to perform the experimental tests.

I would like to thank Fundamental Technology Research Center Honda R&D Co. Ltd for supporting this work.

And finally, I would like to thank my family and friends for being always by my side during the long hours of this project.

Contents

List of Figures

List of Tables

List of acronyms and symbols

Acronyms

ADCB	Asymmetric Double Cantilever Beam
ATCB	Asymmetric Tapered Double Cantilever Beam
CBBM	Compliance Based Beam Method
CBT	Corrected Beam Theory
CCM	Compliance Calibration Method
CLS	Crack Lap Shear
CZM	Cohesive Zone Model
DBT	Direct Beam Theory
DCB	Double Cantilever Beam
ENF	End Notched Flexure
FCG	Fatigue Crack Growth
FPZ	Fracture Process Zone
LEFM	Linear Elastic Fracture Mechanics
LVDT	Linear Variable Differential Transformer
MMB	Mixed-mode Bending
R-curve	Resistance Curve
SLB	Single Leg Bending

Symbols

K	Stress intensity factor
K_c	Critical stress intensity factor
G	Strain energy release rate
G_c	Critical strain energy release rate
G_I	Strain energy release rate in mode I
G_{II}	Strain energy release rate in mode II
E	Young's modulus
E_f	Flexural modulus
υ	Poisson's ratio
a_e	Equivalent crack length
P_{max}	Maximum load
P_{min}	Minimum load
σ_e	Tensile strength
ε_r	Failure strain
φ	Mixed-mode angle

1 Introduction

1.1 Background and motivation

The use of adhesives as a structural bonding component has been increasing in a wide range of industries, mostly because of all the advantages that this technology offers, in terms of performance and costs. Thereby, the necessity of optimizing the joint design has promoted efforts in the research and knowledge of adhesion science. Within this context, it is crucial to study the behaviour of adhesive joints exposed to conditions similar to those experimented during service.

Fracture mechanics tests provide important tools to evaluate adhesive joints strength. The determination of the toughness gives a huge contribute guiding the design process.

Adhesive joints are subjected to opening loads (mode I), shear loads (mode II and III) and various combinations of these two types. Therefore, the characterization of the fracture behaviour over a wide range of combinations between pure modes is necessary to predict failure in real joints.

Considering the importance of studying fatigue, there is still a lack of information regarding to the characterization of adhesive joints behaviour under mixed-mode cyclic conditions.

1.2 Objectives

The objective of the present work is the assessment of the fracture and fatigue behaviour of adhesive joints over a wide range of mixed-mode combinations from pure mode I to pure mode II. More specifically:

1. Determination of the fracture envelopes of three adhesives to achieve mixed-mode energetic failure criteria.
2. Development of a test method for the assessment of fatigue in the mixed-mode testing of adhesively bonded joints;
3. Determination of Paris law parameters as a function of the mixed-mode angle.

1.3 Research methodology

1. Overview of the basic concepts of adhesives, fracture and fatigue test methods;
2. Double Cantilever Beam (DCB) and End Notched Flexure (ENF) tests to characterize the fracture toughness in pure modes;
3. Mixed-mode tests using a mixed-mode apparatus to predict the fracture toughness over wide a range of phase angles, from pure mode I to pure mode II;
4. Finite element analysis using ABAQUS® to model experimental fracture results;

5. Fatigue tests in mode I, mode II and some mixed-mode combinations to determine the corresponding fatigue crack growth (FCG) curves and to evaluate the Paris law slope as a function of the phase angle.

1.4 Thesis outline

This thesis is structured in the following sections:

Chapter 2: An overview of adhesive joints technology, starting by the general characteristics of adhesives and the most used approaches to predict the strength of adhesives. The classical fracture mechanics tests are then described as well as the methodology applied to achieve the toughness of adhesives, Compliance Based Beam Method. This chapter also includes the description of mixed-mode apparatus used to performe the mixed-mode analysis. General considerations about fatigue are presented, focusing on the fracture mechanics approach.

Chapter 3: This chapter comprehends a detailed explanation of the experimental work done. The materials used and the specimen manufacture are here described as well as the fracture and fatigue test specifications followed in this thesis.

Chapter 4: The results obtained for both fracture and fatigue experiments are presented in this chapter followed by the respective discussion. The fracture energies of each test are summarized in fracture envelopes. The fatigue results are shown in terms Paris law slope, leading to Paris law slope envelopes. A criterion is also proposed to relate the FCG curves obtained with the literature.

Chapter 5: Finite element analysis (using ABAQUS®) is described for mode I and mixed mode I+II to validate the experimental fracture results.

Chapter 6: Final conclusions and future works.

2 Literature review

Adhesives are polymeric materials that when applied to surfaces can bond them and resist to their separation. The set composed by the materials joined (adherends) and the adhesive between them is defined as an adhesive joint (Figure 2.1) (da Silva et al. 2007).

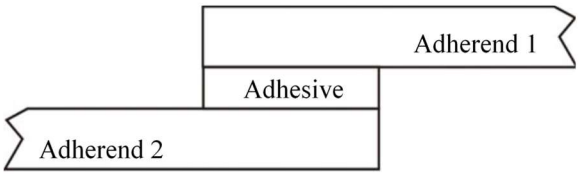

Figure 2.1 – Adhesive joint (adapted from da Silva et al. 2011).

The increasing application of the adhesive joints as an alternative to mechanical joints is related to the numerous advantages presented over conventional mechanical fastened methods. Adhesives provide a more uniform stress distribution over the bonded area allowing higher stiffness and load transmission. Also, by avoiding stress concentrations promoted by bonding elements such as rivets, the fatigue behaviour is improved. Other advantages related to reduced weight and cost come from using the adhesive bonding technology (da Silva et al. 2011).

2.1 Structural adhesives

An adhesive is considered to be a structural adhesive when it can resist to substantial loads, being responsible for the strength and stiffness of the structure (Adams et al. 1997). Generally, the shear strength of these adhesives goes from 5 MPa (for polyurethanes) to 50MPa (for epoxies) (da Silva et al. 2011).

The selection of the appropriate adhesive for a certain application requires the consideration of some factors such as the join design, the type of substrates or the intended joint performance (da Silva et al. 2011). The most commonly used adhesives for structural applications and their corresponding characteristics are presented in Table 2.1.

Table 2.1 - Characteristics of different structural adhesives (da Silva et al. 2011).

Adhesive	Characteristics
Epoxy	High strength Good toughness Temperature resistance
Polyurethanes	Good strength and toughness at low temperatures Resistant to fatigue Impact resistance Good durability
Phenolic	High hardness Excellent thermal stability Limited resistance to thermal shocks Difficult to process
Silicone	Environmental stability High degree of flexibility Capability to bond materials of various natures High cost

2.2 Failure modes

Bonded joints break by adhesion, cohesion or a combination of the two (Figure 2.2). Cohesion failure happens when the crack propagates in the adhesive and its occurrence indicates that the adhesive strength is weaker than the strength of the substrate of the interface. On the other hand, the adhesion failure means failure at the interface, and it is typical of inadequate surface preparation or ineffective surface preparation process (da Silva et al. 2011; Katsiropoulos et al. 2012).

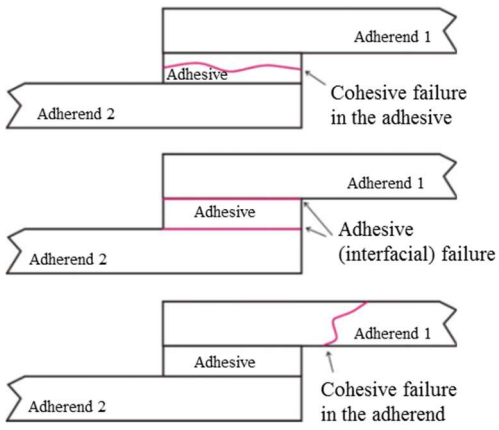

Figure 2.2 – Examples of cohesive and adhesive failure (da Silva et al. 2011).

The interphase is the region between the adhesive and adherend. It consists in a thin layer presenting different physical and chemical characteristics from the adherend and adhesive. Inside the interphase there is the interface, which is the contact plane between the surface and the two materials. The nature of the interface determines the mechanical properties of the adhesive bonding (da Silva et al. 2011).

Different adhesives exhibit different failure modes despite having the same adherend. Temperature and moisture strongly influence the locus of failure. Therefore, bonded joint failure is not easy to predict because many parameters can influence it (Renart et al. 2014).

2.3 Failure criteria

The increase of structural applications for adhesives requires the development of theories and models. There are two basic approaches to predict the failure of adhesive joints: continuum and fracture mechanics (de Moura et al. 2008).

2.3.1 Continuum mechanics

According to this theory there is a perfect joining between adhesive and adherend, meaning that the presence of defects or materials with protuberances infringes the basic principle. This theory aims to characterize the stresses and deformations in the bonded parts and to define the maximal force applied (Rodrigues 2015; Chaves et al. 2014).

However, it has the restriction of not providing a rigorous description of the structures' behavior when stress singularities are present (de Moura et al. 2008).

2.3.2 Fracture mechanics

Fracture mechanics approaches have some advantages over strength-based methods. Assuming the possibility of the structure having defects such as cracks, voids, delamination, *etc.*, this theory evaluates if the defect will cause failure or if during the structure's lifetime the defect will remain under the critical size. (da Silva et al. 2007; Chaves et al. 2014).

Regarding the Linear Elastic Fracture Mechanics (LEFM), there are two different concepts to evaluate the crack propagation: a stress intensity factor criterion and an energetic criterion.

The stress intensity factor (Irwin et al. 1958) is a geometric parameter that characterizes the stress field in the neighborhood of the crack tip

$$K = Y\sigma_R\sqrt{\pi a} \tag{2.1}$$

where Y is a non-dimensional factor depending on the geometry and load distribution. σ_R is the remote tension applied and a is the crack size.

According to this theory, the crack propagation will occur when the stress intensity factor equals the critical value, K_c, named fracture toughness and established for the material

$$K = K_c \tag{2.2}$$

Fracture mechanics usually applies the energetic analysis due to the physical importance related to the strain energy release rate and also because of the difficulty on the determination of the stress intensity factor (de Moura et al. 2008).

The energetic criterion relies on the concept established by Griffith (1921). According to this criterion, an intern defect propagates when the energy available at the tip, G, known as energy release rate, equals the energy needed for the crack to propagate, G_c, the critical energy release rate (da Silva et al. 2007).

Thus, to avoid crack propagation:

$$G \leq G_c \tag{2.3}$$

These presented concepts were found to be related by Irwin's studies. For the plane stress state, the stress intensity factor, K, and the Energy release rate, G, are related by:

$$G = \frac{K^2}{E} \tag{2.4}$$

And for the plane strain state

$$G = \frac{K^2(1-\nu^2)}{E} \tag{2.5}$$

where E is the Young's modulus and ν is the material Poisson's ratio.

As shown in Figure 2.3, three modes of crack propagation can be distinguished for different loading application. Mode I is the opening mode and mode II and III are the shear modes.

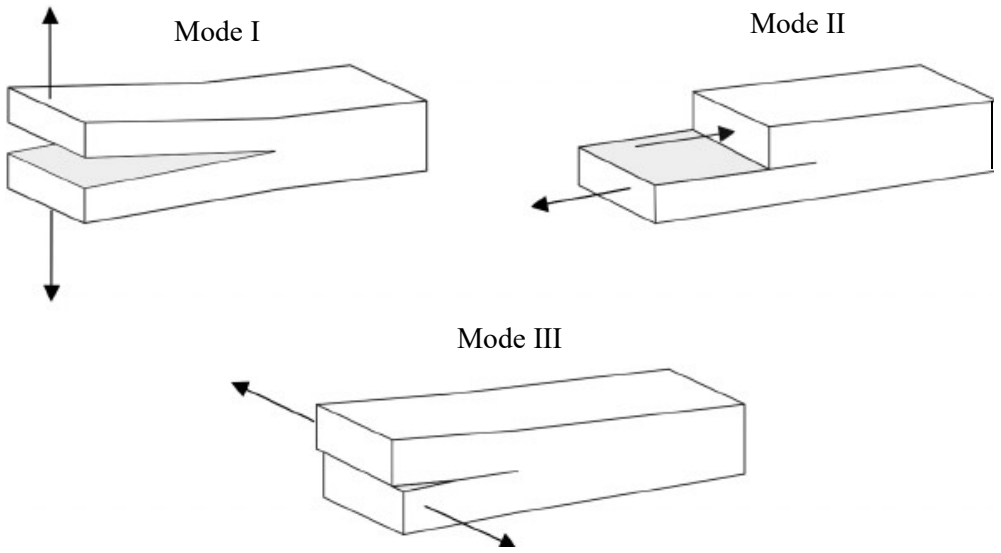

Figure 2.3 – Fracture modes (Chaves et al. 2014).

In most of the real situations crack propagation occurs as a combination of the mentioned modes, requiring a mixed mode analysis. (Chaves et al. 2014)

Particularly, in adhesive joints, the crack propagation that normally is perpendicular to the maximum stress applied, is restricted by the subtracts leading to a mixed-mode I+II propagation. In these circumstances the use of a suitable energetic criterion is needed, *e.g.*:

$$\left(\frac{G_I}{G_{Ic}}\right)^{\alpha} + \left(\frac{G_{II}}{G_{IIc}}\right)^{\beta} = 1 \tag{2.6}$$

where the index I and II indicate the pure mode to which the energy release rate refers. α and β are constants that usually take the value $\alpha = \beta = 1$ or $\alpha = \beta = 2$, referring to linear and quadratic criterion, respectively (da Silva et al. 2007; Chaves et al. 2014).

Fracture Mechanics relies on the presence of defects that are usually artificially modeled as pre-cracks to simulate the damage caused by the production process or induced during the service. Though, criteria based on Fracture Mechanics are better suited for crack propagation than for initiation (da Silva et al. 2007).

2.4 Numerical approach

In order to overcome the drawbacks of the analytical approaches mentioned above and exploit the usefulness of their advantages, damage models emerge as a suitable choice (de Moura et al. 2008).

Cohesive and continuum damage models allow the simulation of damage initiation and crack propagation. Both of these methodologies are suited for fracture analysis, combining aspects of stress based analysis and fracture mechanics to deal with the different stages of damage (de Moura, Gonçalves, et al. 2008).

Continuum damage models are better suited for cases when the thickness has to be considered. There is a region near the crack tip, named Fracture Process Zone (FPZ) where inelastic processes happen. As can be seen in Figure 2.4, FPZ varies as a function of the thickness, therefore, affecting the fracture behaviour of adhesive joints. These models are excellent tools to evaluate this influence on the fracture behaviour. Continuum damage models also provide a good simulation of the crack patch propagation in bonded joints (de Moura et al. 2008; Chaves et al. 2014).

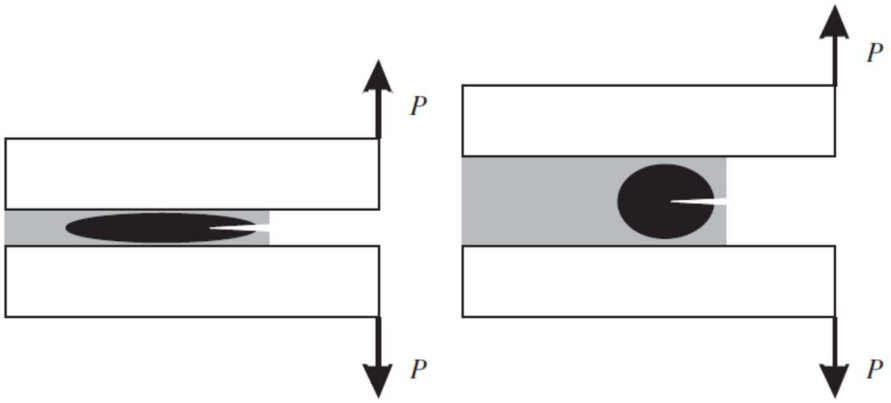

Figure 2.4 – Influence of adhesive thickness on the FPZ (de Moura et al. 2008).

Cohesive zone models (CZM) are usually applied to interface finite elements. Those finite elements are characterized by the absence of thickness promoting the connection of different material susceptible of being separated. This artifice allows two points originally connected to open as a rupture criterion is satisfied, promoting damage propagation (da Silva et al. 2007). The main advantage of CZM is the fact of not needing to assume a pre-crack or to know the direction of propagation.

The rupture process should be gradual. As the crack grows, the energy associated dissipates. This phenomenon is simulated considering a softening law, represented in Figure 2.5, relating stresses and relative displacements between homologous points of the elements. To simulate the behavior of ductile adhesives, a trapezoidal softening law should be used. The plateau region of the trapezoidal law corresponds to the progressive softening of the material. For more brittle adhesives, the trapezoidal law converts into a triangular one, without the plateau.

Since generally bonded joints are under mixed-mode loading, a formulation for the interface finite elements should include a mixed-mode damage model, which is an extension of the pure-mode model (de Moura et al. 2008).

Cohesive damage models use a stress criterion to predict damage onset. The crack growth is simulated using an energetic criterion.

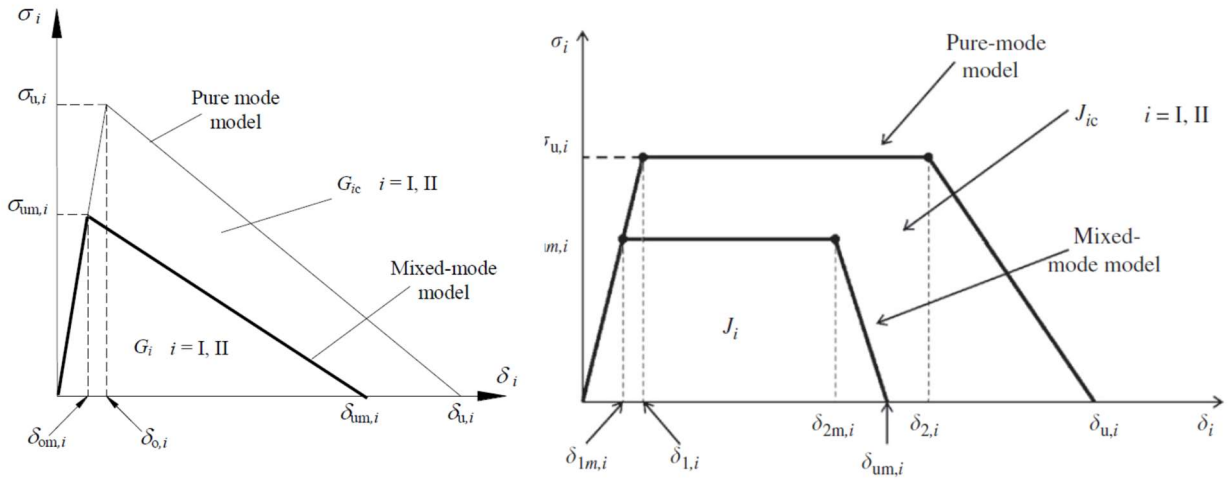

Figure 2.5 – Triangular and trapezoidal softening laws for pure and mixed-mode (Chaves et al. 2014; Chaves et al. 2011)

2.5 Fracture mechanics tests

Fracture mechanics tests provide powerful tools to evaluate adhesive joints strength. These tests allow to reach the value for the critical energy release rate, G_c, representative of the fracture toughness. According to the mode of loading, several tests have been developed to characterize the failure of adhesive joints (da Silva et al. 2007; Chaves et al. 2014).

The fracture resistance in any mode may be determined using the Irwin-Kies equation (da Silva et al. 2011):

$$G_c = \frac{P^2}{2B}\frac{dC}{da} \tag{2.7}$$

Where B is the specimen width, P is the load and C is the compliance, given by:

$$C = \frac{\delta}{P} \tag{2.8}$$

Applying the classical reduction schemes to determine the G_c, such as the compliance calibration method (CCM), corrected beam theory (CBT) or direct beam theory (DBT), can induce non-negligible errors to the value estimated, since these approaches depend on accurate crack length measurement during the propagation. That accuracy is difficult to reach due to unstable crack propagation or difficulties in clearly visualizing the crack tip. FPZ develops ahead of the crack tip in consequence of multiple micro-cracks nucleation through the adhesive thickness and plastification, making the identification of the crack tip locus even more difficult (de Moura et al. 2008). Also, the energy released at the FPZ can be large, particularly when ductile adhesives are used and should be taken into account in the selected data reduction scheme (de Moura et al. 2008).

The compliance based beam method (CBBM) overcomes these limitations. This approach is based on the crack equivalent concept avoiding crack monitoring during the test (Figure 2.6). Furthermore, the CBBM incudes the FPZ effects and takes into account the Young's modulus scattering between different specimens considering an equivalent elastic modulus (de Moura et al. 2008). Using this data reduction scheme the fracture toughness can be obtained by experimental determination of the load and displacement.

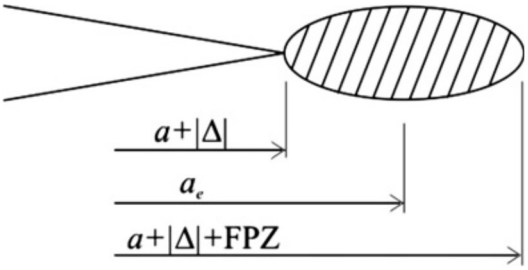

Figure 2.6 – Schematic representation of the FPZ and crack equivalent concept (de Moura et al. 2008).

The value of G_c is deducted from a resistance curve (R-curve). This curve represents the energy release rate as a function of the crack length. The mean value of G_c will be considered when the value of G do not tend to change significantly, leading to a stabilization plateau of the curve (da Silva et al. 2011; Chaves et al. 2014).

2.5.1 Mode I fracture tests

Double Cantilever Beam (DCB) test is the most used for mode I opening forces. The test is well described by the standard ASTM D3433 and ISO 25217 for measuring the critical fracture energy in pure mode I, G_{Ic}, of bonded joints.

As the name suggests, DCB specimens are composed by two substrates (the double cantilever) bonded along their length (Figure 2.7), except for an initial region at one end exempt of adhesive, the pre-crack a_0. (da Silva et al. 2012; da Silva et al. 2007; da Silva et al. 2011).

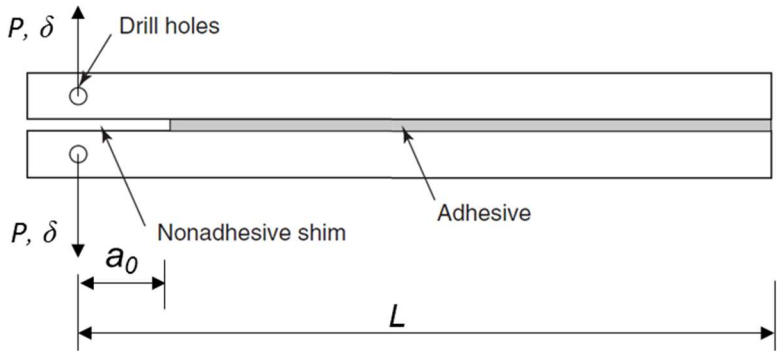

Figure 2.7 – DCB specimen schematics (adapted from da Silva et al. 2012)

According to ISO 25217, the specimen is initially loaded at a constant crosshead displacement rate until the crack has grown a short distance. Typically, this might correspond to about 2-5mm of crack growth. Then, loading is stopped and the specimens is fully unloaded. This is called the precracking stage. Its importance relies on the fact that it creates the peak of energy necessary for a stable crack propagation (da Silva et al. 2012).

The load is applied to the specimen by opening the beams through the holes drilled on the adherend and the test displacement rate goes generally between 0.5 and 3 mm/min, depending on the specimen's geometry and material. During the experiment, the load P and the displacement δ are recorded (da Silva et al. 2007).
Making use of the CBBM data reduction scheme, the fracture toughness in mode I is given by:

$$G_{\mathrm{Ic}} = \frac{6\mathrm{P}^2}{B^2 h^3}\left(\frac{2a_e^2}{E_f} + \frac{h^2}{5G_{13}}\right) \tag{2.9}$$

where h and B represent, respectively, the height and width of the specimen arm, and G_{13} the shear modulus. The flexural modulus, E_f, is obtained using the measured initial compliance (C_0)

$$E_f = \left(\mathrm{C_0} - \frac{12(\mathrm{a_0} + |\Delta|)}{5\mathrm{BhG}}\right)^{-1} \frac{8(\mathrm{a_0} + |\Delta|)^3}{Bh^3} \tag{2.10}$$

where Δ is the crack length correction accounting for the beam root rotation and deflection effects.

$$\Delta = h\sqrt{\frac{E}{11G_{13}}\left[3 - 2\left(\frac{\Gamma}{1+\Gamma}\right)^2\right]} \tag{2.11}$$

and

$$\Gamma = 1.18\frac{\mathrm{E}}{\mathrm{G_{13}}} \tag{2.12}$$

The initial compliance is determined using the definition of compliance according to this approach

$$\mathrm{C_I} = \frac{6\mathrm{a_e^3}}{EBh^3} + \frac{12\mathrm{a_e}}{5\mathrm{BhG_{13}}} \tag{2.13}$$

considering the crack equivalent concept, a_e, accounting on the FPZ effects ($a_e = a + |\Delta| + \Delta a_{\mathrm{FPZ}}$) (de Moura et al. 2008; da Silva et al. 2011)

$$a_e = \frac{1}{(6\alpha)}A - \frac{2\beta}{A} \tag{2.14}$$

where

$$\alpha = \frac{8}{Bh^3E_f}; \beta = \frac{12}{5BhG_{13}}; \gamma = -C \tag{2.15}$$

and

$$A = \left(\left(1 - 108\gamma + 12\sqrt{3\frac{(4\beta^3 + 27\gamma^2\alpha)}{\alpha}}\right)\alpha^2\right)^{\frac{1}{3}} \tag{2.16}$$

2.5.2 Mode II fracture tests

Fracture characterization under pure mode II tests are still not well addressed due to some particular aspects inherent to the tests usually performed, such as the complex apparatus needed and friction effects. ENF appears to be the most suitable test for the G_{IIc} characterization despite of the problems related to unstable crack growth in some types of adhesives and to the crack monitoring (de Moura et al. 2009).

The specimens of the ENF test are similar to the ones used for the DCB experiment, already described in the section 2.5.1. Here, the procedure consists in loading the simply supported beam at midlength, with a precrack at one of the edges as shown in Figure 2.8 (da Silva et al. 2012). The load applied creates almost a pure shear stress state at the crack tip and makes the

adherends deform elastically, which allows for shear characterization (Campilho & da Silva 2014).

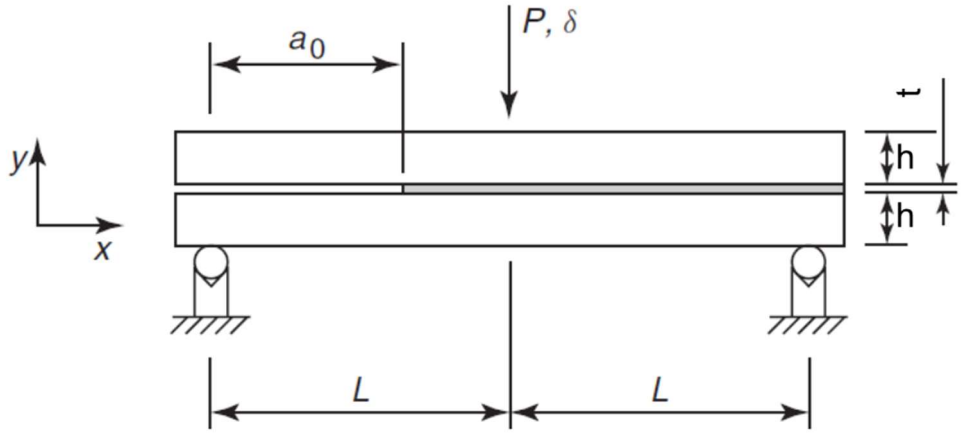

Figure 2.8 – Schematic representation of the ENF test (da Silva et al. 2012).

The same as for DCB testing, CBBM data reduction scheme is also implemented for the ENF specimen, allowing to increase the accuracy of the fracture energy measurements without crack length monitoring during propagation. The procedure followed by this method accounts on several aspects not included in beam theory, such as the stress concentrations near the crack tip, contact between the specimen arms and root displacement and rotation effects (de Moura et al. 2009).

Using the Irwin-Kies relation, the fracture energy in pure mode II is given by

$$G_{\mathrm{IIc}} = \frac{9\mathrm{P}^2 a_e^2}{16B^2 E_f h^3} \tag{2.17}$$

Considering the specimen's compliance using beam theory

$$C_{II} = \frac{3a^3 + 2L^3}{8EB\,h^3} + \frac{3L}{10G_{13}Bh} \tag{2.18}$$

The flexural modulus can be calculated from equation 2.18, using the initial compliance C_0 and the initial crack length a_0 (de Moura et al. 2009)

$$E_f = \frac{3\mathrm{a}_0^3 + 2L^3}{8Bh^3 C_{0corr}} \tag{2.19}$$

where

$$C_{0corr} = C_0 - \frac{3L}{10G_{13}Bh} \tag{2.20}$$

Substituting E_f and $a_e$in the place of E and a, respectively, in equation 2.18, it can be written

$$a_e = a + \Delta_{FPZ} = \left[\frac{C_{corr}}{C_{0_{corr}}} a_o^3 + \frac{2}{3}\left(\frac{C_{corr}}{C_{0_{corr}}} - 1\right) L^3\right]^{1/3} \tag{2.21}$$

2.5.3 Mixed-mode I+II fracture tests

The importance of the fracture behaviour characterization under mixed-mode I/II loads in adhesive joints has led to the development of several tests (Table 2.2)

Table 2.2 - Fracture tests applied for the mixed-mode fracture characterization (Chaves et al. 2014).

Test name	Test scheme	Global mixity φ (º)
Asymmetric Double Cantilever Beam (ADCB)		$0<\varphi<34$
Single Leg Bending (SLB)	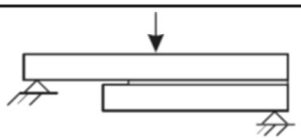	≈ 41
Crack Lap Shear (CLS)		≈49
Asymmetric Tapered Double Cantilever Beam (ATCB)		≈20
Mixed Mode Bending (MMB)	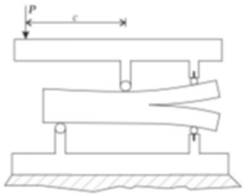	$\varphi=f(c)$
Spelt Loading Jig (SPELT)	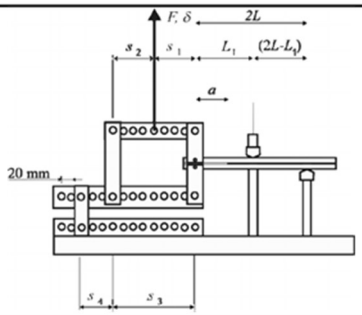	$\varphi=f(s_1, s_2, s_3, s_4)$

When it comes to mixed-mode loading, the ratio of mode I and mode II in each case must be defined using some parameter. For that purpose, the mixed-mode phase angle, φ, is given by

$$\varphi = \tan^{-1}\sqrt{\left(\frac{K_{II}}{K_I}\right)} = \tan^{-1}\sqrt{\left(\frac{G_{II}}{G_I}\right)} \qquad (2.22)$$

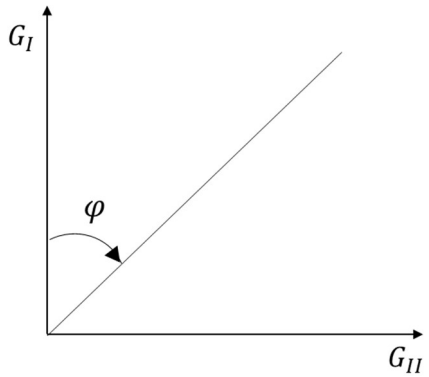

Figure 2.9 – Phase angle between G_I and G_{II}.

Despite of all the tests that exist for this characterization, the majority of them require a specific specimen and only provide results for one mixed-mode combination.

The Mixed Mode Bending (MMB) is the only standard test available to evaluate the mixed-mode toughness (defined in ASTM D6671). This test allows the measurement for different mixed-mode ratios, however, it was originally designed for delamination with composites, making it inappropriate for stiffer aluminum or steel adherends (Chaves et al. 2014).

In order to characterize the fracture behaviour of adhesive joints in a wide range of fracture modes, an apparatus was developed by Chaves et al. (Figure 2.10). This apparatus is an evolution of the already existent Spelt loading jig (Fernlund & Spelt 1994) with the difference that its operation does not use the crack length measurement, instead it uses the displacement given by the LVDT's (linear variable differential transformer). It also has the advantage of having the specimen placed inside of the structure, reducing the overall dimensions and simplifying the test operations (Chaves et al. 2013).

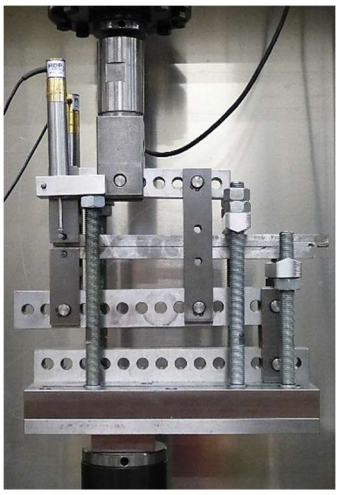

Figure 2.10 – Mixed-mode apparatus.

This apparatus can be configured for phase angles between the two pure loading modes (mode I and mode II) simply by changing the length of the beams that hold and apply the load to the specimens (distances $s_1 - s_2 - s_3 - s_4$ in Figure 2.11).

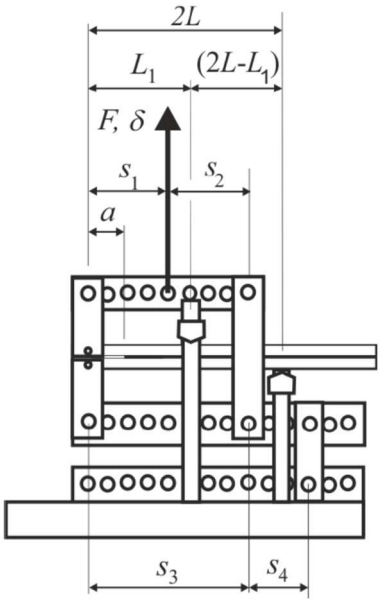

Figure 2.11 – Schematics of the mixed-mode apparatus (Chaves et al. 2013)

Changing those distances, the loads F_1 and F_2 applied to the upper and lower adherends (represented in Figure 2.12) become different. The relationship between the forces applied by each beam of the apparatus and the mixed-mode phase angle is given by

$$\varphi_{apparatus} = \tan^{-1} \frac{\sqrt{3}\left(\frac{F_1}{F_2}+1\right)}{2\left(\frac{F_1}{F_2}-1\right)} \tag{2.23}$$

The loading applied to the specimen is a combination of mode I and mode II. Analyzing the two corresponding components (Figure 2.12), mode I loading can be viewed as a DCB specimen and mode II as an ENF loaded asymmetrically (Chaves et al. 2013).

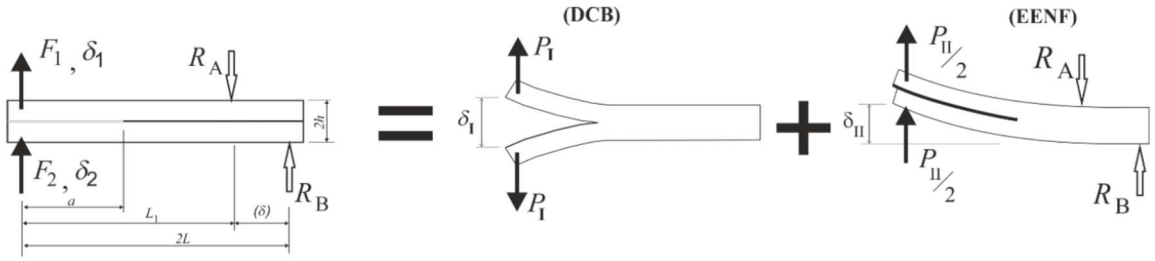

Figure 2.12 – Schematic representation of the specimen loading with mode I and mode II partition (Chaves et al. 2014).

The specimens used to perform these tests are similar to those required for DCB or ENF tests, which reveals to be another advantage of this device.

P-δ curve is obtained from a universal testing machine and the two LVDT's connected to each beam measure its displacement (Figure 2.11). The specimen is placed in the apparatus through pins inserted in drilled holes and contacting with the LVDT's.

The load components F_1 and F_2 can be obtained by the applied load and loading arm (Figure 2.10)

$$F_1 = F\frac{s_1}{s_3}\ ; F_2 = F\frac{s_1 s_4}{s_3(s_3+s_4)} \tag{2.24}$$

From Figure 2.12 it can be seen that

$$P_I = \frac{F_1 - F_2}{2};\ P_{II} = F_1 + F_2 \tag{2.25}$$

and

$$\delta_I = \delta_1 - \delta_2\ ;\ \delta_{II} = \frac{\delta_1 + \delta_2}{2} \tag{2.26}$$

Applying the CBBM data reduction scheme, the strain energy release rate under mixed-mode (G_T) can be achieved in an easier way, just considering the compliances of the pure modes

$$C_I = \frac{\delta_I}{P_I} = \frac{8a^3}{Bh^3E} + \frac{12a}{5BhG} \tag{2.27}$$

$$C_{II} = \frac{\delta_{II}}{P_{II}} = \frac{3a^3 + 2LL_1^2}{2Bh^3E} + \frac{6LL_1}{5BhG(2L - L_1)} \tag{2.28}$$

It is verified, as expected, that equation 2.27 is compatible to Equation 2.13 obtained for a DCB specimen and Equation 2.28 is consistent with Equation 2.18 for an ENF specimen when L_1 equals L.

Fracture toughness for mode I and mode II are calculated using the following expressions:

$$G_{\mathrm{I}} = \frac{6\mathrm{P}_{\mathrm{I}}^2}{B^2h^3}\left(\frac{2a_{eI}^2}{E_f} + \frac{h^2}{5G_{13}}\right) \tag{2.29}$$

$$G_{\mathrm{II}} = \frac{9\mathrm{P}_{\mathrm{II}}^2 a_{eII}^2}{16B^2E_fh^3} \tag{2.30}$$

The same considerations used for the DCB and ENF specimens regarding the flexural modulus and crack equivalent concept are aplied to Equations 2.29 and 2.30 (Chaves et al. 2013).

The resistance curves, determined for each mode, allow the identification of the energy release rates values, providing the mode-mixity and the total fracture energy of the test (Chaves et al. 2014; da Silva et al. 2011).

2.5.3.1 Fracture envelopes

Fracture envelopes are graphic representations of the strain energy release rate in mode I and mode II for phase angles between the two loading modes. The outline defining fracture envelopes allows the definition of an energetic failure criterion (Chaves et al. 2011). The determination of such criteria in adhesives is extremely important once it gives information of the strength by equating energy release rate to the toughness at the appropriate phase angle (Stamoulis et al. 2014).

Chaves et al. characterized the fracture behaviour of bonded joints using the mixed-mode apparatus under different loading conditions. Figure 2.13 presents seven scenarios analyzed considering the linear and quadratic failure energetic criteria.

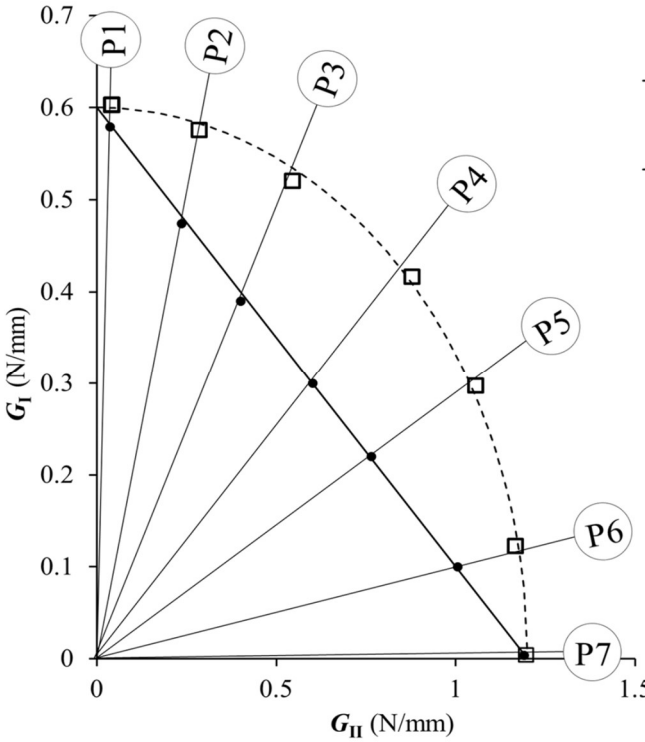

	Jig arrangement			
Scenarios	s_1 (mm)	s_2 (mm)	s_3 (mm)	s_4 (mm)
P1	100	40	140	-60
P2	120	40	160	-120
P3	40	120	160	40
P4	60	80	140	60
P5	60	80	140	120
P6	40	40	80	100
P7	100	40	140	80

Figure 2.13 – Fracture envelope for the seven scenarios (Chaves et al. 2013).

2.6 Fatigue

The study of fatigue in adhesive joints is extremely important since many of common service failures occur due to an extensive exposure to cyclic conditions. In fact, those cyclic loadings can cause failure for lower load values than those required to cause quasi-static failure (da Silva et al. 2007; Fernández 2008). Adhesive joints present, generally, better fatigue properties over other conventional joining methods like mechanically fastened joints. Thus, in some cases, adhesive is interposed to conventional joints in order to improve the mechanical behaviour (da Silva et al. 2007; de Moura et al. 2008).

2.6.1 Fatigue load

Fatigue loadings vary cyclically with time. The characterization of this variation is usually done by means of some parameters as seen in Figure 2.14. The fatigue spectrum is usually defined in terms of applied load or displacement or even considering cyclic stress, for more complex structures. The majority of the experiments establish a constant amplitude for the load applied, and the sinusoid may be defined by the frequency f (number of cycles per unit of time) and two load or stress parameters. The load parameters usually used to describe fatigue spectra are the maximum load (P_{max}) and load ratio ($R = P_{min}/P_{max}$). There are also other parameters that can be used in their place such as the minimum load (P_{min}), the mean load (P_m) or load range ΔP as represented in Figure 2.14 (da Silva et al. 2011; Fernández 2008).

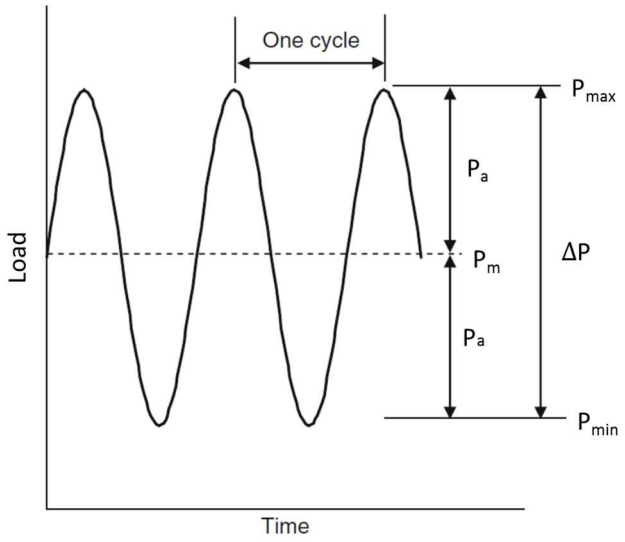

Figure 2.14 – Typical cyclic loading parameters (adapted from da Silva et al. 2011).

2.6.2 Prediction methods

The assessment of fatigue in polymeric materials can become quite complex. It depends on several variables such as cracks, porosities, environmental factors, geometry, *etc.* (da Silva et al. 2007; de Goeij et al. 1999). One of the main factors that influences the fatigue behaviour is the fracture toughness of the adhesive. A tough adhesive often appears to be more resistant to fatigue since it can store more energy, which is released during the reverse stage of the cycle, not causing excessive deformation (da Silva et al. 2007).

In order to improve the structure's design, either for economic and reliability aspects, it is important to determine the lifetime and the resistance to fatigue (da Silva et al. 2007; Fernández 2008). Within this context, different theories intend to estimate the fatigue behaviour of adhesive joints, performing tests that reveal to be expensive and not always applicable (da Silva et al. 2007). Some use tests to obtain the intrinsic properties of the adhesive, though, these results cannot be used to predict the fatigue performance since it depends strongly on the adhesive bond line thickness (de Goeij et al. 1999). Others use the stress-life approach to obtain the classical S-N fatigue curves (Figure 2.15) performing tests either in simple specimens, in real or in sub-scales structures. However, as the results of simple specimens are difficult to extrapolate to real joints, this investigation of fatigue properties in joints become expensive and possible unsuitable (da Silva et al. 2007; de Goeij et al. 1999).

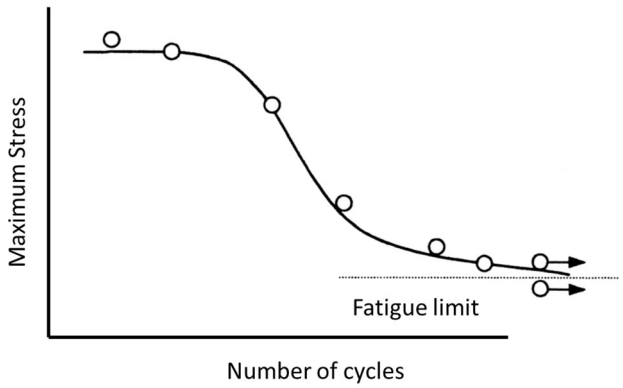

Figure 2.15 – S-N curve (adapted from De Goeij et al. 1999).

Structural joints under load present cracks that initiate and propagate along the weakest path of the component. Studies focused on fracture mechanics lead to another approach, widely used

for predicting the fatigue behaviour: the Fatigue Crack Growth (FCG) (Vassilopoulos et al. 2014). This theory assumes the presence of a pre-crack on a structure subjected to cyclic loading and analyses the crack propagation (da Silva et al. 2007; de Goeij et al. 1999). The strain energy release rate G can be related to the fatigue crack growth rate by fracture mechanics tests. It was shown that the plotted expression of the crack growth rate per cycle, da/dN , and the variation of G over time in logarithmic scale has a sigmoidal shape similar to previously observed studies of FCG in metals and polymers, and that it follows the power law for a large range (de Goeij et al. 1999; Fernández et al. 2011). Figure 2.16 shows a typical propagation curve.

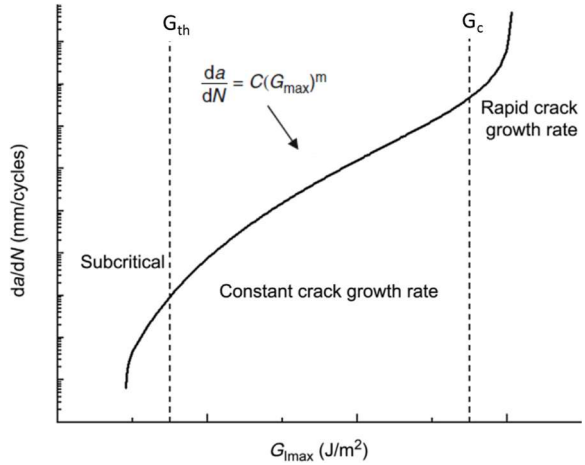

Figure 2.16 – Typical fatigue crack growth curve (adapted from Vassilopoulos et al. 2014).

Three different stages can be distinguished from the fatigue crack growth curve. The initial part, located bellow the energy release rate threshold, G_{th}, is considered to have negligible crack growth. After this threshold, crack propagation takes place and the growth assumes a linear shape that fits well with the Paris law relationship:

$$\frac{da}{dN} = C\left(\frac{\Delta G}{G_c}\right)^m \tag{2.31}$$

where C and and m are constants obtained by the adjustment of experimental values. The third region starts when the crack growth becomes unstable and leads to ultimate failure (da Silva et al. 2007; Fernández et al. 2011). The value of G_{th} and the slope of the Paris law are the key parameters of this curve. Usually, the design methodologies comprising fatigue damage in bonded joints use one or both of these parameters (Renart et al. 2014).

In real joints under mixed-mode loading, the crack propagation rate is a function of the combined effect of G_I and G_{II}. So, it is appropriate to use the total strain energy release rate G_T for derivation of the FCG curves since for most common mixed-mode tests, individual G_I and G_{II} are much more difficult to calculate. Experiments in the literature (Fernández 2008; Pirondi & Nicoletto 2006; Carraro et al. 2013; Hafiz et al. 2013) show that the mixed-mode angle significantly affects the FCG curves obtained for different joints and materials. Although, different behaviors have been verified and there is no agreement on the mode-mixity effect in the FCG curve (Shahverdi & Vassilopoulos 2014). Figure 2.17 shows different studies on mixed-mode fatigue specimens.

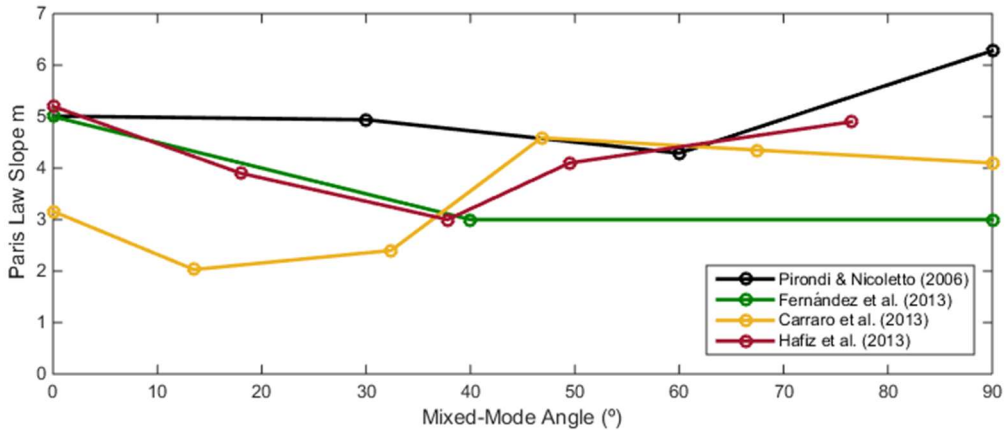

Figure 2.17 – Paris law parameter m as a function of the mixity.

Fernández et al. (2013) studied a mixed-mode I+II fatigue failure criterion to predict the behaviour of composite bonded joints under any mode-mixity using SLB specimens. It was found that the crack propagation rate in mode I is much higher than in mixed-mode I+II ($\varphi \approx 41°$) and mode II conditions, revealing that the presence of mode II loadings delay the crack advance under fatigue load conditions (Fernández et al. 2013).

2.6.3 Fatigue testing

Fatigue testing aims to reproduce the conditions applied to bonded joints during service. Performing those tests, it is possible to assess the fatigue behavior by determining some parameters that characterize crack initiation and propagation (Renart et al. 2014):

- The number of cycles at which the crack starts to propagate, for a given load (usually expressed in terms of G);
- The crack growth rate dependence on G (FCG curves);
- The threshold value of G, G_{th}.

The procedure consists of applying the load cyclically, thus causing subcritical crack propagation in the adhesive. The load required is lower than the value used for static conditions and it is introduced by controlling the load or the displacement (Renart et al. 2014). Generally, a ratio of the failure load is established as the maximum load applied in fatigue (P_{max}), and the P_{min} is obtained by the load ratio R.

Standard fracture mechanics tests, such as DCB, are used to generate fatigue crack curves (da Silva et al. 2011). Therefore, the specimens used for fatigue tests are the same as those used for quasi-static tests, described in section 2.4.

The same way as for the static fracture tests, CBBM data reduction scheme is also applied to fatigue tests to overcome the difficulties inherent to the crack length monitoring (Fernández et al. 2011). As referred before (section 2.4) this methodology also takes in account other aspects not considered in classical methods, such as the energy dissipation at the FPZ.

Though, the fracture energies are calculated using the same considerations leading to the same equations:

for mode I (DCB):

$$G_{\mathrm{I}} = \frac{6\mathrm{P}^2}{B^2 h^3}\left(\frac{2a_e^2}{E_f} + \frac{h^2}{5G_{13}}\right) \tag{2.32}$$

for mode II (ENF):

$$G_{\mathrm{II}} = \frac{9\mathrm{P}^2 a_e^2}{16B^2 E_f h^3} \tag{2.33}$$

and for mixed-mode I+II (mixed-mode apparatus):

$$G_{\mathrm{I}} = \frac{6\mathrm{P}_{\mathrm{I}}^2}{B^2 h^3}\left(\frac{2a_{eI}^2}{E_f} + \frac{h^2}{5G_{13}}\right); G_{\mathrm{II}} = \frac{9\mathrm{P}_{\mathrm{II}}^2 a_{eII}^2}{16B^2 E_f h^3} \tag{2.34}$$

The determination of the fatigue crack growth rate, da/dN can be done using the secant method, recommended in standard ASTM E647. This method consists in evaluating the variation of the equivalent crack length as a function on the number of cycles considering a discrete number of measurements (n) during the test

$$\left(\frac{da}{dN}\right)_{\overline{a_e}} = \frac{(a_{e_{i+1}} - a_{e_i})}{(N_{i+1} - N_i)} \tag{2.35}$$

where

$$\overline{a_e} = \frac{(a_{e_{i+1}} - a_{e_i})}{2} \tag{2.36}$$

and i represents the ith measurement of the test ($0 \ll i \ll n$), resulting in an average value of the rate in an increment. The corresponding equivalent crack length, for each G is the average value of the limits of the increments (Equation 2.36) (Fernández et al. 2013).

3 Experimental details

The work presented here is inserted in an external project requested by HONDA R&D. Therefore, some information must be kept confidential and that is the reason why the adhesives used in this study are not disclosed.

3.1 Materials

3.1.1 Adhesives

Three one-component epoxy adhesives (Adhesive 1, Adhesive 2 and Adhesive 3), selected by HONDA R&D, were used to perform the static analysis. The study of fatigue only comprises Adhesive 2 and Adhesive 3 due to limitations of available time.

Following the supplier indications, the curing cycle is the same for the three adhesives and is presented in Figure 3.1. The adhesives cure at 170ºC during 30 minutes.

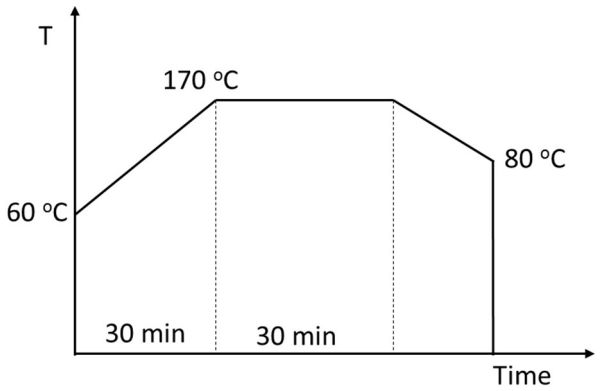

Figure 3.1 – Curing profile of the three adhesives (supplier specifications).

3.1.2 Adherends

The substrates used in this study were steel substrates. The selection of the steel DIN 40CrMnMo7 took in consideration the value of yield strength (Table 3.1) which is high enough to keep the adherends in the elastic range.

Table 3.1 – Young's modulus and yield strength of DIN 40CrMnMo7 steel.

Young's modulus [GPa]	Yield strength [MPa]
210	900

3.2 Specimen geometry

The specimen geometry used to perform the fracture and fatigue tests follows the ASTM D-3433-99 (Figure 3.2):

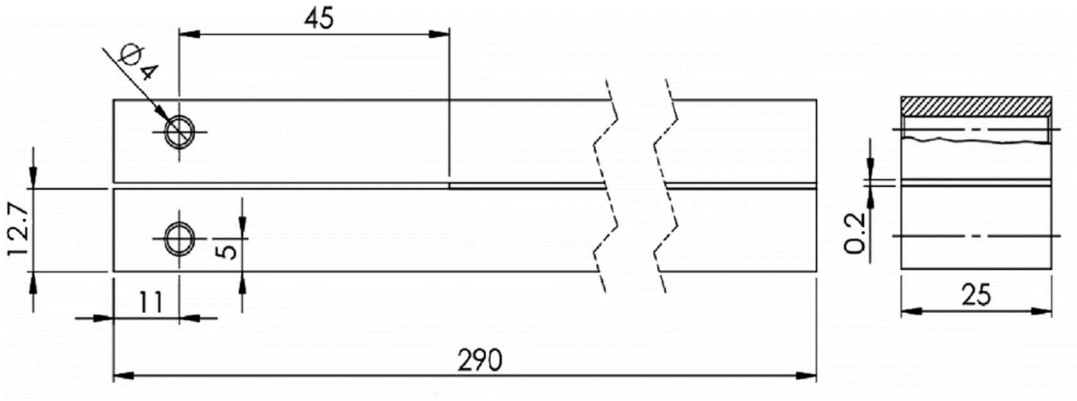

Figure 3.2 – Specimens geometry according to ASTM D-3433-99 (dimensions in millimeters)

3.3 Specimen manufacture

The preparation of the specimens includes several stages that must be respected.

First of all, the mold had to be prepared, cleaning its surface from residues and using a release agent (FREKOTE 770NC) to prevent adhesion to the mold.

To assure a strong bond, the surfaces of the steel substrates were first sandblasted and then degreased with acetone. No primer or any other type of surface treatment was applied to the substrates.

The adhesive was applied to the adherends. The thickness of the adhesive layer is established by spacers positioned between the adherends and the proper alignment between adherends should be respected when placed in the mold (Figure 3.3).

Figure 3.3 – Adhesive deposition.

As represented in Figure 3.4, a 0.1 mm thick razor blade was bonded in the middle of two 0.05 mm thick steel to ensure the 0.2 mm of thickness required and also to introduce a defect in the joint, promoting a cohesive crack propagation. On the other end, a 0.2 mm thick steel gauge is used to guarantee the thickness all over the bonding line.

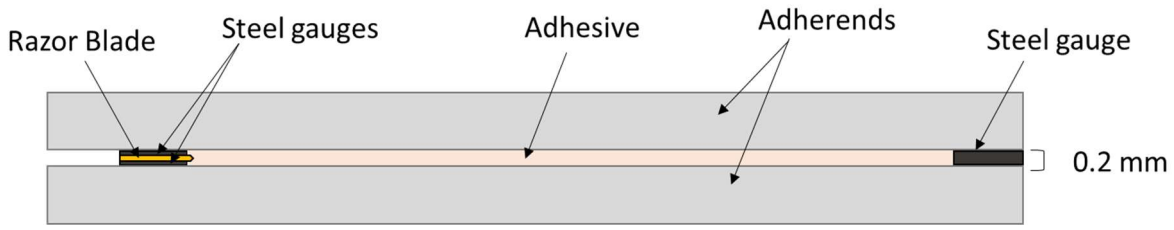

Figure 3.4 – Scheme of the specimens used.

After adhesive deposition, the joints were cured in a hot press at a constant pressure of 15 bar for approximately 30 min at 170ºC. After curing, the adhesive excess at the side edges was carefully removed, first by machining and them using sandpaper.

Before testing, a pre-crack was done to promote stable crack propagation: opening loads were applied to the specimen at a constant crosshead of 0.2 mm/min until the crack originated by the razor blade had grown a short distance. The loading was then stopped, the razor blade was removed and the crack length was registered.

3.4 Tensile tests

Bulk tensile tests are the most common tests performed to provide the intrinsic properties of materials. The test consists on applying an uni-axial and uniform load to the specimen, obtaining the stress and strain curve (Figure 3.5). From this curve the properties of the adhesive, such as tensile strength (σ_e), failure strain (ε_r) and Young's modulus (E) are determined (da Silva et al. 2012).

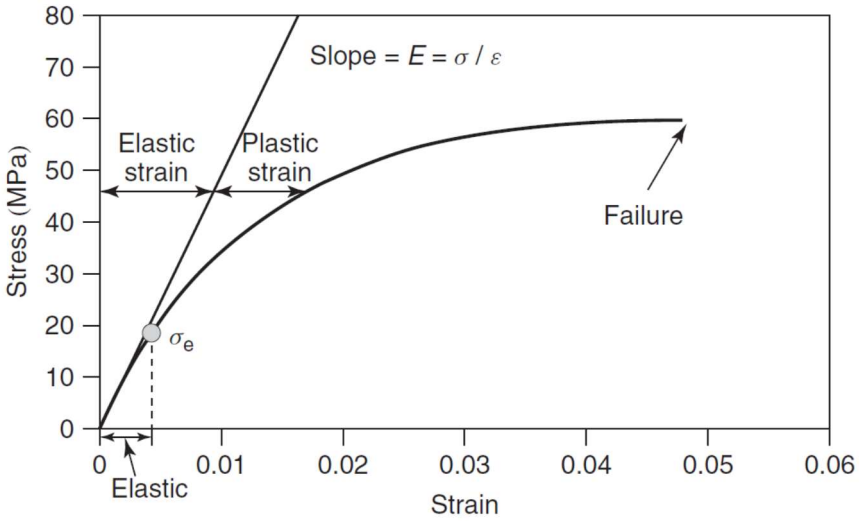

Figure 3.5 – Typical tensile stress-strain curve of an adhesive (da Silva et al. 2012).

With the purpose of modelling the experimental results through a numerical analysis, it is required to determine the strength properties of the adhesives. Though, in a representative way, it was performed bulk tensile tests for Adhesive 3 to proceed with the numerical analysis using that intrinsic properties.

The test was performed at room temperature with a constant displacement rate of 1 mm/min and using specimens with the geometry represented in Figure 3.6. The strain was measured using an extensometer.

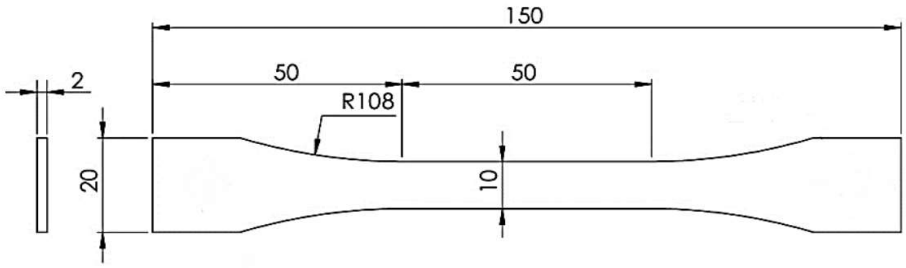

Figure 3.6 – Bulk tensile specimens' geometry according to ASTM D-638 (dimensions in millimeters).

3.5 Fracture tests

3.5.1 Mode I tests (DCB)

DCB tests were performed to assess the fracture behaviour under pure mode I and to determine the critical value of the energy release rate, G_{Ic}. The used constant displacement rate was 0.2 mm/sec and three specimens were tested.

The loading and displacement values were recorded during the test and the R-curves were achieved considering equivalent crack length concept of the CBBM methodology. To calculate the value of G_{Ic} equation 2.9 was used.

Figure 3.7 shows the experimental setup for mode I tests.

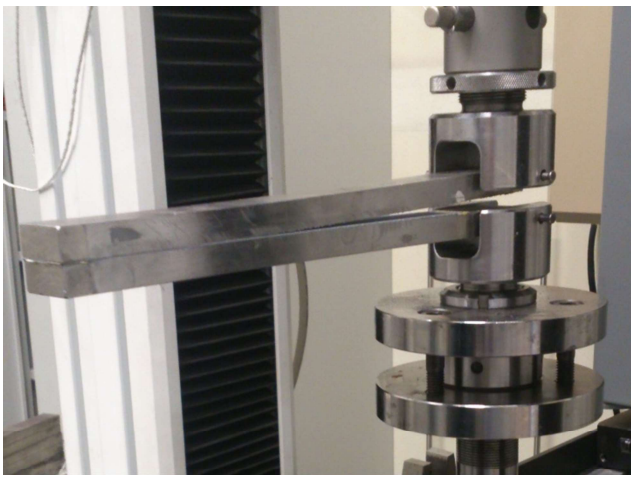

Figure 3.7 – Experimental setup employed for DCB testing.

3.5.2 Mode II tests (ENF)

Regarding the assessment of mode II fracture behaviour, ENF tests were carried out. The same constant displacement rate of 0.2 mm/sec was respected and three specimens for each adhesive were tested in mode II.

Mode II tests have a singular aspect related to the applied shear load: a friction generated between the adherends, in the initial region exempt of adhesive, can lead to overestimations of the G_{IIc} since more energy would be need for the crack propagation. To avoid the misleading friction, a common artifice was implemented: a Teflon® folded film with oil droplet in the middle was introduced in the initial part of the specimen, as shown in Figure 3.8, providing more realistic results.

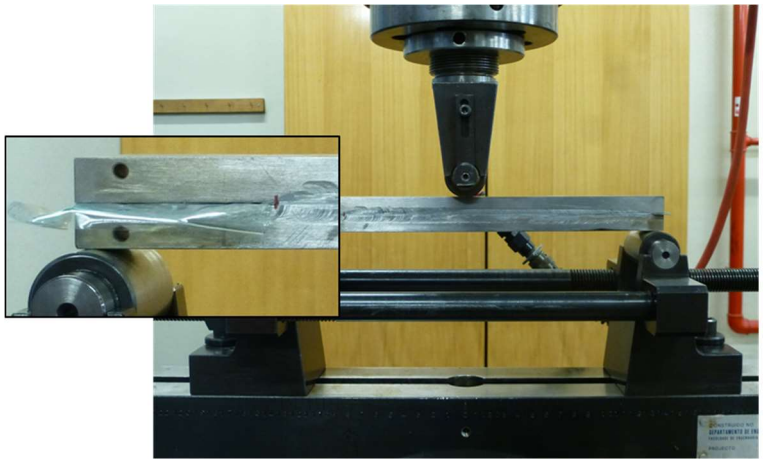

Figure 3.8 – ENF setup with Teflon® film in detail.

The load was applied in the middle of the specimen and the supports were settled at the same distance from the load point, $L = 140$mm. Therefore, the load was applied symmetrically.

As well as for the mode I analysis, the critical value of G_{IIc} was determined from the R-curves obtained from the use of the equivalent crack length concept of CBBM data reduction scheme (Equation 2.17).

3.5.3 Mixed-mode tests

The mixed-mode tests were performed using a mixed-mode apparatus (Portuguese patent nº108188 B) that measures the fracture behaviour for various combinations of mode I and mode II (different mixed-mode angle, φ) by simply changing the length of the beams supporting the specimen (s_1-s_2-s_3-s_4) and the locus of the fixation (L_1 and $2L$) represented in Figure 3.9.

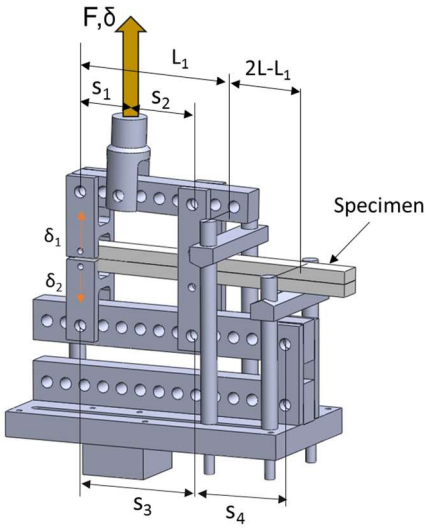

Figure 3.9 – Scheme of the mixed-mode apparatus used.

The mixed-mode configurations used for the quasi-static tests are presented in Table 3.2.

Table 3.2 - Configurations performed for fracture tests in quasi-static conditions.

φ [º]	s_1 [mm]	s_2 [mm]	s_3 [mm]	s_4 [mm]	L_1 [mm]	$2L$ [mm]	Adhesive
0	60	100	160	-100	205	230	2,3
22.2	60	100	160	-60	205	230	1,2,3
56.6	60	80	140	80	180	230	2,3
61.7	40	60	100	120	165	220	1,2,3
86.9	100	40	140	80	170	270	1,2,3

As it is visible in Figure 3.10, a wide range of mixed-mode combinations were studied.

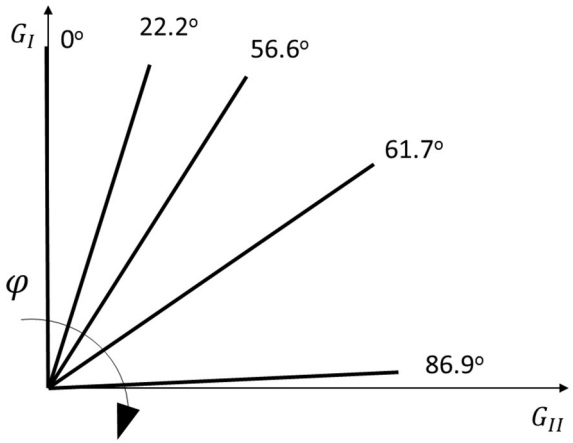

Figure 3.10 – Scheme of the mixed-mode angles studied represented in the fracture envelope.

The same way as for the pure modes, the displacement rate was kept 0.2 mm/sec for every performed test. For each φ of each adhesive, at least three specimens were tested.

The crack equivalent concept was used to reach the critical value of the energy release rate in mode I and in mode II for each combination (Equations 2.29 and 2.30). LVDT's connected to each adherend registered δ_1 and δ_2 (Figure 3.9).

Figure 3.11 represents two of the experimental setups employed.

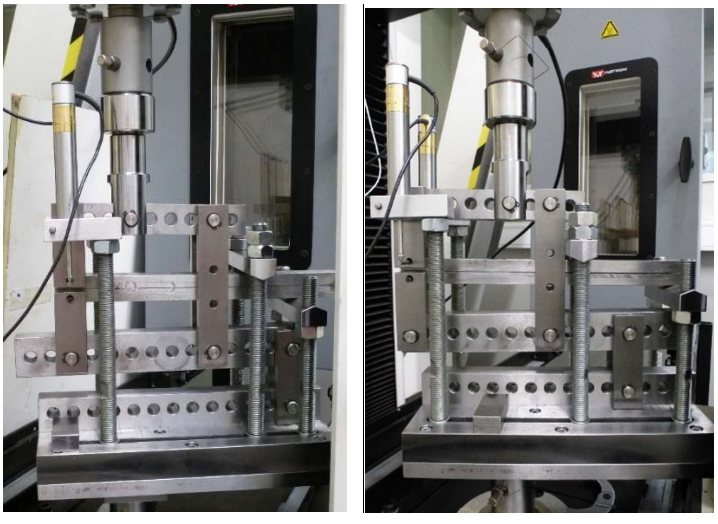

Figure 3.11 – Mixed-mode apparatus for the configuration of φ=56.6º (left) and φ=86.9º (right).

3.6 Fatigue tests

In order to characterize the fatigue crack growth propagation in mode I, mode II and mixed-mode I+II conditions, the same tests used in the fracture study were performed applying a cyclic loading.

The maximum load in fatigue, P_{max}, was established as 70% of the failure load determined in the respective static test. The minimum load, P_{min}, was obtained by a load ratio of 10% of the value of P_{max}.

The frequency value of the experiments was around 1-2 Hz, providing the loading machine the necessary time to course from the minimum to the maximum displacement that is required to apply the loading cycle.

Only adhesive 2 and 3 were used for this analysis, due to time restrictions. In order to study adhesives with different behaviour, the selection included a brittle adhesive (Adhesive 3) and another more ductile (Adhesive 2).

3.6.1 Mode I tests (DCB)

DCB fatigue tests were performed to obtain the FCG curves and to determine the Paris law parameters under pure mode I.

The fatigue parameters applied in mode I fatigue tests are resumed in Table 3.3.

Table 3.3 – Experimental parameters used for DCB fatigue tests.

Adhesive	Frequency [Hz]	Failure load [N]	P_{max} [N]	P_{min} [N]	No. of specimens
2	1	2350	1900*	190	4
3	1	2000	1400	140	4

*80% of the failure load was considered in this case

During the test, the load and displacement were registered and the determination of the FCG curves and Paris law parameters were done. The secant method was used to determine the FCG (Equation 2.35) and CBBM data reduction scheme was applied to achieve the energy release rates without the dependency on the visual measurement of the crack length, which in fatigue is even more difficult to monitor (Equation 2.9).

The same setup of the static tests was used for these fatigue tests (Figure 3.7)

3.6.2 Mode II tests (ENF)

ENF fatigue tests were performed to obtain the FCG curves and determine the Paris law parameters under pure mode II.

The fatigue parameters of the mode II fatigue tests are resumed in Table 3.4.

Table 3.4 – Experimental parameters used for ENF fatigue tests.

Adhesive	Frequency [Hz]	Failure load [N]	P_{max} [N]	P_{min} [N]	No. of specimens
2	2	15000	10500	1050	4
3	2	20000	14000	1400	4

The experimetal setup was the same as for ENF under static conditions and it is represented in Figure 3.8. Attention was paid to the use of a Teflon® film, explained in section 3.5.2 to avoid friction in the initial area of the specimen.

Data analysis carried out for these tests included the same steps followed for mode I. The determination of the energy release rate using CBBM (Equation 2.17) as well as the secant method for the fatigue crack growth (Equation 2.35) allowed to obtain the FCG curves.

3.6.3 Mixed-mode tests

The performed mixed-mode tests to analyze the fatigue behavior were done through the use of the mixed-mode apparatus, the same used for the static study (Figure 2.10). This was the pioneering study of the use of this apparatus with the purpose of studying the fatigue behaviour.

The load P and displacement δ were registered during the tests as well as the displacement of the adherends tips, δ_1 and δ_2, represented in Figure 3.9. Knowing δ_1 and δ_2, it was possible to study the two components of loading separately, obtaining two FCG curves for each test. That procedure was done following the formulation of the mixed-mode apparatus and using CBBM to determine either G_I and G_{II} (Equations 2.29 and 2.30). The FCG was determined by the secant method (Equation 2.35).

Three mixed-mode combinations were studied in fatigue. One configuration closer to mode I, ($\varphi = 22.2^o$), one closer to mode II ($\varphi = 73.9^o$) and another in the middle of the two ($\varphi = 56.6^o$).

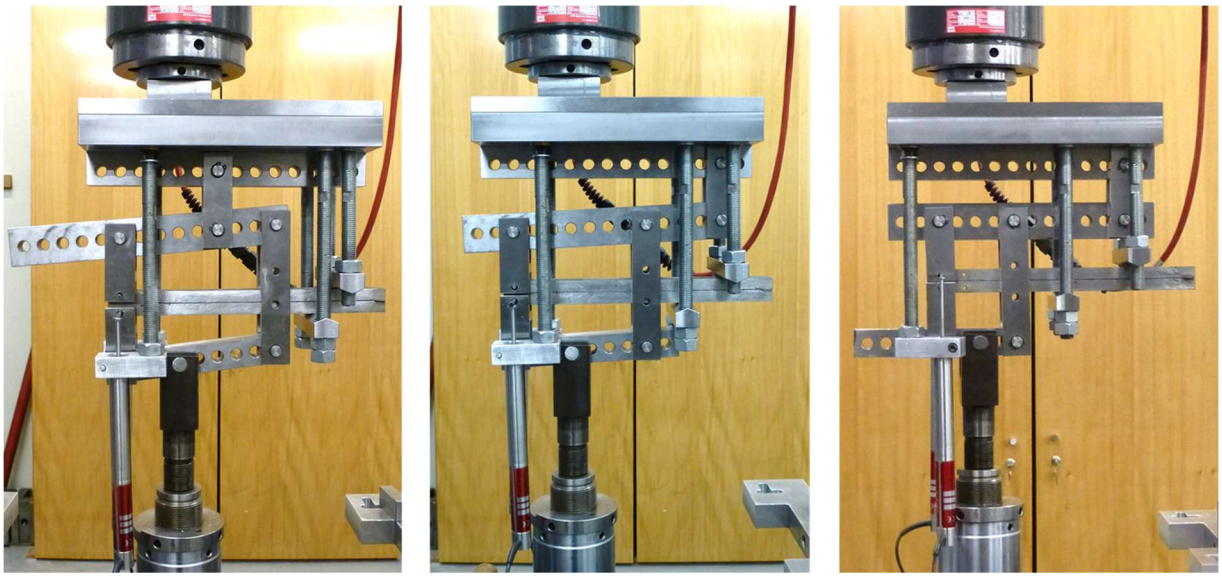

Figure 3.12 – Mixed-mode combinations studied in fatigue conditions: φ=22.2º (left), φ=56.6º (center), φ=73.9º (right).

Fatigue tests were done using a universal testing machine (Material Test System - MTS) which is fixed on the top and the movement is applied to the base. The mixed-mode apparatus was design for the opposite arrangement, so, the device had to be inverted. The results of this fixation were validated by performing static tests for the mixed-mode angle of $\varphi = 56.6^o$ using both configurations.

Table 3.5 resumes the fatigue parameters applied for the mixed-mode fatigue tests.

Table 3.5 – Experimental parameters used for mixed-mode fatigue tests.

φ [º]	Adhesive	Frequency [Hz]	Failure load [N]	P_{max} [N]	P_{min} [N]	No. of specimens
22.2	2	1	5700	3990	399	4
	3	1	5500	3850	385	3
56.6	2	1	7000	4900	490	3
	3	1	8000	5600	560	3
73.9	2	1	8000	5600	560	3
	3	1	10000	7000	700	3

The specifications of the apparatus for each tested mixed-mode angle as well as the representation of the angles in the fracture envelope can be found in Table 3.2 and Figure 3.10, respectively.

4 Results and discussion

4.1 Tensile tests

Tensile tests were done to know the properties of one adhesive and try to model its fracture behaviour. Only Adhesive 3 was characterized because the main focus was perfecting the model so that in the future the other adhesives could be accurately modelled. The stress-strain curves obtained are represented in Figure 4.1. The values for the Young's modulus, tensile strength and strain failure are shown are shown in Table 4.1

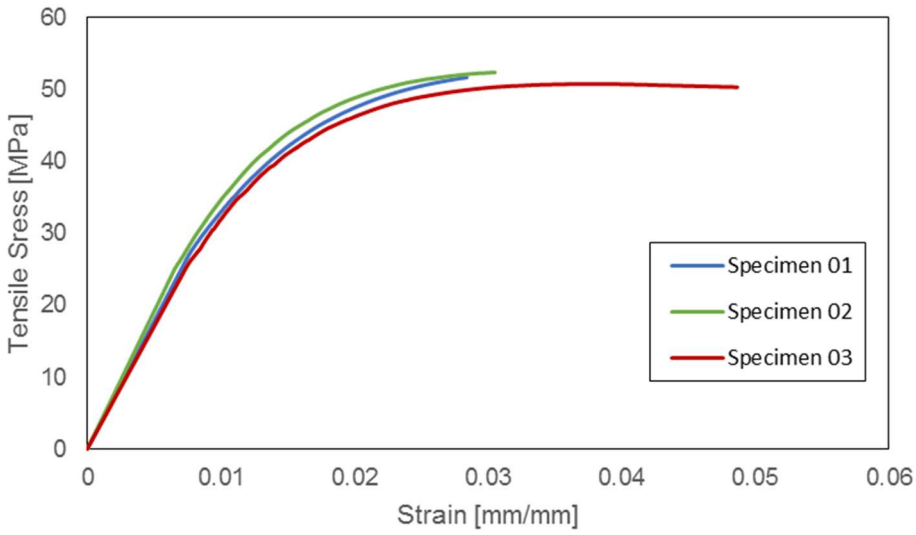

Figure 4.1 – Stress and strain curves obtained for Adhesive 3.

Table 4.1 – Experimentally obtained adhesive properties

Young's modulus (MPa)	Tensile strength (MPa)	Strain failure (%)
4041±407.99	51.64±0.71	2.67±0.94

The Young's modulus value obtained reveals that Adhesive 3 is a very stiff adhesive. The failure strain determined indicates brittle behaviour.

4.2 Fracture

Several tests under quasi-static conditions were done considering that three adhesives were studied for different load conditions. Representative curves of the fracture tests performed will be presented in the next sections and the totality of the results obtained can be found in APPENDIX A.

4.2.1 Mode I

DCB tests performed under static conditions led to the fracture energies of the three adhesives in mode I.

A representative load-displacement curve obtained for each adhesive can be seen in Figure 4.2. Observing the progress of this curves, there is an initial stage where the load increases until a peak value, the critical load. That initial rise corresponds to the storage of elastic energy. When the stored energy is enough to match the energy required for the onset crack propagation, the top of the curve is achieved and the load decreases as the propagation proceeds. Adhesive 3 presents some irregularities compared to the curve of the other two adhesives. This can be explained by an unstable crack propagation due to the brittle behaviour of the adhesive.

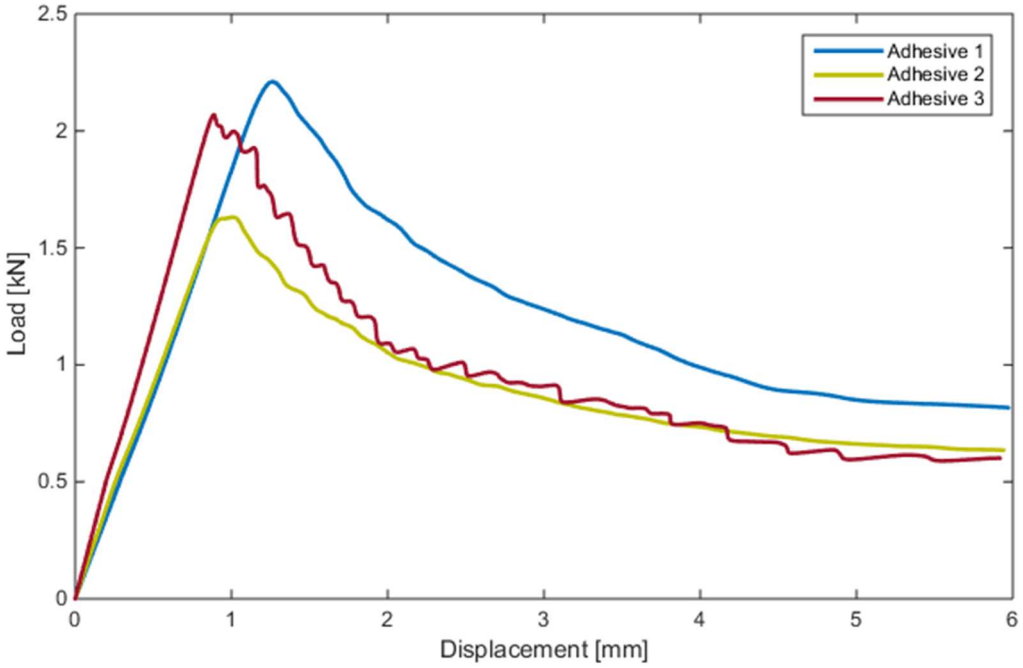

Figure 4.2 – Representative load-displacement curves for a DCB test of each adhesive.

All the specimens presented cohesive failure surfaces (Figure 4.3).

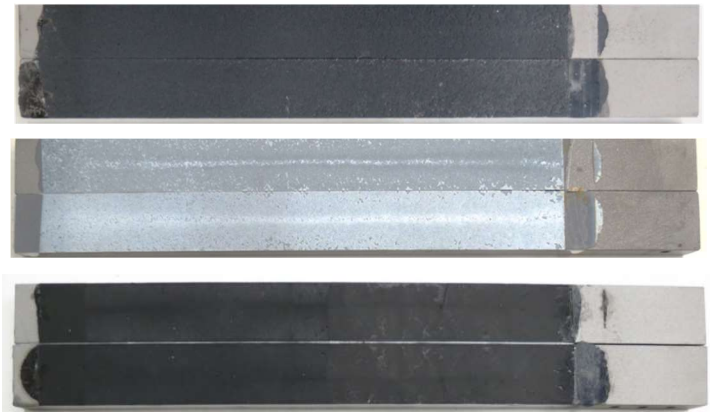

Figure 4.3 – Failure surfaces of DCB specimens. From the top to the bottom: Adhesive 1, Adhesive 2 and Adhesive 3.

The critical energy release rate was evaluated using the CBBM methodology. The values of G in the R-curves initially increase with the equivalent crack length until reaching a plateau, corresponding to G_{Ic} (Figure 4.4).

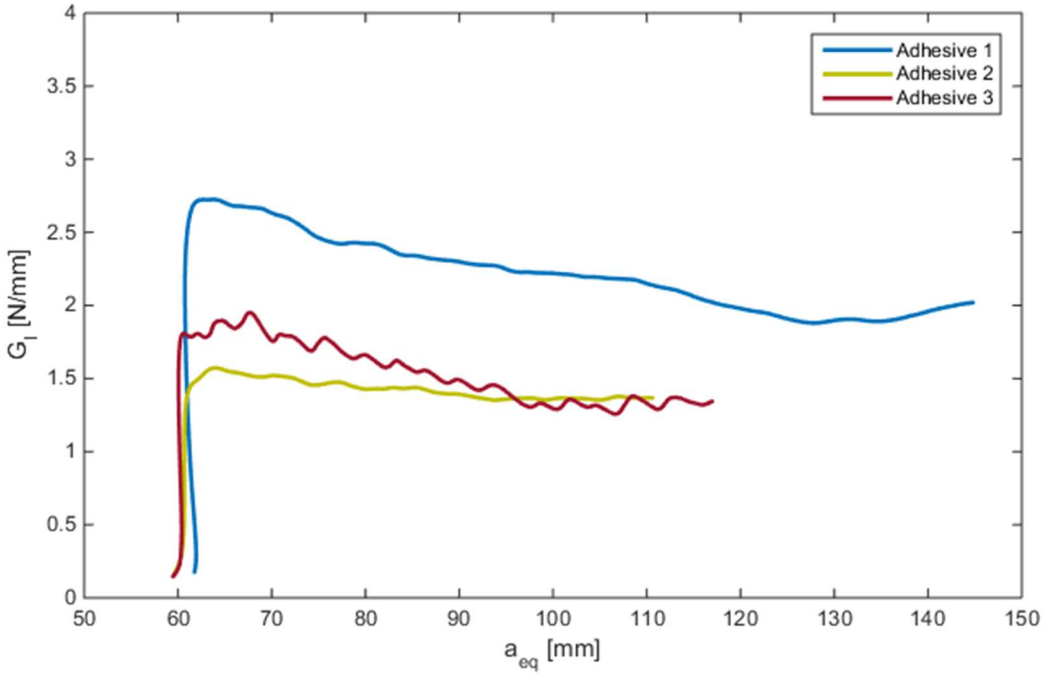

Figure 4.4 – Representative R-curves for a DCB test of each adhesive.

Table 4.2 collects the average values of the fracture toughness of each adhesive. Adhesive 1 presents the highest value of the three and adhesives 2 and 3 are approximately similar in terms of G_{Ic}.

Table 4.2 - Fracture energies for the DCB tests.

Adhesive	G_{Ic} [N/mm]
1	2.06 ± 0.23
2	1.57 ± 0.21
3	1.51 ± 0.26

4.2.2 Mode II

ENF tests were done to determine the fracture energy in mode II. Figure 4.5 shows representative load-displacement curves obtained from these tests. It is possible to observe that the critical loads of the three adhesives are approximately equivalent. However, the curve of Adhesive 3 is quite different from the other two, presenting an almost linear behaviour followed by a sharp decline that corresponds to an unstable crack propagation. The $P-\delta$ curves of adhesives 1 and 2, initially increase linearly and then have a smooth transition, leading to a more stable crack propagation.

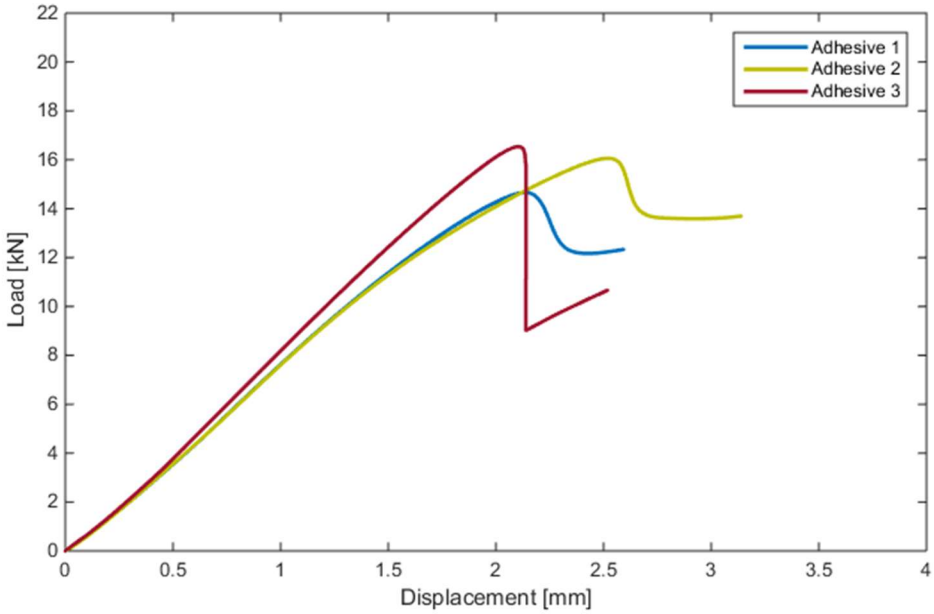

Figure 4.5 – Representative load-displacement curves for a ENF test of each adhesive.

As well as for DCB specimens, the failure surfaces resulting from the ENF tests were all cohesive. Representative failure surfaces of each adhesive are presented in Figure 4.6.

Figure 4.6 – Failure surfaces of ENF specimens. From the top to the bottom: Adhesive 1, Adhesive 2 and Adhesive 3.

Figure 4.7 shows the R-curves experimentally obtained applying the CBBM. The R-curves obtained in the ENF experiments present an increase with the crack length growth, and then a tendency to stabilize, visible by an inflection of the curve. The G_{IIc} is considered to be the G corresponding to the inflection point of the curve. As it was seen in the $P-\delta$ curve of Adhesive 3, the corresponding R-curve shows an abrupt transition from the point of inflection to the point immediately after, which corresponds to a much higher crack length. This results indicate that there is a sudden crack propagation within the joint, pointing to a more brittle adhesive.

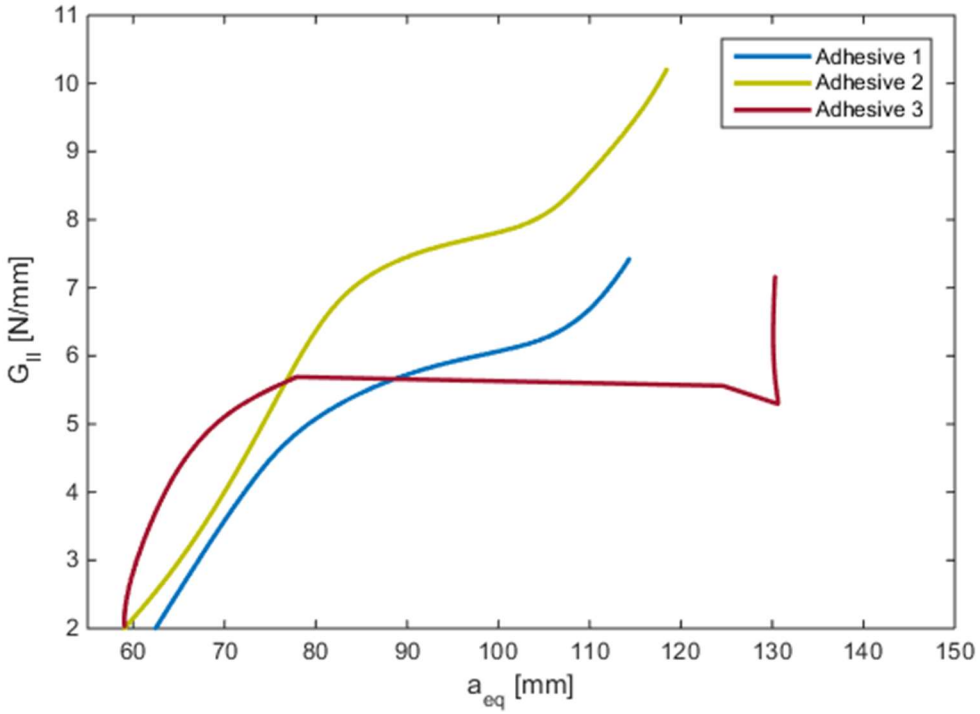

Figure 4.7 – Representative R-curves for a ENF test of each adhesive.

The mean values of G_{IIc} obtained from the several experiments are resumed in Table 4.3. Adhesive 2 shows the higher fracture energy in this case and adhesives 1 and 3 present a slightly lower resistance to shear loads according to this results.

Table 4.3 – Fracture energies for the ENF tests.

Adhesive	G_{IIc} [N/mm]
1	6.20 ± 0.26
2	7.52 ± 0.41
3	6.39 ± 0.40

4.2.3 Mixed-mode I+II

Using an in-house developed mixed-mode apparatus, the fracture behaviour for different combinations of mode I and mode II loading was determined for the studied adhesives.

The procedure followed to assess the fracture behaviour of the different mixed-mode angles tested will be explained using an arbitrary angle.

As the experiments proceed, the load and displacement applied to the specimen were recorded. Figure 4.8 represents $P - \delta$ curves obtained from the universal loading machine. The linear shape in the initial part corresponds to the storage of elastic energy that occurs until the failure load value is achieved, leading to crack initiation. After the peak values the decrease of load is intended as a result of the crack propagation.

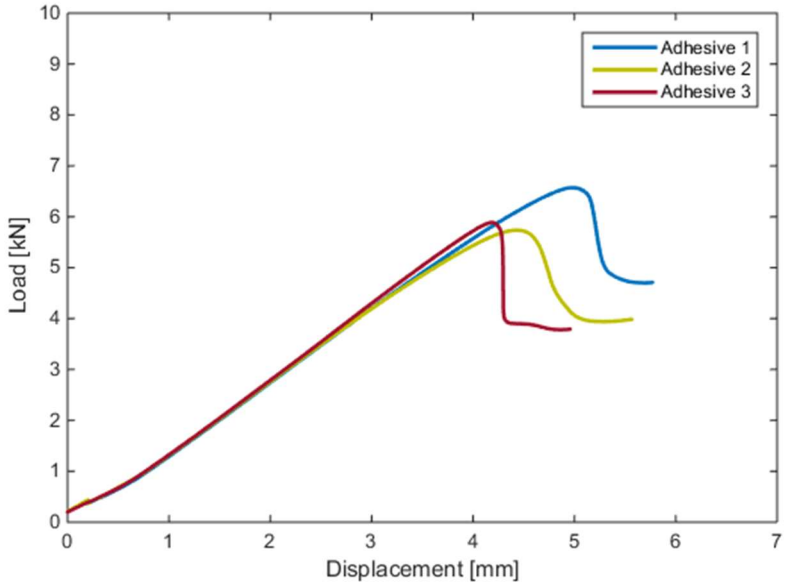

Figure 4.8 – Representative load-displacement curves of each adhesive for an arbitrary angle.

Cohesive failure was verified for all the specimens tested (Figure 4.9).

Figure 4.9 – Failure surfaces of mixed-mode tested specimens. From the top to the bottom: Adhesive 1, Adhesive 2 and Adhesive 3.

To obtain the mode I and mode II components of the energy release rates CBBM methodology was used. When evaluating this equivalent crack, the displacement of the two adherends (δ_1 and δ_2) was measured by LVDT's. The recorded curves of load, δ_1 and δ_2, are represented in Figure 4.10.

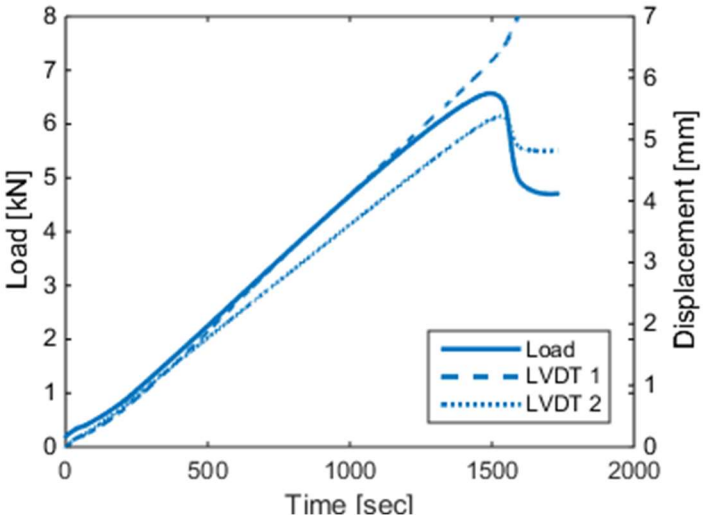

Figure 4.10 – Representative load time curves and LVDT displacements for an arbitrary angle tested.

Figure 4.10 gives a better idea of the variables considered in these tests. LVDT 1 and LVDT 2 measure the displacement of the top and bottom adherend, respectively. In a pure mode test, δ_1 and δ_2 are supposed to be symmetrical. However, in mixed-mode conditions, some contribution of shear loads influence this symmetry, leading to different measured displacements.

Those displacements of the LVDT's, along with the values registered by the loading machine allow to subdivide the mode I and mode II components of the load and displacement applied to the specimen: $P_I - \delta_I$ (mode I) and $P_{II} - \delta_{II}$ (mode II). Figure 4.11 shows representative curves of the two load and displacement components.

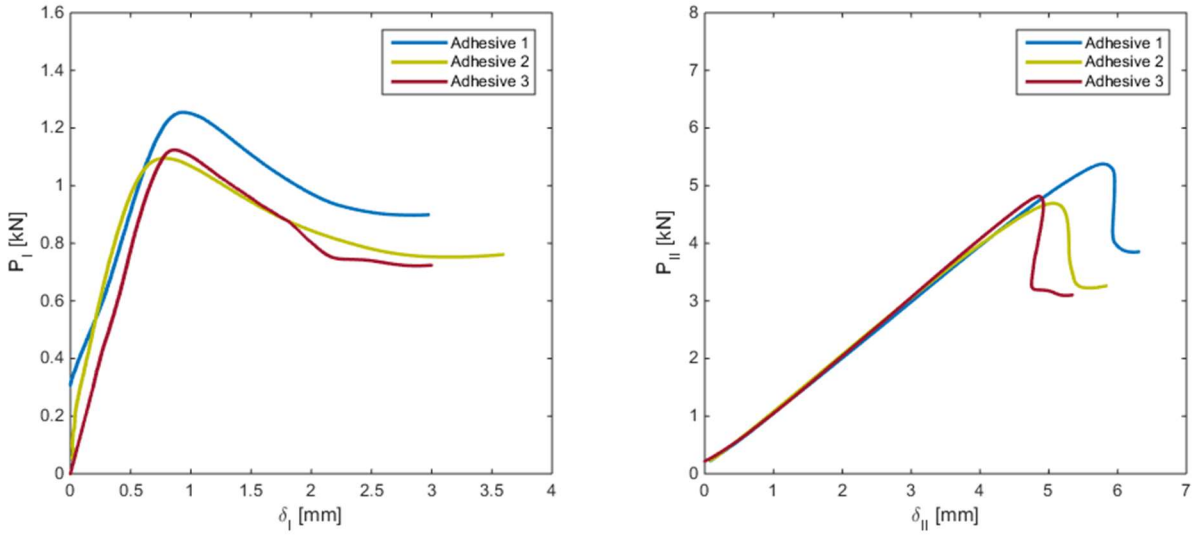

Figure 4.11 – Representative load-displacement mode I component (left) and mode II component (right) for an arbitrary angle tested.

Finally, the R-curves for each component of the load are obtained using the crack equivalent concept (CBBM). Figure 4.12 shows the evolution of G_I and G_{II} with the equivalent crack length in mode I, a_{eq_I} ,and in mode II, $a_{eq_{II}}$, respectively. Through these curves the fracture energies of each mode can be defined.

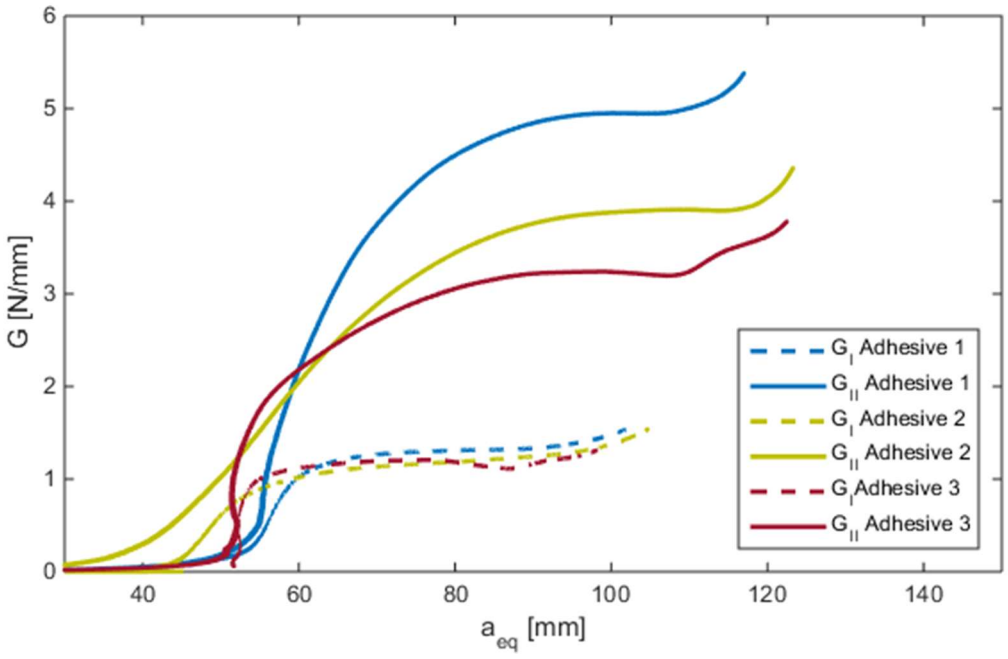

Figure 4.12 – Representative R-curves for an arbitrary angle tested.

4.2.3.1 φ=0°

This mixed-mode apparatus can measure the fracture energy in pure mode I using the specifications presented in Figure 4.13.

s_1 [mm]	s_2 [mm]	s_3 [mm]	s_4 [mm]	L_1 [mm]	$2L$ [mm]
60	100	160	-100	205	230

(a)

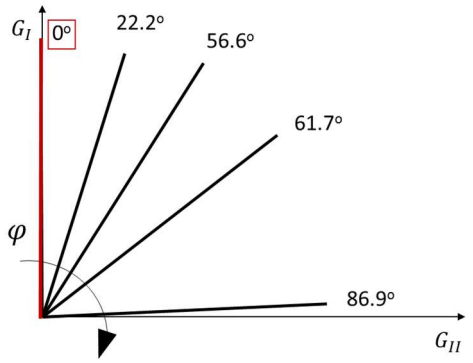

(b)

Figure 4.13 – Experimental specifications for pure mode I using the mixed-mode apparatus: (a) apparatus configuration; (b) mixed-mode angle in the fracture envelope.

For this mixed-mode angle only adhesives 2 and 3 were tested. The R-curves obtained using the CBBM methodology are presented in Figure 4.14.

The mode II component of the R-curves does not appear in these curves, therefore, its presence is negligible, as expected.

The shifted curve of Adhesive 3 in mode I can be explained by the pre-crack length which in this case had a significantly higher value ($a_0 = 130$ mm) than the usual (around 50 mm).

There is an initial increase of the energy release rate with the equivalent crack length until a certain value of G, at which the curve stabilizes. This plateau value corresponds to the fracture energy.

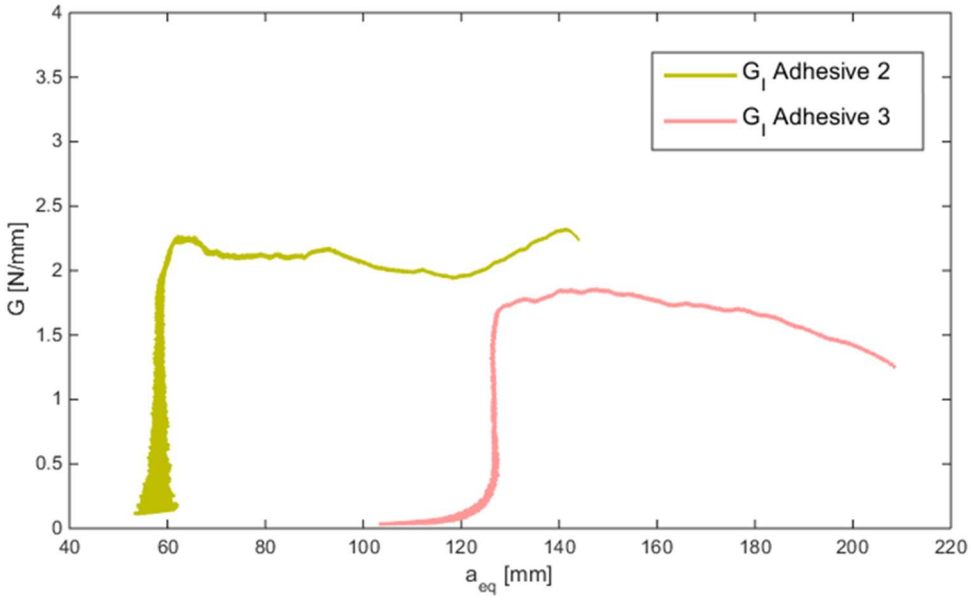

Figure 4.14 – Representative R-curves for mode I tests (φ=0º) of adhesives 2 and 3.

Table 4.4 resumes the results obtained for these tests. Comparing the results of the DCB tests to the results obtained using the mixed-mode apparatus it can be verified that the fracture energy in mode I changes significantly for Adhesive 2. The value obtained with the DCB tests was lower ($G_{Ic} = 1.57$ N/mm). Regarding the Adhesive 3 just a slight difference between values was verified (for DCB $G_{Ic} = 1.51$ N/mm). This difference may be explained by the stiffness of the apparatus, that was not considered for the calculations. The more ductile behaviour of Adhesive 2 can explain this fact. When a ductile adhesive is used, higher deformation will occur until final rupture, and so, the stiffness of the components will have more influence.

The effective mixed-mode angle is in good agreement with the angle defined by the apparatus.

Table 4.4 – Fracture energies for the mixed-mode angle of 0.0º.

$\varphi_{apparatus}$ [º]	Adhesive	G_I [N/mm]	G_{II} [N/mm]	$\varphi_{effective}$ [º]
0.0	2	1.95 ± 0.22	–	0.0
	3	1.60 ± 0.28	–	0.0

4.2.3.2 φ=22.2º

A mixed-mode angle of 22.2^o should represent a mixed-mode condition close to mode I, with a little presence of mode II load. Figure 4.15 shows the configuration used to perform these tests as well as the location of this angle in the fracture envelope.

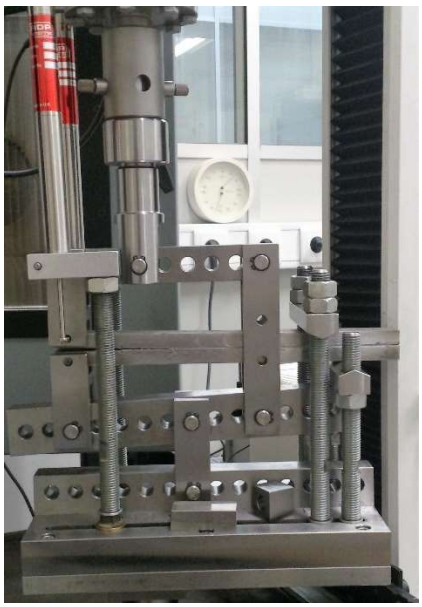

(a)

s_1 [mm]	s_2 [mm]	s_3 [mm]	s_4 [mm]	L_1 [mm]	$2L$ [mm]
60	100	160	-60	205	230

(b)

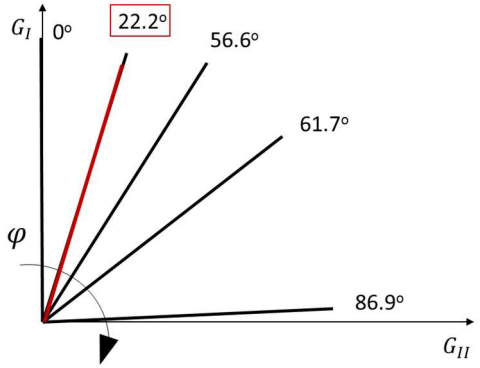

(c)

Figure 4.15 – Experimental specifications for the mixed-mode angle of 22.2º: (a) mixed-mode apparatus; (b) apparatus configuration; (c) mixed-mode angle in the fracture envelope.

The R-curves were obtained using the crack equivalent concept (CBBM). Figure 4.16 represents R-curves for each adhesive resulting from mixed-mode tests performed ($\varphi = 22.2^o$). All the curves have an initial increasing value of G and, at a certain point, a tendency to stabilize. The value of G corresponding to the stabilization of the curve gives the fracture energies in each mode.

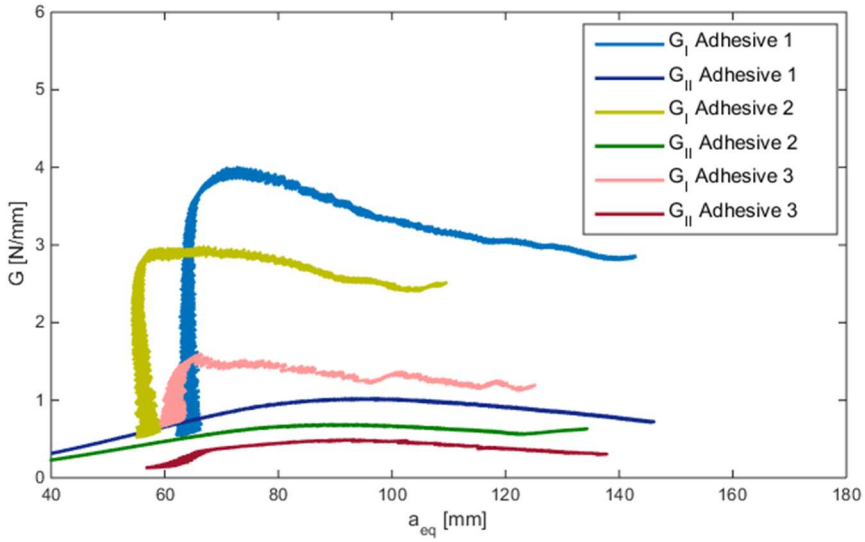

Figure 4.16 – Representative R-curves for a mixed-mode test of each adhesive φ=22.2º.

It is also verified that the fracture energy in mode I for all the adhesives is higher than the fracture energy in mode II. That result was expected due to the proximity of the phase angle to mode I.

Comparing curves of different adhesives, G_I curves seem more distanced, leading to different values of fracture energy. The values of G_{II} appear to be more consistent between adhesives, in this case.

As shown in Table 4.5, Adhesive 1 shows the higher fracture energies in both mode components, while Adhesive 3 shows to be the less resistant to crack propagation.

The effective mixed-mode angle was also evaluated using the G_I and G_{II} obtained (Table 4.5). The effective angles calculated are higher in this case. This means that the apparatus may be applying a load combination slightly different than the supposed, underestimating G_I value or/and overestimating G_{II}.

Table 4.5 – Fracture energies and effective mixed phase angles for the mixed-mode tests (φ=22.2º).

$\varphi_{apparatus}$ [º]	Adhesive	G_I [N/mm]	G_{II} [N/mm]	$\varphi_{effective}$ [º]
22.2	1	2.95 ± 0.09	1.14 ± 0.21	31.8 ± 2.1
	2	2.21 ± 0.31	0.74 ± 0.11	30.1 ± 1.8
	3	1.42 ± 0.33	0.51 ± 0.10	31.0 ± 0.5

4.2.3.3 φ=56.6°

The mixed-mode angle of 56.6^o represents the more balanced mixed-mode test performed in terms of mode I and mode II contribution. This test only comprises adhesive 2 and 3, as referred in section 3.4. Figure 4.17 shows the configuration used to perform these tests as well as the location of this angle results in the fracture envelope.

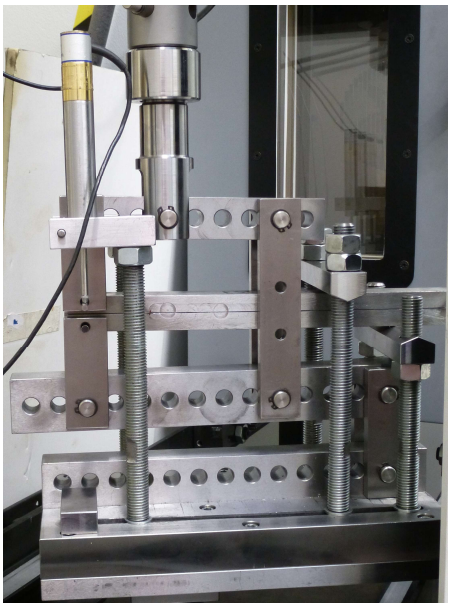

(a)

s_1 [mm]	s_2 [mm]	s_3 [mm]	s_4 [mm]	L_1 [mm]	$2L$ [mm]
60	80	140	80	180	230

(b)

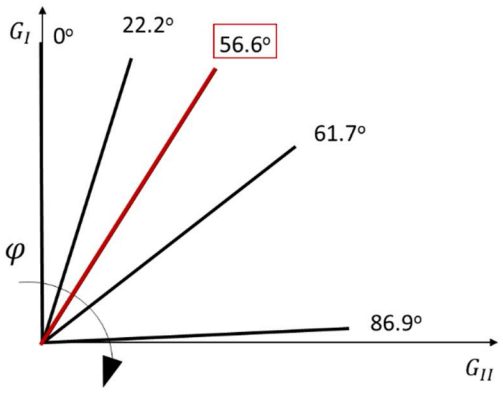

(c)

Figure 4.17 – Experimental specifications for the mixed-mode angle of 56.6º: (a) mixed-mode apparatus; (b) apparatus configuration; (c) mixed-mode angle in the fracture envelope.

The R-curves obtained (Figure 4.18) were evaluated using the crack equivalent concept of the CBBM methodology. The curves present an initial increasing value of G and, at a certain point, a tendency to stabilize. The value of G corresponding to the stabilization of the curve gives the fracture energies in each mode.

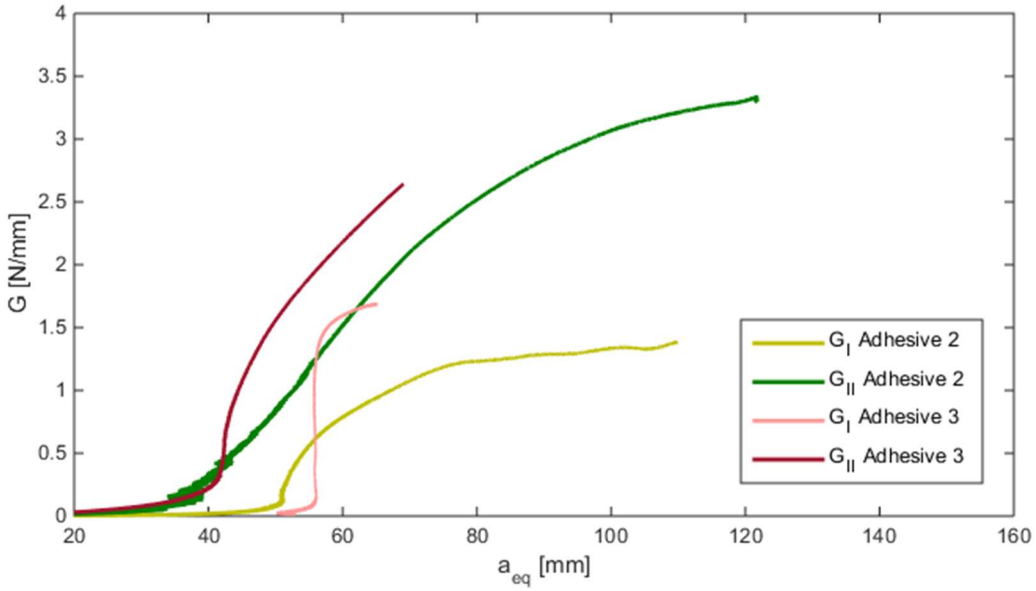

Figure 4.18 – Representative R-curves of a mixed-mode test of adhesives 2 and 3 (φ=56.6º)

It is verified that the fracture energy in mode II is higher than the fracture energy in mode I (a ratio around 1.5 is obtained).

Table 4.6 resumes the average fracture energies obtained.

The effective mixed-mode angle was also evaluated using the values of G_I and G_{II} obtained (Table 4.6). The effective angles calculated are in good agreement with the angle proposed by the apparatus configuration ($\varphi_{apparatus}$).

Table 4.6 – Fracture energies and effective mixed phase angles for the mixed-mode tests (φ=56.6º)

$\varphi_{apparatus}$ [º]	Adhesive	G_I [N/mm]	G_{II} [N/mm]	$\varphi_{effective}$ [º]
56.6	2	1.45 ± 0.07	3.43 ± 0.11	56.93 ± 0.2
	3	1.32 ± 0.25	2.61 ± 0.44	54.59 ± 2.0

4.2.3.4 φ=61.7°

To perform this test, the apparatus was adjusted according to the specifications presented in Figure 4.19. The mixed-mode angle of 61.7^o represents a combined effect of mode I and mode II applied to the specimen. In this case there is a significant contribution of both modes.

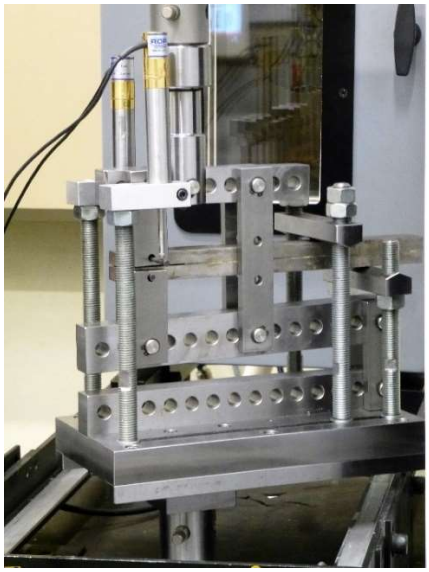

(a)

s_1 [mm]	s_2 [mm]	s_3 [mm]	s_4 [mm]	L_1 [mm]	$2L$ [mm]
40	60	100	120	165	220

(b)

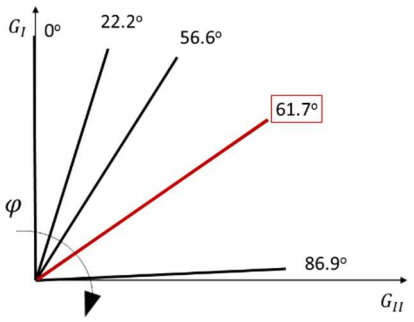

(c)

Figure 4.19 – Experimental specifications for the mixed-mode angle of 61.7º: (a) mixed-mode apparatus; (b) apparatus configuration; (c) mixed-mode angle in the fracture envelope.

Figure 4.20 represents typical R-curves for each adhesive resulting from these mixed-mode tests performed ($\varphi = 61.7^o$). The value of G corresponding to the verified plateau gives the fracture energies in each mode.

Moreover, it is verified that the fracture energy in mode II for all the adhesives is significantly higher than the fracture energy in mode I (a ratio between 3 and 5 is obtained). Comparing different adhesives, the plateaus of G_{II} curves are more distant than the plateaus of G_I curves.

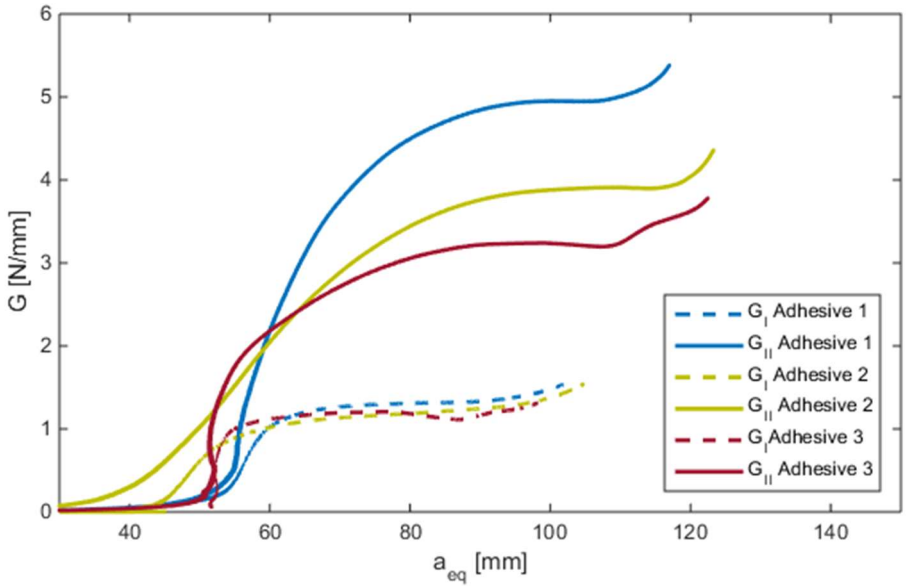

Figure 4.20 – Representative R-curves for a mixed-mode test of each adhesive (φ =61.7º)

Table 4.7 resumes the average fracture energies obtained for all the experiments. Adhesive 1 shows the higher energy release rate in mode II while adhesives 2 and 3 show to be less resistant to the shear load.

The effective mixed-mode angle was also evaluated using the values of G_I and G_{II} obtained (Table 4.7). The effective angles calculated are in good agreement with the angle proposed by the apparatus configuration ($\varphi_{apparatus}$).

Table 4.7 – Fracture energies and effective mixed phase angles for the mixed-mode tests (φ=61.7º)

$\varphi_{apparatus}$ [º]	Adhesive	G_I [N/mm]	G_{II} [N/mm]	$\varphi_{effective}$ [º]
61.7	1	1.29 ± 0.28	4.59 ± 0.49	62.2 ± 1.7
	2	1.22 ± 0.08	4.10 ± 0.63	61.3 ± 1.3
	3	1.25 ± 0.17	3.32 ± 0.22	58.5 ± 0.9

4.2.3.5 φ=86.9°

The mixed-mode angle of 86.9^o represents the closest to mode II mixed-mode test performed. This angle intends to obtain an almost pure mode II loading. Figure 4.21 shows the configuration used to perform these tests as well as the location of this angle in the fracture envelope.

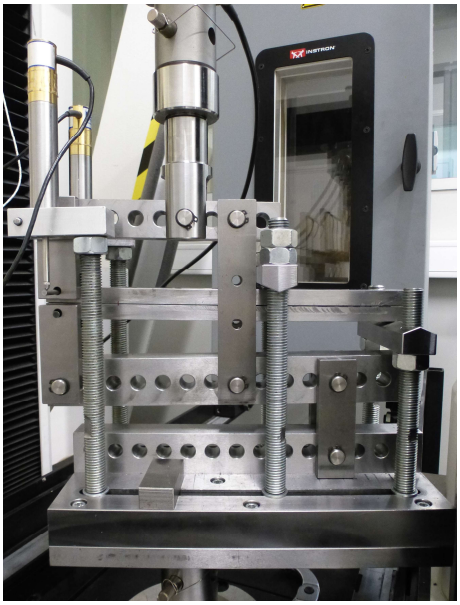

(a)

s_1 [mm]	s_2 [mm]	s_3 [mm]	s_4 [mm]	L_1 [mm]	$2L$ [mm]
100	40	140	80	170	270

(b)

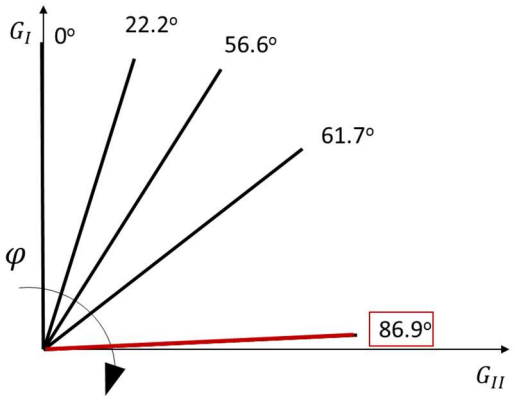

(c)

Figure 4.21 – Experimental specifications of the mixed-mode angle of 86.9º: (a) mixed-mode apparatus; (b) apparatus configuration; (c) mixed-mode angle in the fracture envelope.

Figure 4.22 shows the R-curves obtained using the CBBM methodology. It can be seen that the R-curves of the mode I component are negligible comparing to the mode II R-curves. That indicates the efficiency of the apparatus to perform the loading required.

Analyzing mode II R-curves there is an initial increase of the energy release rate with the equivalent crack length until a certain value of G, at which the curve stabilizes. The G corresponding to the point of inflection is considered to be the value of the fracture energy.

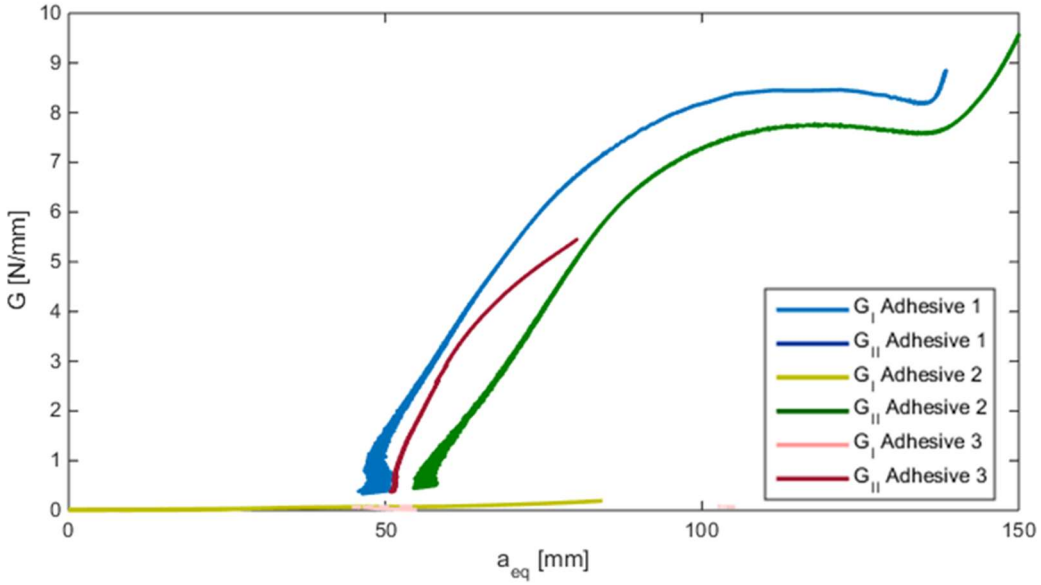

Figure 4.22 – Representative R-curves of a mixed-mode test (φ=86.9º) of each adhesive.

The average results of this tests are shown in Table 4.8. Comparing the results of the ENF tests (Table 4.3) to the results obtained using the mixed-mode apparatus, it can be verified that the fracture energies in mode II are approximately the same. The difference between values can be explained either by some friction of ENF tests and by the stiffness of the machine that is not considered. Friction leads to higher G_{IIc} of the ENF tests (as the case of adhesives 2 and 3) and the stiffness of the machine also leads to higher fracture energies (Adhesive 1).

The effective mixed-mode angle was determined using the values of G_I and G_{II} obtained (Table 4.8). The angles calculated are in good agreement with the angle proposed by the apparatus configuration ($\varphi_{apparatus}$).

Table 4.8 – Fracture energies and effective mixed phase angles for the mixed-mode tests (φ=86.9º).

$\varphi_{apparatus}$ [º]	Adhesive	G_I [N/mm]	G_{II} [N/mm]	$\varphi_{effective}$ [º]
86.9	1	0.03 ± 0.01	7.55 ± 0.77	86.7 ± 0.3
	2	0.03 ± 0.01	7.06 ± 0.80	86.6 ± 0.2
	3	0.02 ± 0.01	5.53 ± 0.8	86.9 ± 0.6

4.2.4 Fracture envelope

The fracture energies determined by pure mode tests along with the energy release rates determined by mixed-mode tests allowed to build fracture envelopes of the three adhesives. Fracture envelopes are good representatives of the fracture behaviour since the global tendency of the fracture toughness can be easily assessed using the trend line defined by the determined points.

Using the fracture energy data calculated with the previously described tests, fracture envelopes were produced, one for each of the adhesives tested. Those fracture envelopes are presented in Figure 4.23.

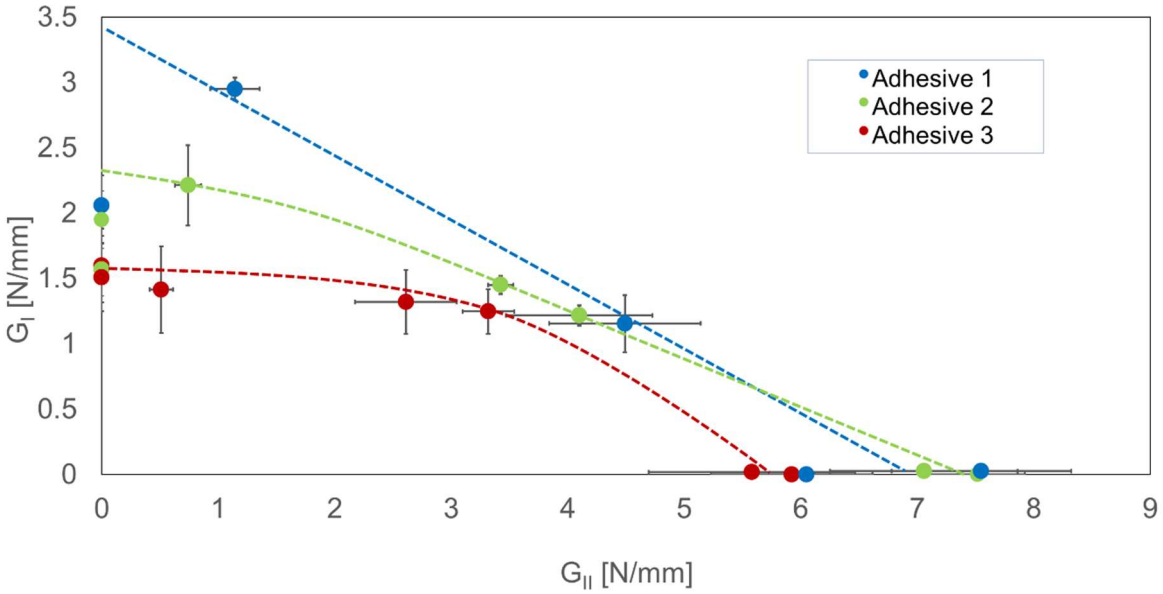

Figure 4.23 – Fracture envelopes obtained for the three adhesives.

Fracture energies in mode II are higher than in mode I, as expected. The differences between the fracture energies verified in pure modes obtained using the apparatus and the standard tests can be explained due to the stiffness of the apparatus, which was not considered in the calculations.

The envelopes clearly show that Adhesive 1 is the toughest adhesive, with significantly higher fracture energies measured for all the cases under study. Adhesive 3 is the less tough, while Adhesive 2 has fracture energy values between those exhibited by the other two adhesives.

The ductility of the adhesive may have an influence on the energetic criterion of the fracture envelope. Adhesive 1 appears to follow a linear criterion while adhesives 2 and 3 show more agreement with a quadratic criterion. A similar mixed-mode linear criterion for a ductile adhesive was obtained by Chaves et al. (2014) studying Araldite® 2015.

In the fracture envelopes of adhesives 1 and 2, high values of G_I were obtained for the mixed-mode angle close to mode I. This same tendency was found by Stamoulis et al. (2014) while studying the mixed-mode fracture behaviour of a ductile adhesive (SikaPower®-498). The increase of the G_I value near mode I may be due the plasticization of the adhesive.

4.3 Fatigue

The main purpose of the fatigue tests was the assessment of the Fatigue Crack Curves to define the Paris law parameters in each type of loading.

The FCG curves were obtained considering the crack equivalent concept (CBBM), thus avoiding the measurement of the real crack length. The equivalent crack length represented in Figure 4.24 shows an example of the evolution of the crack propagation until final rupture.

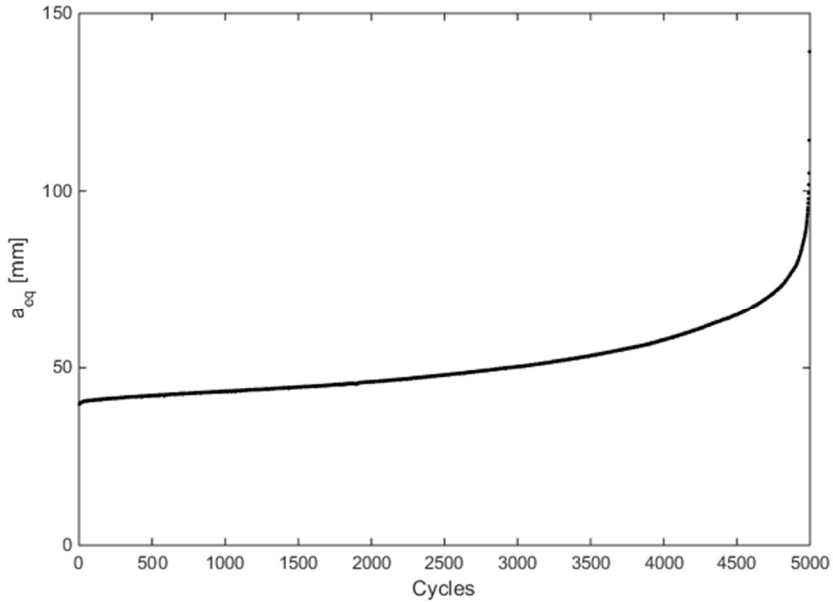

Figure 4.24 – Representative curve of the equivalent crack length evolution as a function of the number of cycles.

The evolution of G_{max} as a function of the crack length is represented in Figure 4.25. It is verified that the plotted value tends to the fracture energies determined statically. In the final rupture these values are the same.

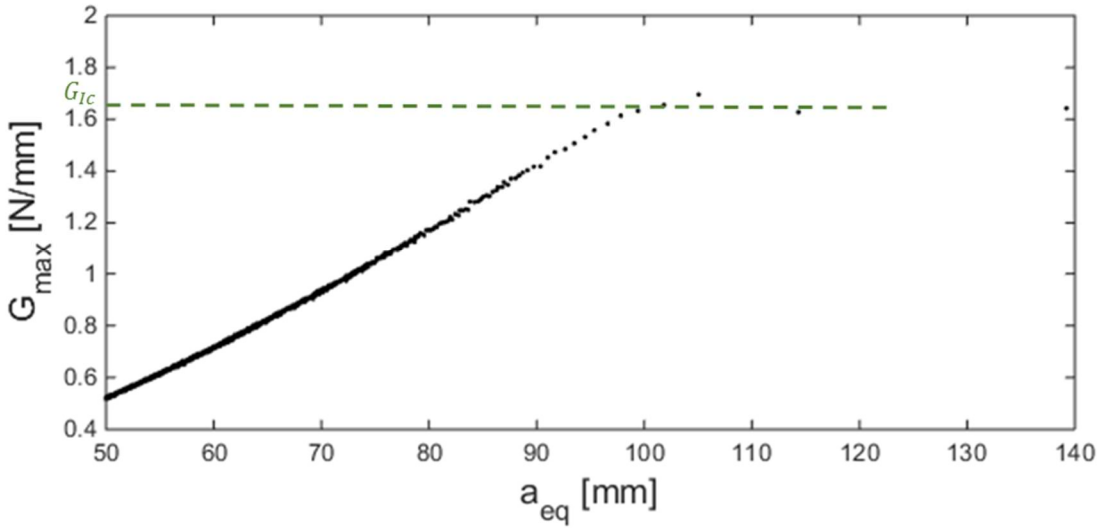

Figure 4.25 – Representative curve of the equivalent crack length evolution as a function of the number of cycles.

4.3.1 Mode I

Applying to the specimens cyclic opening loads as DCB test for static conditions it was possible to analyze the crack propagation rate by recording the load and displacement during the test.

Table 4.9 shows in detail the parameters applied to the specimens during the experiments. The ratio of the failure load used for adhesive 2 characterizations was exceptionally higher in these tests due to difficulties inherent to the onset crack when using the usual 70% value.

Table 4.9 – Fatigue parameters used to perform the fatigue tests in mode I.

Adhesive	Frequency [Hz]	Failure load [N]	P_{max} [N]	P_{min} [N]	No. of specimens
2	1	2350	1900*	190	4
3	1	2000	1400	140	3

*80% of the failure load was considered in this case

The tested specimens presented cohesive failure, as represented in Figure 4.26.

Figure 4.26 – Failure surfaces of mode I specimens tested in fatigue. Adhesive 2 (top) and Adhesive 3 (bottom).

Two examples of FCG curves obtained are represented in Figure 4.27 and Figure 4.28 for Adhesive 2 and Adhesive 3, respectively.

Observing these curves, a well-defined linear shape is verified. The linear stage, where the propagation takes place, fits well with the Paris law relationship, as referred in section 2.6.2. Therefore, the Paris law parameters were determined by equations of the trend lines.

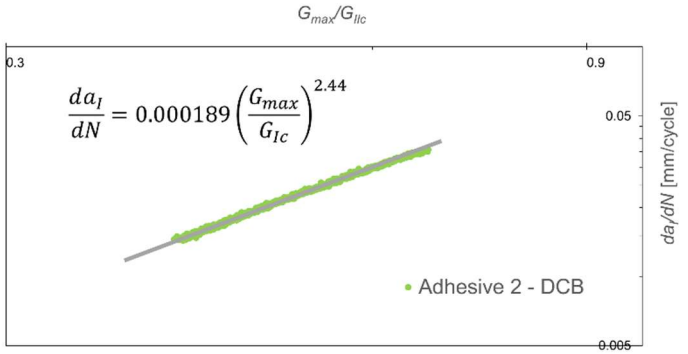

Figure 4.27 – Representative FCG curve for Adhesive 2 in mode I.

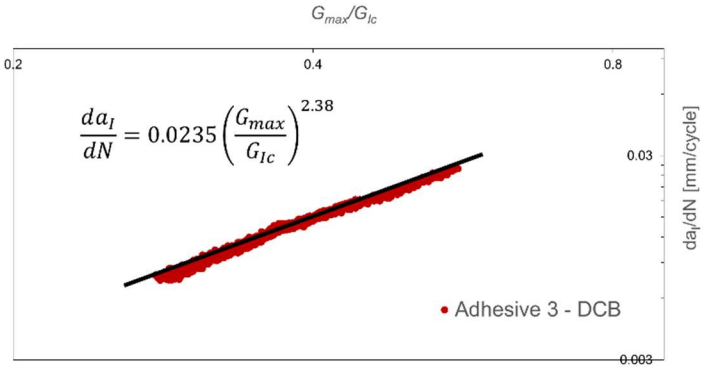

Figure 4.28 – Representative FCG curve for Adhesive 3 in mode I.

The Paris law parameters obtained from all the considered DCB specimens are presented in Table 4.10.

Table 4.10 – Paris law constants of DCB specimens.

Adhesive	Specimen	m_I	C_I
2	1	2.44	0.0002
	2	2.44	0.0923
	3	2.40	0.0167
	4	2.41	0.0798
	Average	2.42 ± 0.02	0.0472 ± 0.0395
3	1	2.97	0.1270
	2	3.11	0.0121
	3	2.38	0.0235
	Average	2.82 ± 0.32	0.0542 ± 0.0517

It can be said that in mode I both adhesives have similar resistance to crack propagation, comparing the Paris law slopes. The results of m present a good agreement while the intersections, C, present some scatter. This fact can be explained by the dependency of C on the damage initiation instant, influenced by the pre-crack (Fernández 2008). Nonetheless, the impact of this parameter in propagation rate is small when compared to m.

4.3.2 Mode II

In order to analyze the crack propagation rate a cyclical shear loading was applied to the specimens and so load and displacement were recorded.

ENF tests were done considering the specifications of Table 4.11. The fraction of the failure load used was 70% for the two adhesives.

Table 4.11 – Fatigue parameters used to perform the fatigue tests in mode II.

Adhesive	Frequency [Hz]	Failure load [N]	P_{max} [N]	P_{min} [N]	No. of specimens
2	2	15000	10500	1050	3
3	2	20000	14000	1400	3

As the measurement of the crack length is difficult and inaccurate, the equivalent crack length concept of CBBM was also applied in these data analysis.

Cohesive failure was verified in all the specimens (Figure 4.29).

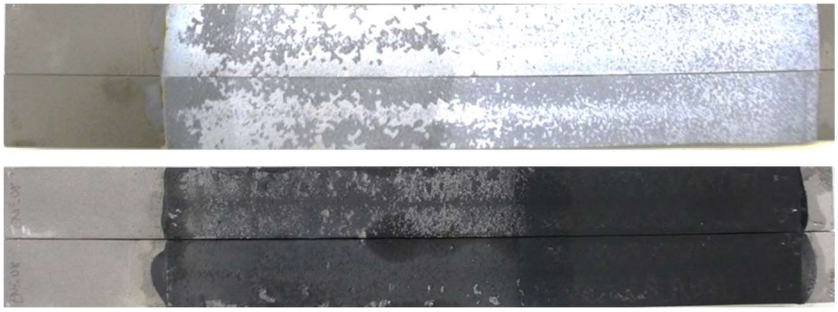

Figure 4.29 – Failure surfaces of mode I specimens tested in fatigue. Adhesive 2 (top) and Adhesive 3 (bottom).

Figure 4.30 and Figure 4.31 shows FCG curves obtained in mode I. Power laws were fitted to establish the corresponding parameters.

It can be immediately concluded that the slope is lower in mode II compared to mode I, for both adhesives, indicating that shear loads lead to slower crack propagation.

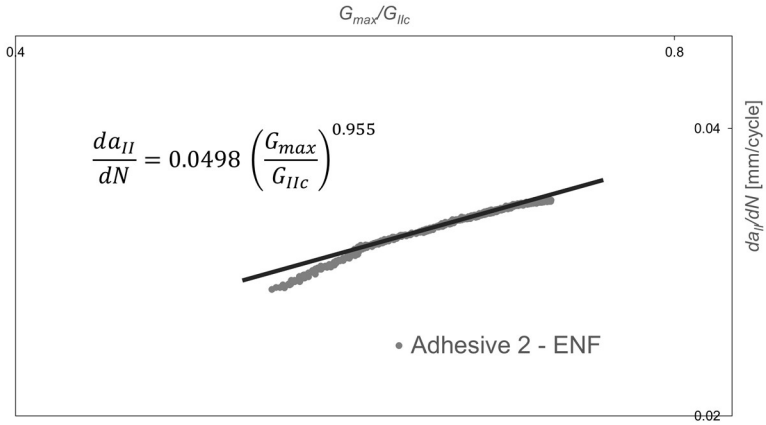

Figure 4.30 – Representative FCG curve for Adhesive 2 in mode II.

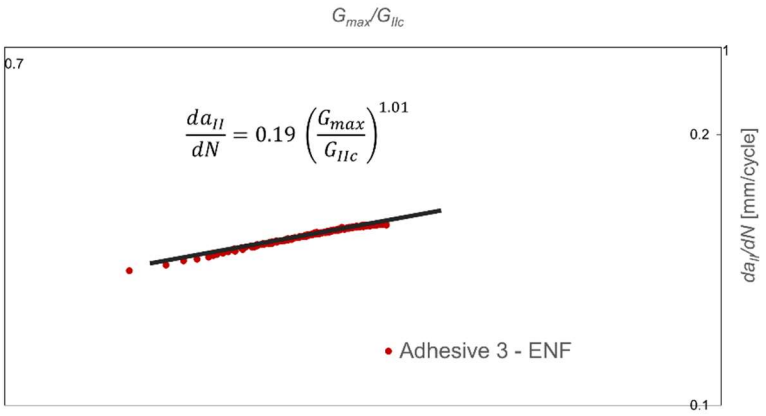

Figure 4.31 – Representative FCG curve for Adhesive 3 in mode II.

Table 4.12 resumes the Paris law parameters determined. Once again, it was verified that the slope values were in good agreement but the intersections had a large scatter.

Table 4.12 – Paris law constants of ENF specimens.

Adhesive	Specimen	m_{II}	C_{II}
2	1	1.15	0.8570
	2	1.00	0.0860
	3	0.96	0.0498
	Average	1.03 ± 0.08	0.3309 ± 0.3723
3	1	1.06	0.2690
	2	1.01	0.1900
	3	0.98	0.0821
	Average	1.02 ± 0.03	0.1804 ± 0.0766

4.3.3 Mixed-mode I+II

The mixed-mode analysis in fatigue was done using the same apparatus used in static tests. The study included configurations for three different mixed-mode angles: $\varphi = 22.2^o$, $\varphi = 56.6^o$ and $\varphi = 73.9^o$.

The load P and displacement δ were registered during the tests as well as the displacement of the adherends tips, δ_1 and δ_2, measured by the LVDT's. Knowing δ_1 and δ_2, the two components of load could be separated, obtaining two FCG curves for each test. The equivalent crack length of CBBM methodology was used to determine the FCG curves.

Figure 4.32 shows an example of the displacements recorded during a mixed-mode test in fatigue (maximum and minimum values). The LVDT1 and LVDT2 show different displacements between them, which means that the two adherends do not have a symmetrical movement. The displacements have a slight increase during the experiment until the final rupture occurs, leading to a huge variation.

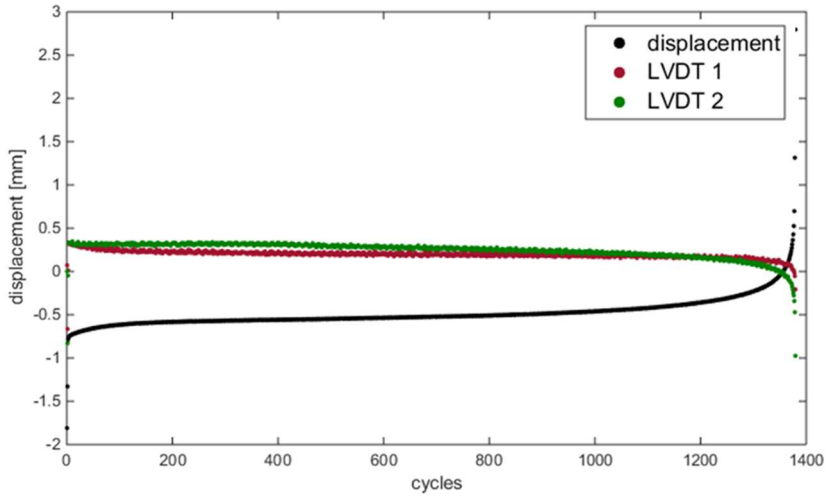

Figure 4.32 – Example of the displacements recorded during a fatigue mixed mode-test.

That procedure was done following the formulation of the mixed-mode apparatus and using CBBM to determine either G_I and G_{II} (Equations 2.29 and 2.30).

The same way as for static conditions the load and displacements were separated to calculate the mode I and mode II components. Examples of these two components are presented in Figure 4.33 and Figure 4.34.

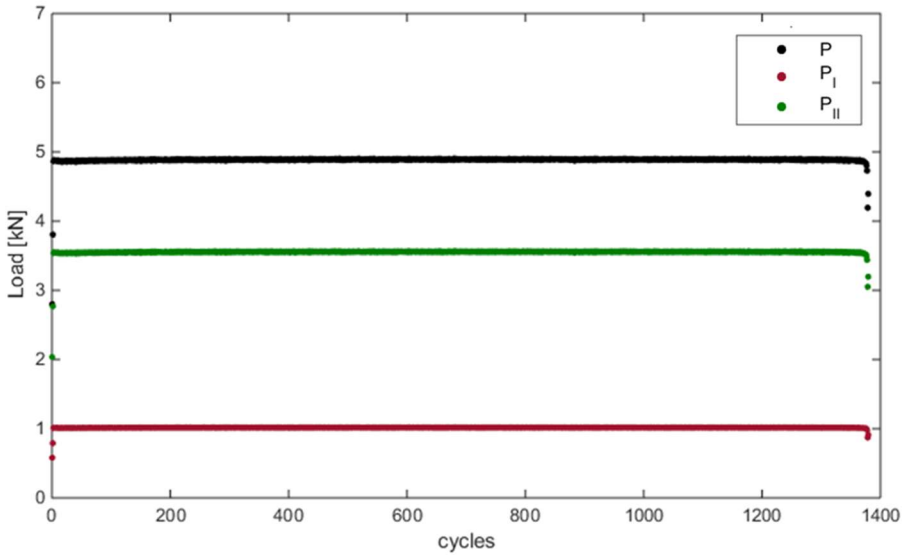

Figure 4.33 – Example of the mode I and mode II components of the load during a fatigue mixed mode-test: load recorded by the loading machine, mode I component and mode II component.

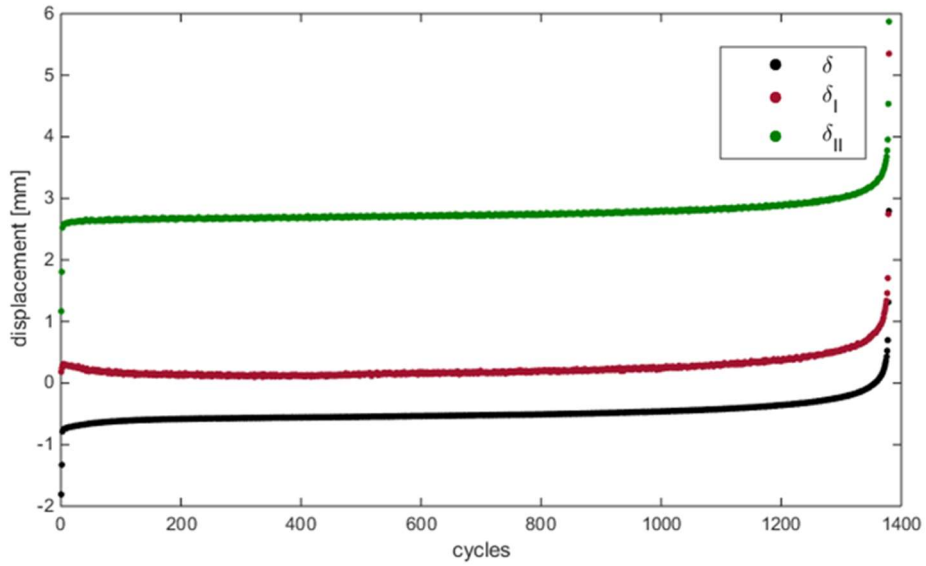

Figure 4.34 – Example of the mode I and mode II components of the displacement during a fatigue mixed mode-test: recorded by the loading machine, mode I component and mode II component.

With the two components calculated, the analysis was done as if mode I and mode II tests have been done. The same procedure used for the pure modes was used to determine the FCG curves.

The fatigue parameters established in each case is resumed in Table 4.13.

Table 4.13 – Experimental parameters used for mixed-mode fatigue tests.

φ [º]	Adhesive	Frequency [Hz]	Failure load [N]	P_{max} [N]	P_{min} [N]	No. of specimens
22.2	2	1	5700	3990	399	4
	3	1	5500	3850	385	3
56.6	2	1	7000	4900	490	3
	3	1	8000	5600	560	3
73.9	2	1	8000	5600	560	3
	3	1	10000	7000	700	3

4.3.3.1 φ=22.2º

The configuration of the apparatus followed to perform these tests is presented in Figure 4.35.

(a)

s_1 [mm]	s_2 [mm]	s_3 [mm]	s_4 [mm]	L_1 [mm]	$2L$ [mm]
60	100	160	-60	205	230

(b)

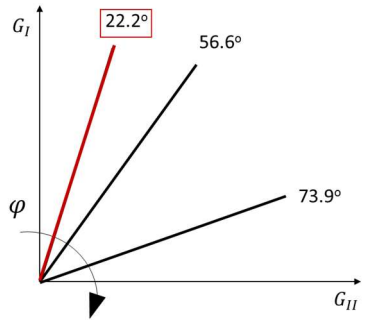

(c)

Figure 4.35 – Experimental specifications for the mixed-mode angle of 22.2º: (a) mixed-mode apparatus; (b) apparatus configuration; (c) mixed-mode angle in the fracture envelope.

As represented in Figure 4.36, the specimens tested had cohesive failure.

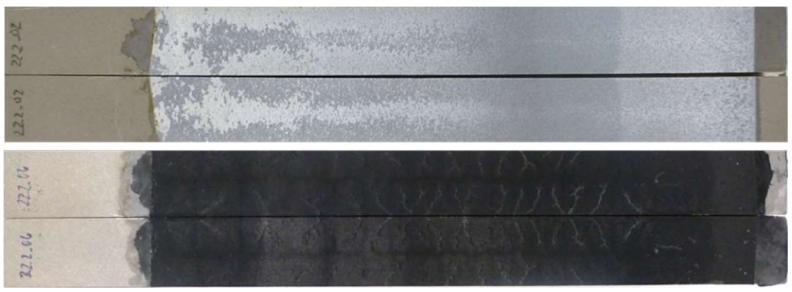

Figure 4.36 – Failure surfaces of mixed-mode specimens tested in fatigue (φ=22.2º). Adhesive 2 (top) and Adhesive 3 (bottom).

The FCG determined in this case showed well-defined curves for the mode I component and very unstable propagation for mode II component. This was an expected result due to the proximity to mode I loading. Representative curves obtained for mode I component are presented in Figure 4.37 and Figure 4.38.

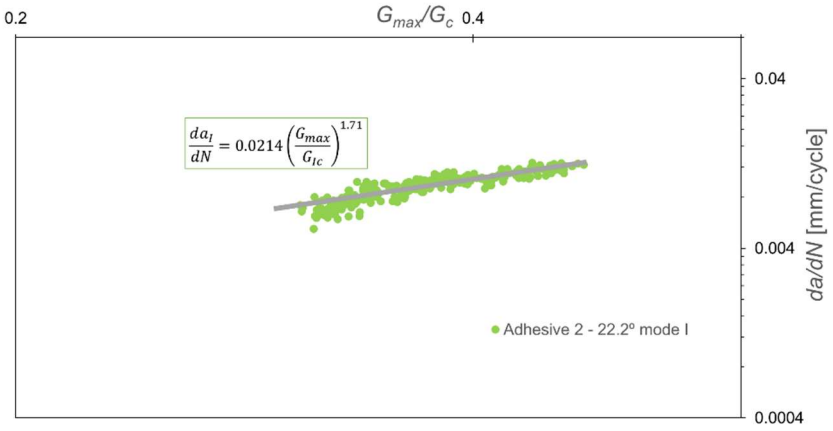

Figure 4.37 – Representative FCG curve for Adhesive 2 in mixed-mode (φ=22.2º).

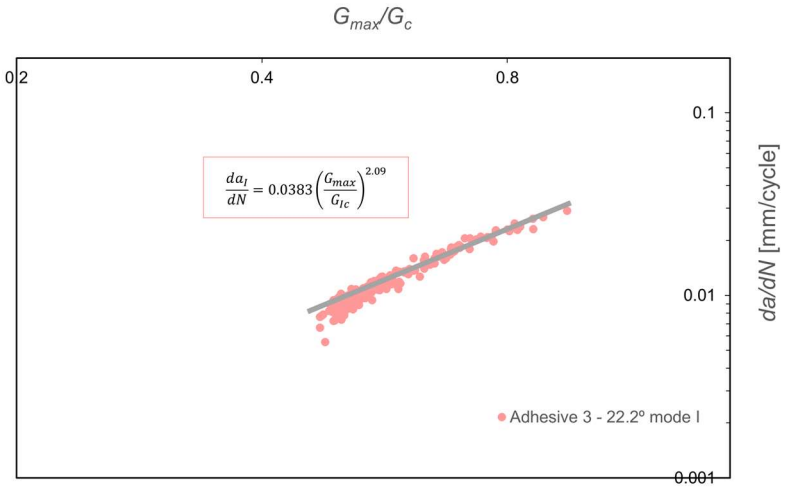

Figure 4.38 – Representative FCG curve for Adhesive 3 in mixed-mode (φ=22.2º).

The mode II FCG curves are not presented due to its irregular shape. Despite that, the correspondent Paris law parameters could be determined.

Additionally, since Adhesive 2 is more ductile, it presented better shaped curves than Adhesive 3. The number of cycles of the experiments using the Adhesive 3 were lower, leading to more scattered curves.

Table 4.14 shows the results of the Paris law parameters obtained.

Table 4.14 – Paris law constants of the mixed-mode specimens tested (φ=22.2º).

Adhesive	Specimen	m_I	C_I	m_{II}	C_{II}
2	1	1.79	0.0383	0.20	0.0039
	2	1.71	0.0214	0.30	0.0048
	3	1.83	0.0226	0.40	0.0046
	4	2.13	0.0166	0.30	0.0017
	Average	1.87 ± 0.16	0.0247 ± 0.0082	0.30 ± 0.07	0.0278 ± 0.0098
3	1	2.02	0.0258	0.30	0.0039
	2	2.41	0.0069	0.20	0.0053
	3	2.09	0.0383	0.20	0.0060
	Average	2.17 ± 0.17	0.0237 ± 0.0129	0.23 ± 0.05	0.0051 ± 0.0009

As seen above, there was a good concordance between all the specimens regarding the Paris law slope of the mode I component. On the other hand, mode II component slope did not present clear results due to the instability of the curves it was based in. The intersections C_1 and C_2 presented scattered values.

4.3.3.2 φ=56.6º

Setup configuration followed to perform these tests is presented in Figure 4.39.

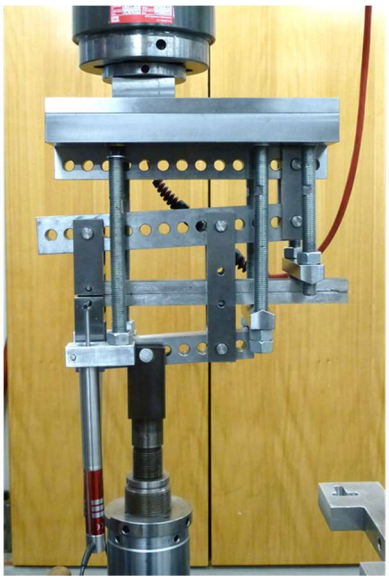

(a)

s_1 [mm]	s_2 [mm]	s_3 [mm]	s_4 [mm]	L_1 [mm]	$2L$ [mm]
60	80	140	80	180	230

(b)

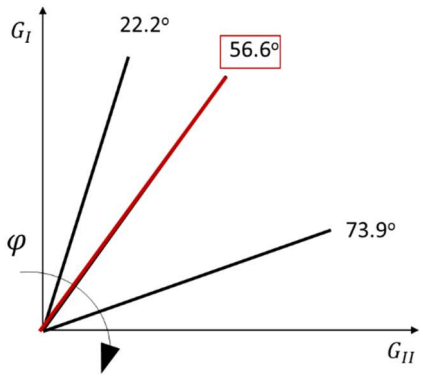

(c)

Figure 4.39 – Experimental specifications for the mixed-mode angle of 56.6º: (a) mixed-mode apparatus; (b) apparatus configuration; (c) mixed-mode angle in the fracture envelope.

All the specimens presented cohesive failure surfaces, as shown in Figure 4.40.

Figure 4.40 – Failure surfaces of mixed-mode specimens tested in fatigue (φ=56.6º). Adhesive 2 (top) and Adhesive 3 (bottom).

FCG curves of each component determined in this case showed a linear shape, used to define the Paris law parameters (Figure 4.41 and Figure 4.42). By observing the curves, it is verified that slope in mode I component is higher than in mode II component, even using a mixed-mode angle with almost the same contribution of mode I and mode II loading.

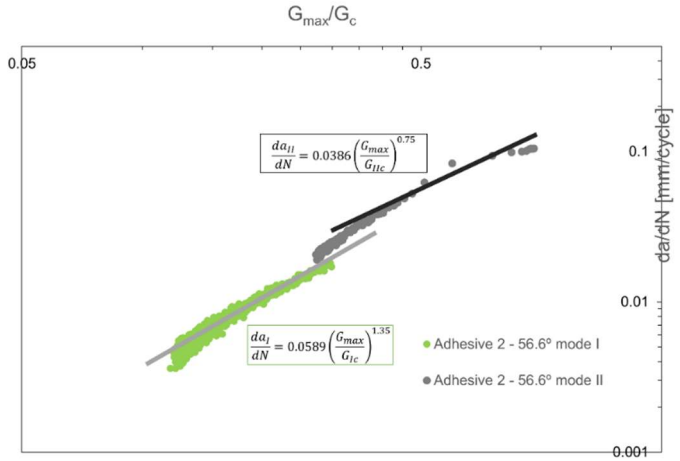

Figure 4.41 – Representative FCG curve for Adhesive 2 in mixed-mode (φ=56.6º).

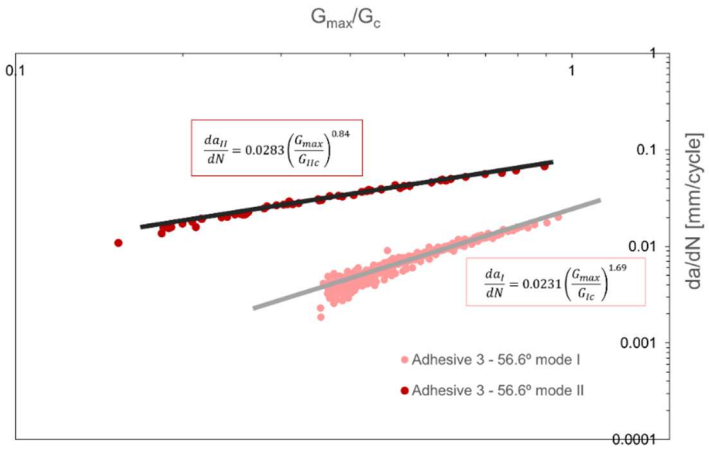

Figure 4.42 – Representative FCG curve for Adhesive 3 in mixed-mode (φ=56.6º).

Table 4.15 shows the results of the Paris law parameters obtained.

Table 4.15 – Paris law constants of the mixed-mode specimens tested (φ=56.6º).

Adhesive	Specimen	m_I	C_I	m_{II}	C_{II}
2	1	1.27	0.0828	0.47	0.1140
	2	1.26	1.1600	0.80	0.0694
	3	1.35	0.0589	0.75	0.0386
	Average	1.29 ± 0.04	0.4339 ± 0.5135	0.67 ± 0.14	0.0740 ± 0.0310
3	1	1.69	0.0231	0.84	0.0283
	2	1.48	0.0213	0.87	0.0800
	3	1.86	0.0099	0.78	0.0311
	Average	1.68 ± 0.16	0.0181 ± 0.0058	0.83 ± 0.04	0.0465 ± 0.0237

The results indicate that Adhesive 2 presents lower slope in both modes, comparing to the same variables obtained for Adhesive 3. This may be intended as an increased susceptibility of brittle adhesives to fatigue loading.

4.3.3.3 φ=73.9°

The same way as for the other angles studied, the configuration of the apparatus was changed, this time to apply a load closer to mode II (Figure 4.43).

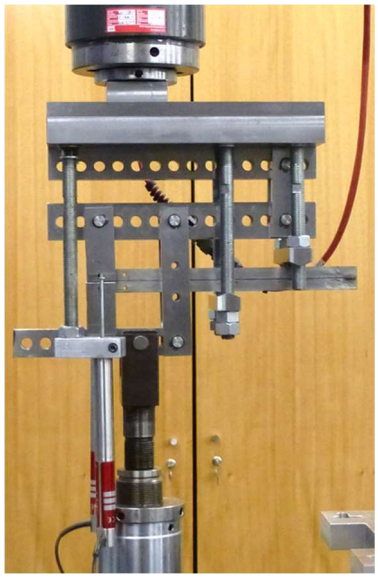

(a)

s_1 [mm]	s_2 [mm]	s_3 [mm]	s_4 [mm]	L_1 [mm]	$2L$ [mm]
40	40	80	120	135	235

(b)

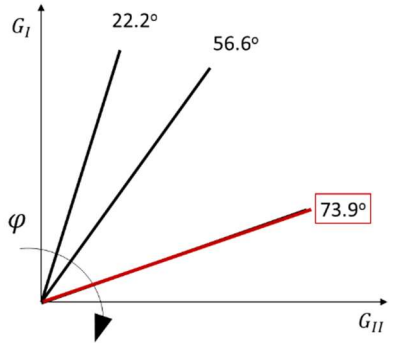

(c)

Figure 4.43 – Experimental specifications for the mixed-mode angle of 73.9: (a) mixed-mode apparatus; (b) apparatus configuration; (c) mixed-mode angle in the fracture envelope.

All the specimens presented cohesive failure, as seen in Figure 4.44.

Figure 4.44 – Failure surfaces of mixed-mode specimens tested in fatigue (φ=73.9º). Adhesive 2 (top) and Adhesive 3 (bottom).

Figure 4.45 and Figure 4.46 shows representative curves of the FCG curves obtained. Well-defined linear shaped curves were verified for Adhesive 2, however in the case of Adhesive 3 the FCG curves were more irregular. In the experiments of Adhesive 2 the FCG rate as a function of G_{max}/G_c increases faster for the mode II component than for mode I, that was expected considering the proximity to mode II loadings. For Adhesive 3, the slope stays higher for mode I than mode II component.

Despite being far from mode I, the major part of these component curves stayed well defined. This indicates that the crack propagation in mode I is more stable.

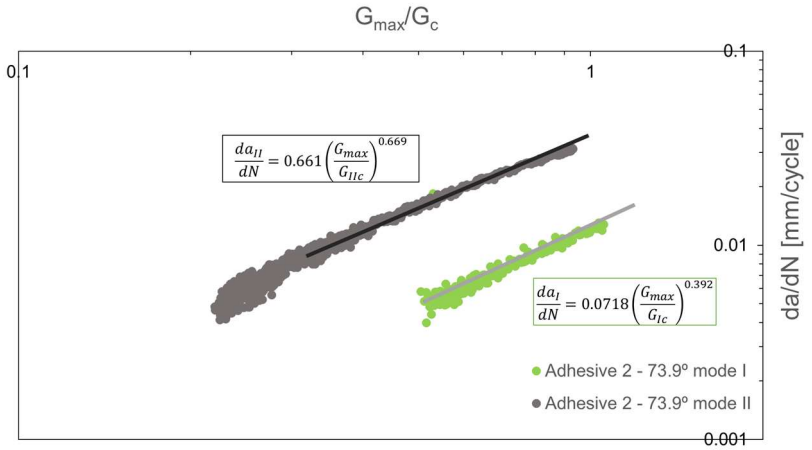

Figure 4.45 – Representative FCG curve for Adhesive 2 in mixed-mode (φ=73.9º).

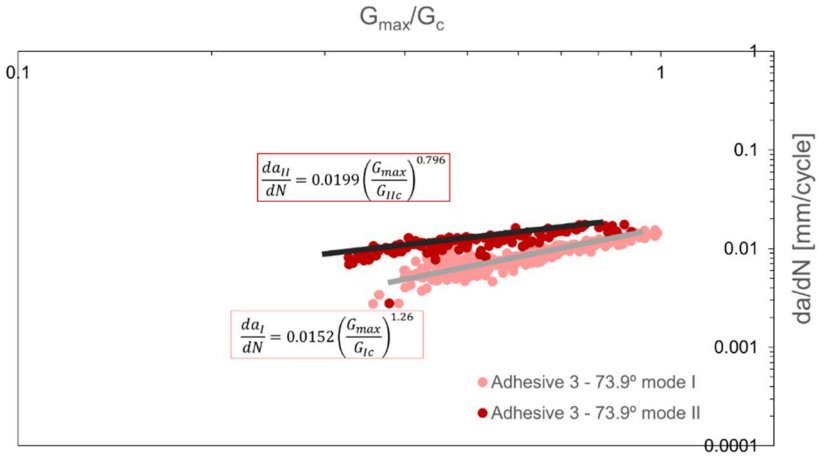

Figure 4.46 – Representative FCG curve for Adhesive 3 in mixed-mode (φ=73.9º).

Table 4.16 shows the results of the Paris law parameters obtained.

Table 4.16 – Paris law constants of the mixed-mode specimens tested (φ=73.9º).

Adhesive	Specimen	m_I	C_I	m_{II}	C_{II}
2	1	0.39	0.0718	1.20	0.0350
	2	0.30	0.0793	0.90	0.0310
	3	0.27	0.0420	0.75	0.7000
	Average	0.32 ± 0.05	0.0644 ± 0.0161	0.93 ± 0.17	0.2553 ± 0.3144
3	1	0.750	0.0459	0.765	0.0459
	2	0.75	0.133	0.829	0.133
	3	1.26	0.0199	0.796	0.0199
	Average	0.92 ± 0.240	0.056 ± 0.03	0.80 ± 0.03	0.066 ± 0.240

These results indicate the same dispersion of the intersection parameter and a good agreement of the slope values.

4.3.4 Summary of fatigue results

In order to have a better perception of the fatigue behaviour in terms of mixed-mode angle, two analysis were done: the Paris law slope envelope and the total Paris law slope evolution with φ.

Since the intersection parameter C in the FCG curves always present some scatter, it was assumed that the intersection does not have any tendency.

4.3.4.1 Paris law slope envelope

Using the Paris law slope parameters defined by the fatigue experiments, it was possible to build the envelopes of the Paris law slope for the two adhesives (Figure 4.47). Observing those two envelopes, it can be said that the crack propagation rate verified in pure mode II is lower than in pure mode I and that the mixed-mode angles studied present intermediate m values for the two components. Only Adhesive 3 in φ=56.6º showed a deviation from the global tendency, with higher values of m_{II} that it was expected. The envelopes fit well with a quadratic criterion.

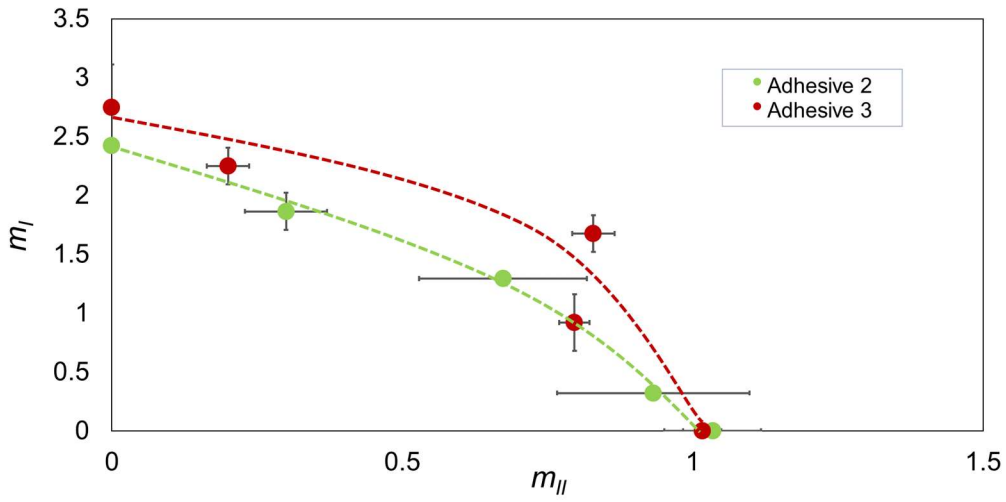

Figure 4.47 – Paris law m parameter envelope.

4.3.4.2 m_T *vs* φ

Finally, in order to compare the results obtained in other studies of the mixed-mode fatigue behaviour, a criterion was applied to define the total Paris law parameters. Interesting results for the total Paris law slope evolution with the mixed-mode angle were obtained when using the relation established by Benzeggagh & Kenane (1996) to define the total critical energy release rate in mixed-mode conditions. This relation gives the total G_{TC} considering the modal ratio G_{II}/G_T

$$G_{TC} = G_{IC} + (G_{IIC} - G_{IC}) \left(\frac{G_{II}}{G_T}\right)^n$$

Using m_T instead of G_{TC} in this relation, an expression to calculate the total Paris law slope in mixed-mode conditions was obtained.

$$m_T = m_I + (m_{II} - m_I) \left(\frac{G_{II}}{G_T}\right)^{n=1}$$

n was considered to be 1 to obtain a linear relation.

The results obtained for the total Paris law slope as a function of the mixed-mode angle are presented in Figure 4.48. It is verified that Adhesive 3 shows higher values of FCG slope, indicating that more brittle adhesives are more susceptible to fatigue loadings, leading to faster propagation. According to the criterion established for m_T, the type of loading changes the crack propagation rate. Moreover, observing the decreasing tendency of m_T with the mixed-mode angle it is concluded that mode II loads contribute to delay the propagation. The error values calculated using Benzeggagh & Kenane (1996) relation were lower than the deviations showed in the slope envelopes.

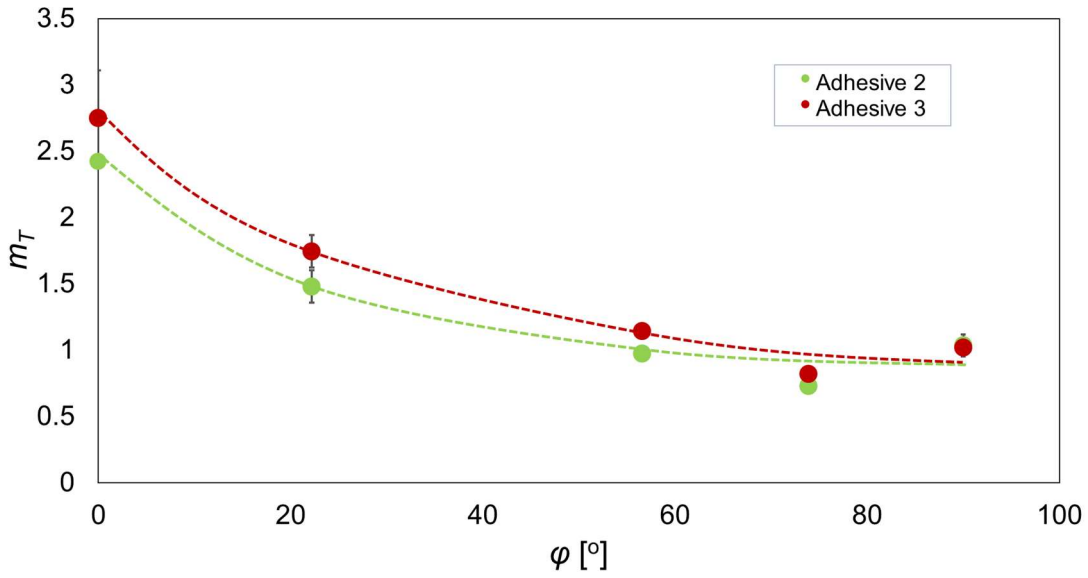

Figure 4.48 – Paris law m parameter as a function of the mixed mode-angle.

5 Numerical analysis

A numerical analysis implemented in ABAQUS® was performed to model the experimental fracture results. The adherends were modelled with 4-node bilinear plane strain quadrilateral elements (CPE4R in ABAQUS®) and the 0.2 mm thickness of adhesive layer was modelled using 4-node two-dimensional cohesive elements (COH2D4 in ABAQUS®). This numerical analysis focused on the behaviour of Adhesive 3, which was simulated using DCB and mixed-mode models to develop the model so that in the future it can applied other adhesives.

The mechanical properties used in the simulations are presented in Table 5.1.

Table 5.1 – Elastic and cohesive properties

Elastic Properties (Steel)			Elastic Properties (Adhesive 3)		Cohesive Properties (Adhesive 3)			
E [GPa]	G^* [GPa]	υ	E [GPa]	G^* [GPa]	σ_R [MPa]	$\tau_{R^{**}}$ [MPa]	G_{Ic} [N/mm]	G_{IIc} [N/mm]
210	78.9	0.3	4.04	1.51	51.64	29.81	1.51	6.39

*deducted from the Young's modulus
** deducted from σ_R applying Von Mises relation

The dimension of the cohesive elements is shown in Table 5.2.

Table 5.2 – Dimension of the cohesive elements.

Number of elements	1225
Size of the elements	0.2 mm

Damage onset and propagation within the adhesive were simulated using a triangular traction-separation law. As explained in section 2.4, this softening law is adequate for brittle adhesives.

Figure 5.1 presents a detail of the specimen's mesh. A more refined mesh was used in the damage propagation zone, near the adhesive.

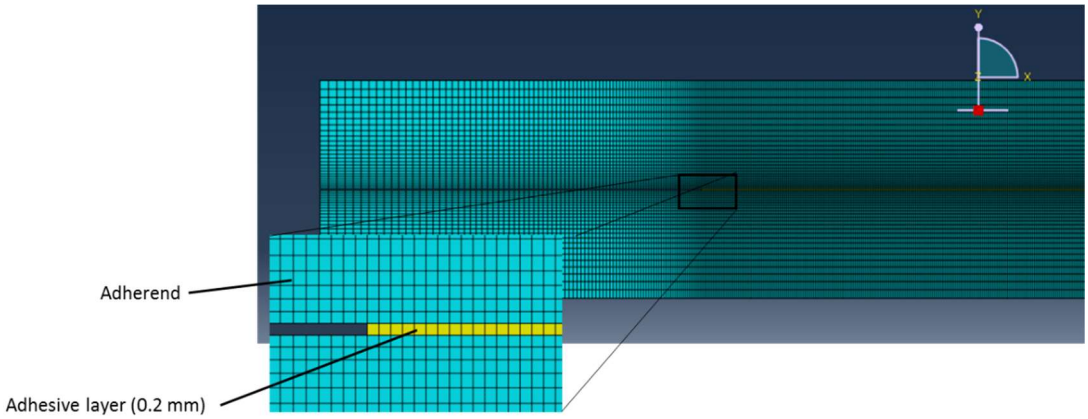

Figure 5.1 – Mesh used in the numerical analysis.

In the following sections the results of the numerical analysis obtained for mode I and mixed-mode conditions will be presented.

5.1 Mode I model

A schematic representation of the boundary conditions used for mode I is presented in Figure 5.2.

Figure 5.2 – Boundary conditions of the DCB test.

The deformed shape resulting from applying mode I loading shows the damage in the adhesive layer (Figure 5.3).

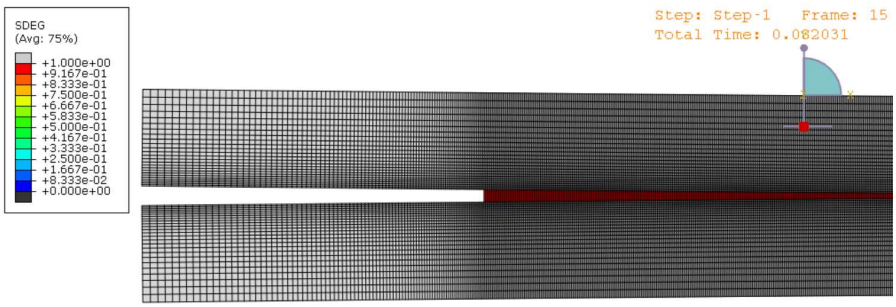

Figure 5.3 – Deformed shape for mode I loading (SDEG).

P-δ and R-curves obtained by numerical and experimental analysis are presented in Figure 5.4 and Figure 5.5. Regarding the P-δ curves, the numerical analysis showed higher stiffness as expected, and higher failure load probably due to experimental imperfections in the adhesive layer. However, the R-curves are in good agreement. The numerical model provides a value of G_I close to the experimental results ($G_{I_{model}} = 1.45$ N/mm and $G_{I_{exp}} = 1.51 \pm 0.26$ N/mm)

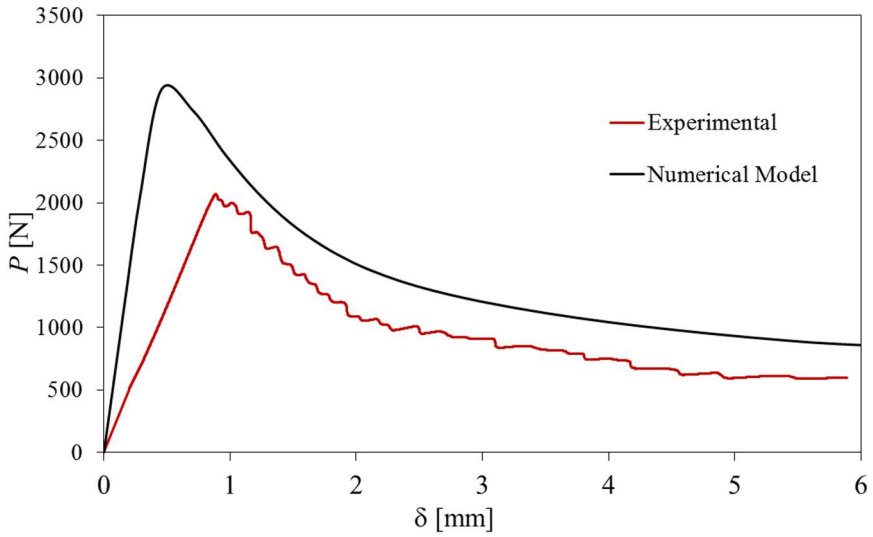

Figure 5.4 – Experimental and numerical P-δ curves for DCB test.

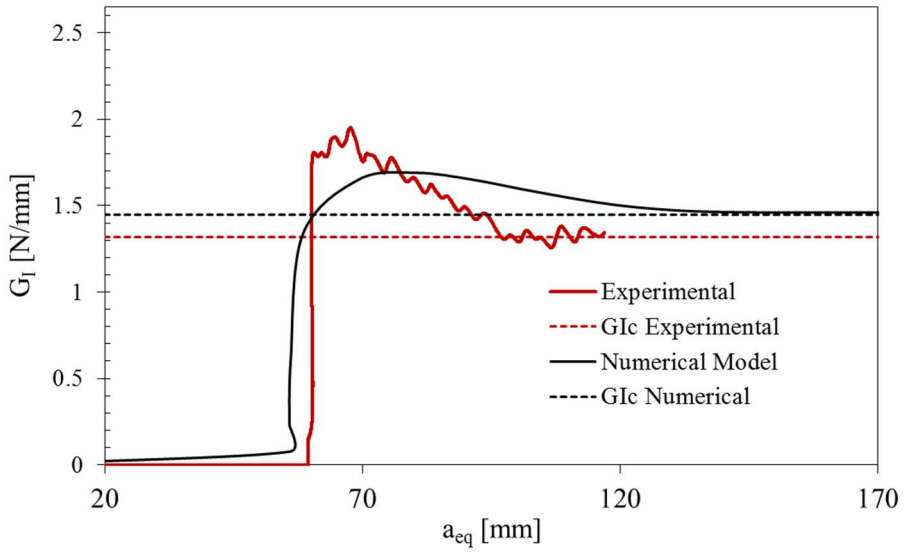

Figure 5.5 – Experimental and numerical R-curves for a DCB test.

5.2 Mixed-mode model

Mixed-mode models were used to validate some of the results obtained using the mixed-mode apparatus ($\varphi = 22.2^o$ and $\varphi = 61.7^o$). The loading device was reproduced using rigid beams and links, as represented in Figure 5.6 and Figure 5.7.

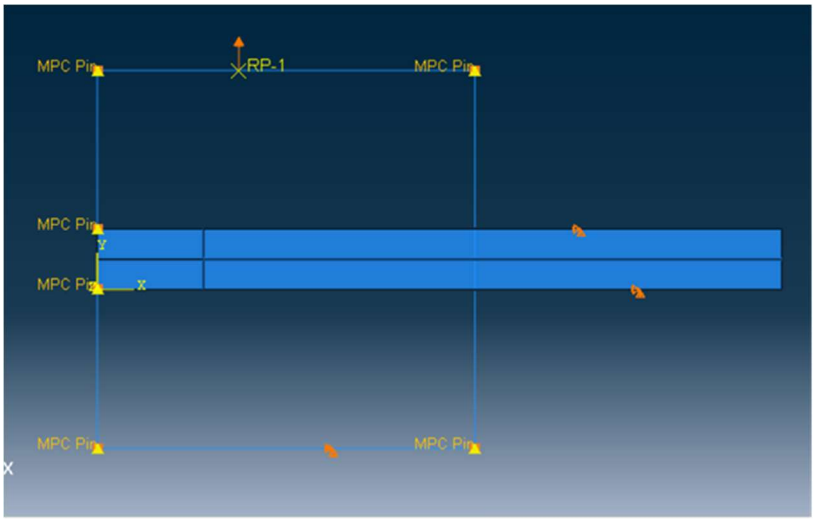

Figure 5.6 – Boundary conditions of the mixed-mode test: φ =22.2º.

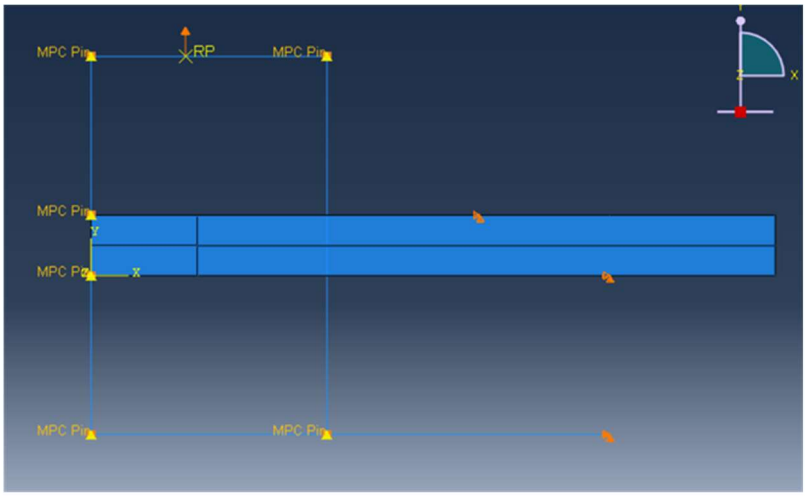

Figure 5.7 – Boundary conditions of the mixed-mode test: φ =61.7º.

P-δ curves obtained by numerical and experimental analysis are presented in Figure 5.8 and Figure 5.9. Again, the P-δ curves of the numerical analysis showed higher stiffness and higher failure load.

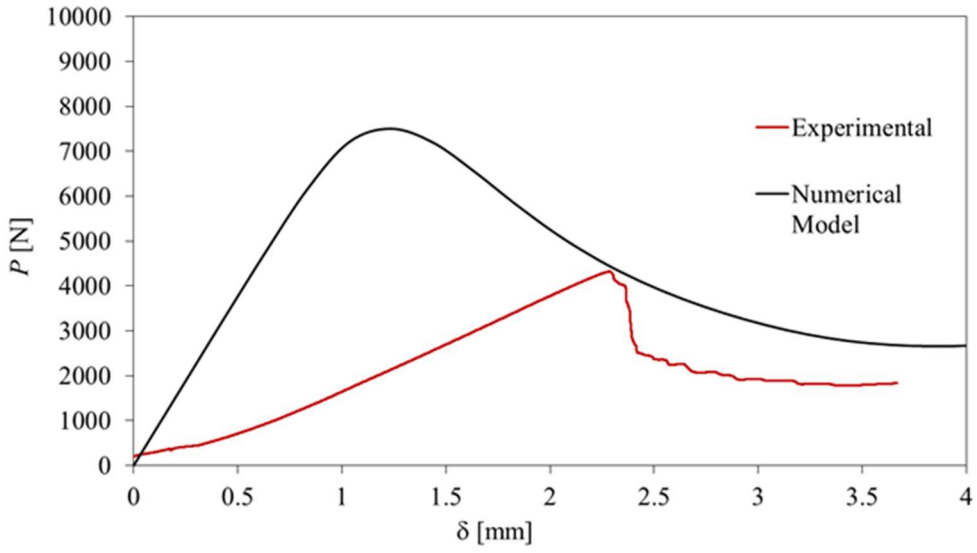

Figure 5.8 – Numerical and experimental P-δ curves of the mixed-mode test: φ=22.2º.

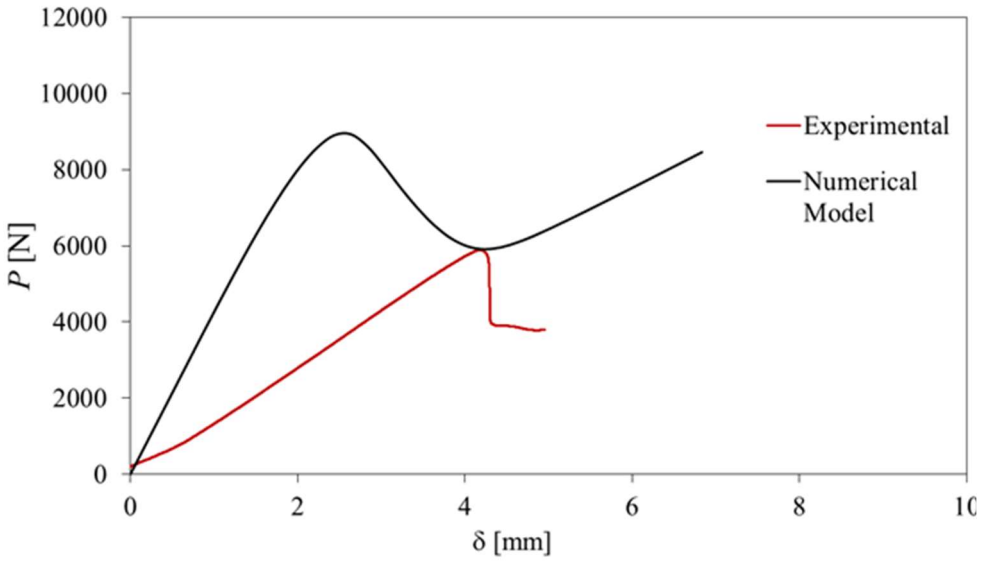

Figure 5.9 – Numerical and experimental P-δ curves of the mixed-mode test: φ=61.7º.

The LVDT displacements were also compared between numerical and experimental studies as seen in Figure 5.10 and Figure 5.11. Although the curves are significantly different, the similar tendencies of the displacements recorded during the experiments and the models output displacements show that the models are applying loads close to the required.

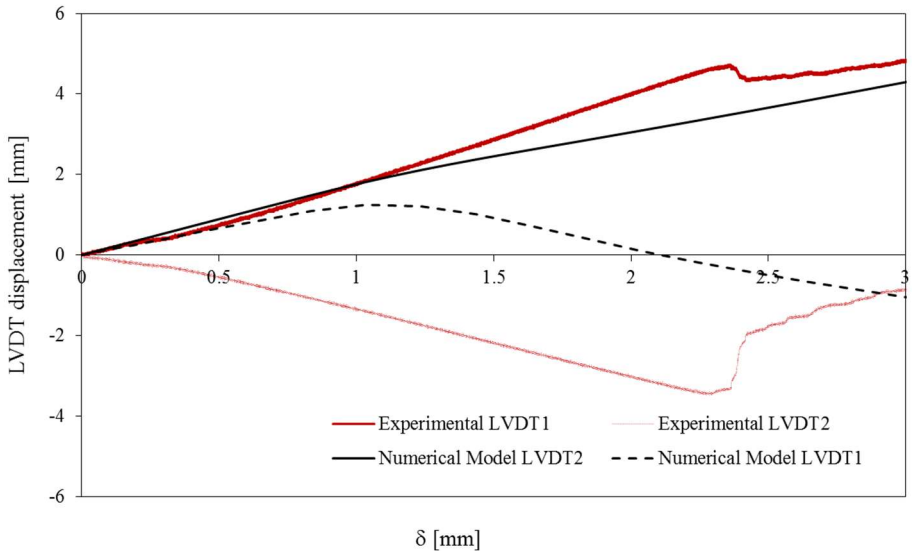

Figure 5.10 – LVDT displacements obtained by numerical and experimental analysis: φ=22.2º.

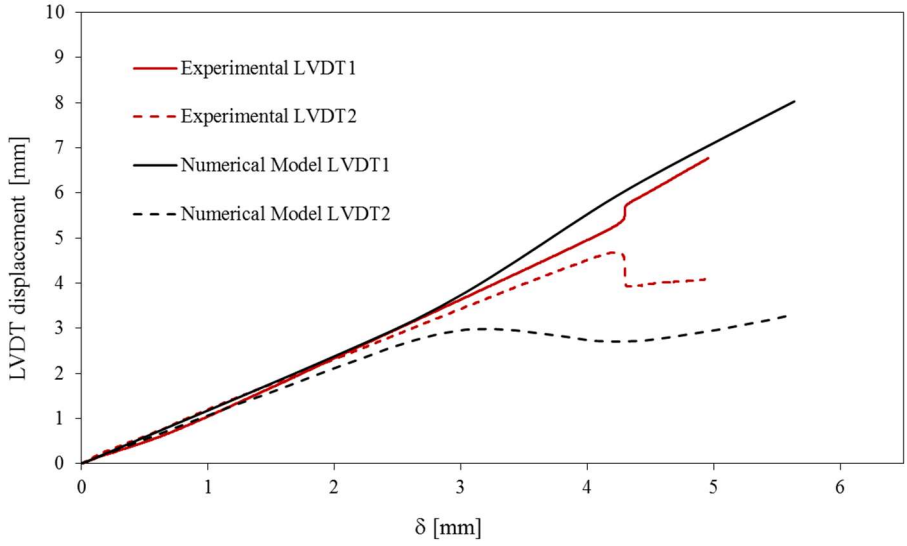

Figure 5.11 – LVDT displacements obtained by numerical and experimental analysis: φ=61.7º.

The numerical R-curves were determined applying the crack equivalent concept of CBBM. Comparing those numerical R-curves with the experimental ones (Figure 5.12 and Figure 5.13) we can see that the models always overestimate the fracture energies. For the mode I component of $\varphi = 22.2^o$ the model predicted $G_{Ic} = 3.5$ N/mm while the experiments pointed to $G_{Ic} = 1.42 \pm 0.43$ N/mm. Mode II components had a good agreement in this case ($G_{II\ model} = 0.50$ N/mm and $G_{IIc_{exp}} = 0.51 \pm 0.10$ N/mm).

The opposite situation occurred for $\varphi = 61.7^o$. Fracture energies in mode I were in good agreement ($G_{Ic_{model}} = 1.3$ N/mm and $G_{Ic_{exp}} = 1.25 \pm 0.17$ N/mm) while fracture energies in mode II were significantly different ($G_{IIc_{model}} = 5.0$ N/mm and $G_{IIc_{exp}} = 3.32 \pm 0.22$ N/mm).

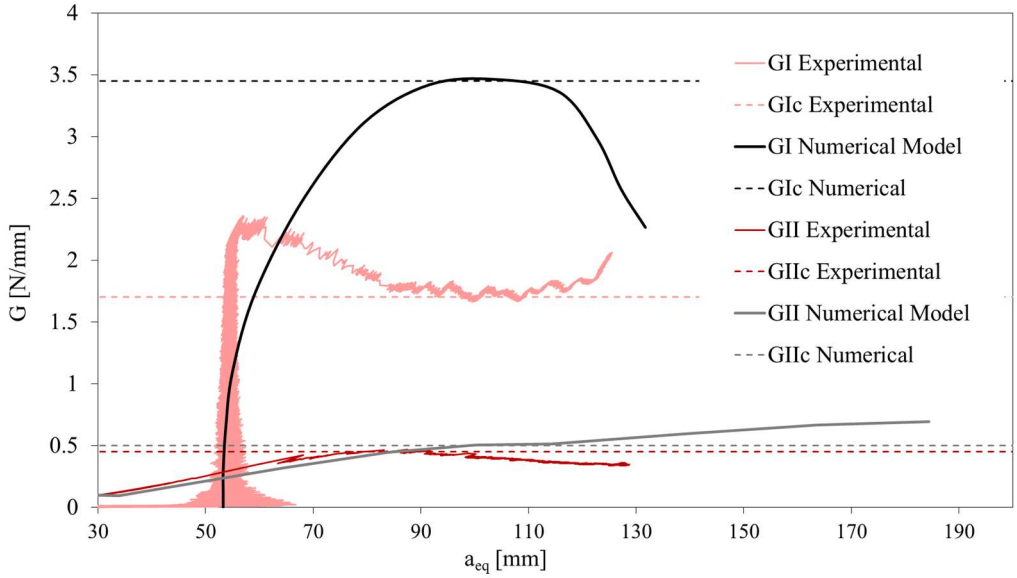

Figure 5.12 – R-curves obtained by numerical and experimental analysis for a mixed-mode test: φ=22.2º.

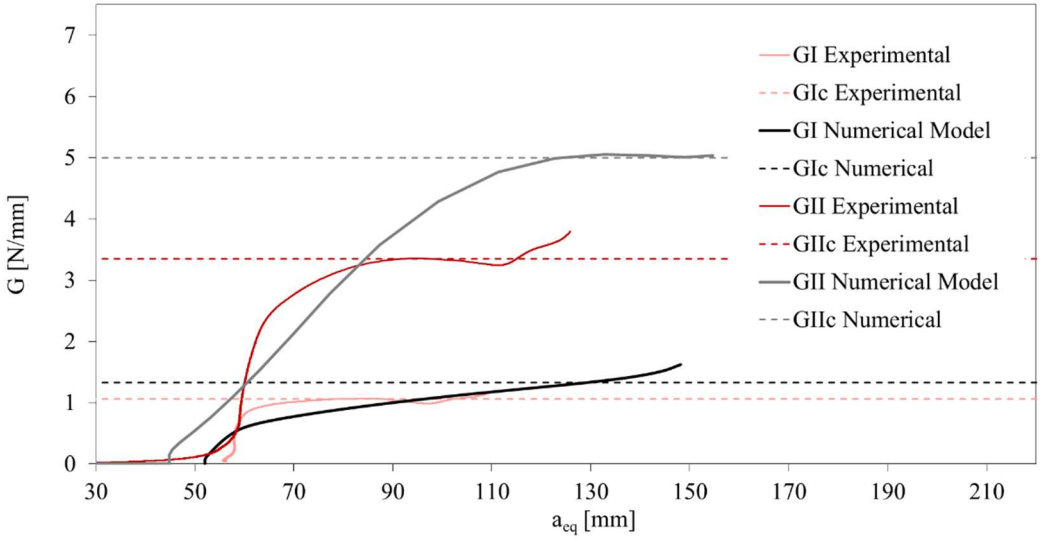

Figure 5.13 – R-curves obtained by numerical and experimental analysis for a mixed-mode test: φ=61.7º.

5.3 Summary of numerical results

Figure 5.14 shows the numerical results obtained inserted in the experimental fracture envelope of Adhesive 3.

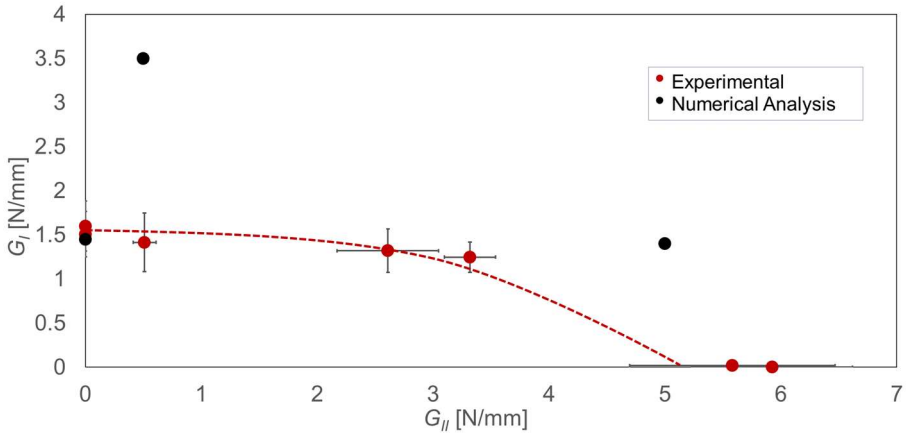

Figure 5.14 – Experimental fracture envelope of Adhesive 3 and numerical results.

The results show that the models need to be improved. Although there are some evidences of good predictions, the mixed-mode models are not able yet to evaluate the fracture behaviour of this adhesive. The difference between numerical and experimental results can be explained by the stiffness of the model components. The apparatus setup modelled may be absorbing some of the energy applied, instead of transmitting the load to the specimen. Though the stiffness of the model must be corrected. The type of adhesive also certainly influences the results, and the fact that the triangular law is the only traction-separation curve implemented for the cohesive zone model in ABAQUS® also adds to the number of factors that must be closely studied before modelling the remaining adhesives.

6 Conclusions and future works

6.1 Conclusions

The main objectives of this thesis were to assess the mixed-mode fatigue and the fracture behaviour of adhesively bonded joints.

Performing DCB, ENF and mixed-mode tests in a wide range of load conditions, from pure mode I to pure mode II allowed to obtain a fracture envelope for the three adhesives studied.

Fracture envelopes of adhesives 2 and 3 showed a moderately good agreement with the quadratic criterion while the fracture envelope of Adhesive 3 fitted better with the linear criterion. It was also found that Adhesive 1 showed the more ductile behaviour with higher fracture energies in all the static tests performed while Adhesive 3 was found to be the most brittle of the three. A good approximation of the fracture energy in mode I was obtained using the numerical analysis. The mixed-mode models still need an improvement to provide good predictions of the fracture behaviour of the Adhesive 3.

The fatigue study presented in this work was a first approach to the mixed-mode crack propagation behaviour using a mixed-mode apparatus that analyses the mode I and mode II components separately.

FCG curves of mode I and mode II components were determined for two adhesives in three different phase angles. This curves led to the Paris law slope envelope.

The comparison of these results with other studies done before required the establishment of a criterion to obtain the total Paris law slope parameter, m_T.The evolution of m_T as a function of the mixed mode angle showed that the presence of mode II loads delay the crack propagation rate. This behaviour was consistent with other works found in the literature, therefore validating our methodology and novel approach at studying the mixed-mode crack propagation behaviour.

6.2 Future works

The work presented suggests a relationship between the Paris law slope of mode I and mode II components in mixed-mode conditions. In order to validate this assumption it would be interesting to perform a mixed-mode test in the same fatigue conditions and with the same adhesive using another mixed-mode specimen such as ATCB or SLB. After determining the FCG curves, the Paris law slope could be compared to the results obtained here.

Another suggestion is the improvement of the fracture analysis of the mixed-mode apparatus by measuring the stiffness of its components thus giving a better estimative of the fracture energy. That could be achieved by performing the same tests in the apparatus using a steel-only specimen.

It would also be interesting to improve the numerical models to obtain better agreement between numerical and experimental results and to include numerical analysis for the other adhesives that were not considered in this satudy.

References

Adams, R.D., Comyn, J. & Wake, W.C., 1997. *Structural adhesive joints in engineering*, Springer Science & Business Media.

ASTM D-3433-99, 2004. Standard Test Method for Fracture Strength in Cleavage of Adhesives in Bonded Joints. *Current*, 98(Reapproved), pp.1–5.

ASTM D-638, 2003. Standard Test Method for Tensile Properties of Plastics. *ASTM, West Conshohocken, PA*.

ASTM D6671, 2001. Standard Test Method for mixed modeI-Mode II Interlaminar Fracture Toughness of Unidirectional Fiber-Reinforced Composites. *Annual book of ASTM standards*, 15, p.3.

ASTM E-647, 2002. Standard test method for measurement of fatigue crack growth rates. *Annual Book of ASTM Standards, Section Three: Metals Test Methods and Analytical Procedures*, 3, pp.628–670.

Benzeggagh, M.L. & Kenane, M., 1996. Measurement of mixed-mode delamination fracture toughness of unidirectional glass/epoxy composites with mixed-mode bending apparatus. *Composites science and technology*, 56(4), pp.439–449.

Campilho, R.D.S.G. & da Silva, L.F.M., 2014. Mode I fatigue and fracture behaviour of adhesively-bonded carbon fibre-reinforced polymer (CFRP) composite joints. *Fatigue and Fracture of Adhesively-Bonded Composite Joints*, p.93.

Carraro, P.A. et al., 2013. Crack propagation analysis in composite bonded joints under mixed-mode (I+ II) static and fatigue loading: experimental investigation and phenomenological modelling. *Journal of Adhesion Science and Technology*, 27(11), pp.1179–1196.

Chaves, F.J.P., da Silva, L.F.M., et al., 2013. Apparatus and Method for Characterization of Bonded Joints Mixed Mode I + II Fracture DEMec Engineering Science and Mechanics Department , Virginia Tech , Blacksburg , VA 24061. , pp.3–6.

Chaves, F.J.P., de Moura, M.F.S.F., et al., 2014. Fracture characterization of bonded joints using the dual actuator load apparatus. *Journal of Adhesion Science and Technology*, 28(5), pp.512–524.

Chaves, F.J.P., Da Silva, L.F.M., et al., 2014. Fracture mechanics tests in adhesively bonded joints: a literature review. *The Journal of Adhesion*, 90(12), pp.955–992.

Chaves, F.J.P. et al., 2011. Numerical analysis of the dual actuator load test applied to fracture characterization of bonded joints. *International Journal of Solids and Structures*, 48(10),

pp.1572–1578.

Chaves, F.J.P., de Moura, M., et al., 2013. Numerical validation of a crack equivalent method for mixed-mode I+ II fracture characterization of bonded joints. *Engineering Fracture Mechanics*, 107, pp.38–47.

Fernández, M. V et al., 2011. Composite bonded joints under mode I fatigue loading. *International Journal of Adhesion and Adhesives*, 31(5), pp.280–285.

Fernández, M. V et al., 2013. Mixed-mode I+ II fatigue/fracture characterization of composite bonded joints using the Single-Leg Bending test. *Composites Part A: Applied Science and Manufacturing*, 44, pp.63–69.

Fernández, M.V., 2008. Fracture Characterization of Composite Bonded Joints Under Fatigue Loading.

Fernlund, G. & Spelt, J.K., 1994. Mixed-mode fracture characterization of adhesive joints. *Composites Science and Technology*, 50(4), pp.441–449.

de Goeij, W.C., Van Tooren, M.J.L. & Beukers, A., 1999. Composite adhesive joints under cyclic loading. *Materials & design*, 20(5), pp.213–221.

Griffith, A.A., 1921. The phenomena of rupture and flow in solids. *Philosophical transactions of the royal society of london. Series A, containing papers of a mathematical or physical character*, 221, pp.163–198.

Hafiz, T.A. et al., 2013. Mixed-mode fatigue crack growth in FM73 bonded joints. *International Journal of Adhesion and Adhesives*, 40, pp.188–196.

Irwin, G.R., Kies, J.A. & Smith, H.L., 1958. Fracture strengths relative to onset and arrest of crack propagation. In *Proc. ASTM*. pp. 640–657.

Katsiropoulos, C. V et al., 2012. Fracture toughness and shear behavior of composite bonded joints based on a novel aerospace adhesive. *Composites Part B: Engineering*, 43(2), pp.240–248.

de Moura, M.F.S.F., Gonçalves, J.P.M., et al., 2008. Cohesive and continuum mixed-mode damage models applied to the simulation of the mechanical behaviour of bonded joints. *International Journal of Adhesion and Adhesives*, 28(8), pp.419–426.

de Moura, M.F.S.F., Campilho, R.D.S.G. & Gonçalves, J.P.M., 2008. Crack equivalent concept applied to the fracture characterization of bonded joints under pure mode I loading. *Composites Science and Technology*, 68(10), pp.2224–2230.

de Moura, M.F.S.F., Campilho, R.D.S.G. & Gonçalves, J.P.M., 2009. Pure mode II fracture characterization of composite bonded joints. *International Journal of Solids and Structures*, 46(6), pp.1589–1595.

Pirondi, A. & Nicoletto, G., 2006. Mixed mode I/II fatigue crack growth in adhesive joints. *Engineering fracture mechanics*, 73(16), pp.2557–2568.

Renart, J. et al., 2014. Mode I fatigue behaviour and fracture of adhesively-bonded fibre-reinforced polymer (FRP) composite joints for structural repairs. *Fatigue and Fracture of Adhesively-Bonded Composite Joints*, p.121.

Rodrigues, T.A.F., 2015. Determination of the fracture envelope of an adhesive joint as a function moisture.

Shahverdi, M. & Vassilopoulos, A.P., 2014. Mixed-mode fatigue and fracture behavior of adhesively-bonded composite joints. *Fatigue and Fracture of Adhesively-Bonded Composite Joints*, p.187.

da Silva, L.F.M., Dillard, D.A. & Blackman, B., 2012. *Testing adhesive joints: best practices*, John Wiley & Sons.

da Silva, L.F.M., Esteves, V.H.C. & Chaves, F.J.P., 2011. Fracture toughness of a structural adhesive under mixed mode loadings. *Materialwissenschaft und Werkstofftechnik*, 42(5), pp.460–470.

da Silva, L.F.M., de Magalhaes, A.G. & de Moura, M.F.S.F., 2007. *Juntas adesivas estruturais*, Publindustria.

da Silva, L.F.M., Öchsner, A. & Adams, R.D., 2011. *Handbook of adhesion technology*, Springer Science & Business Media.

Stamoulis, G. et al., 2014. On the experimental mixed-mode failure of adhesively bonded metallic joints. *International Journal of Adhesion and Adhesives*, 51, pp.148–158.

Vassilopoulos, A.P., Shahverdi, M. & Keller, T., 2014. Mode I fatigue and fracture behavior of adhesively-bonded pultruded glass fiber-reinforced polymer (GFRP) composite joints. *Fatigue and Fracture of Adhesively-Bonded Composite Joints*, p.149.

APPENDIX A: Fracture results

Mode I

Adhesive	Specimen	G_{Ic} [N/mm]
1	1	2.33
	2	1.9
	3	1.95
	Average	2.06 ± 0.23
2	1	1.37
	2	1.56
	3	1.78
	Average	1.57 ± 0.21
3	1	1.32
	2	1.8
	3	1.4
	Average	1.51 ± 0.26

Mode II

Adhesive	Specimen	G_{IIc} [N/mm]
1	1	6.10
	2	6.00
	3	6.50
	Average	6.20 ± 0.26
2	1	7.80
	2	7.70
	3	7.05
	Average	7.52 ± 0.41
3	1	6.84
	2	6.11
	3	6.21
	Average	6.39 ± 0.40

Mixed-mode I+II

$\varphi = 0.0°$

Adhesive	Specimen	G_I [N/mm]	G_{II} [N/mm]	φ_{eff} [º]
2	1	1.7	–	0.0
	2	2.05	–	0.0
	3	2.1	–	0.0
	Average	1.95 ± 0.22	–	0.0 ± 0.0
3	1	1.40	–	0.0
	2	1.80	–	0.0
	Average	1.60 ± 0.28	–	0.0 ± 0.0

$\varphi = 22.2°$

Adhesive	Specimen	G_I [N/mm]	G_{II} [N/mm]	φ_{eff} [º]
1	1	3.05	1.35	33.6
	2	2.90	1.15	32.2
	3	2.90	0.93	29.5
	Average	2.95 ± 0.09	1.14 ± 0.21	31.8 ± 2.1
2	1	2.45	0.68	27.8
	2	2.50	0.90	31.0
	3	1.90	0.73	31.8
	4	2.00	0.65	29.7
	Average	2.21 ± 0.31	0.74 ± 0.11	30.1 ± 1.8
3	1	1.65	0.58	30.7
	2	1.18	0.44	31.4
	Average	1.42 ± 0.33	0.51 ± 0.10	31.0 ± 0.5

$\varphi = 56.6°$

Adhesive	Specimen	G_I [N/mm]	G_{II} [N/mm]	φ_{eff} [º]
2	1	1.40	3.35	57.1
	2	1.50	3.5	56.8
	Average	1.35 ± 0.07	3.43 ± 0.40	56.9 ± 0.23
3	1	1.70	3.25	54.1
	2	1.20	2.15	53.2
	3	1.25	2.25	53.3
	4	1.40	2.70	54.2
	5	1.05	2.70	58.1
	Average	1.32 ± 0.25	2.61 ± 0.44	54.6 ± 2.0

$\varphi = 61.7°$

Adhesive	Specimen	G_I [N/mm]	G_{II} [N/mm]	φ_{eff} [º]
1	1	1.31	4.95	62.8
	2	1.00	4.03	63.5
	3	1.55	4.78	60.3
	Average	1.29 ± 0.28	4.59 ± 0.49	62.2 ± 1.7
2	1	1.15	3.92	61.6
	2	1.30	4.80	62.5
	3	1.20	3.58	59.9
	Average	1.22 ± 0.08	4.10 ± 0.63	61.3 ± 1.3
3	1	1.50	3.65	57.3
	2	1.20	3.20	58.5
	3	1.12	3.20	59.4
	4	1.17	3.22	58.9
	Average	1.25 ± 0.17	3.32 ± 0.22	58.5 ± 0.9

$\varphi = 86.9°$

Adhesive	Specimen	G_I [N/mm]	G_{II} [N/mm]	φ_{eff} [º]
1	1	0.02	7.60	87.1
	2	0.03	8.35	86.6
	3	0.02	6.50	86.8
	4	0.03	7.75	86.4
	Average	0.03 ± 0.01	7.55 ± 0.77	86.7 ± 0.3
2	1	0.02	6.45	86.8
	2	0.02	6.28	86.8
	3	0.03	7.80	86.5
	4	0.03	7.70	86.4
	Average	0.03 ± 0.01	7.06 ± 0.80	86.6 ± 0.2
3	1	0.01	6.40	87.7
	2	0.02	5.40	86.5
	3	0.01	4.65	86.2
	4	0.02	6.60	86.8
	5	0.02	4.85	86.3
	6	0.02	5.25	86.5
	Average	0.02 ± 0.01	5.53 ± 0.80	86.9 ± 0.6